Measuring surface water flow velocities by a drone and large-scale particle image velocimetry (LSPIV)

Master Thesis
August 2022

Omar Sharif

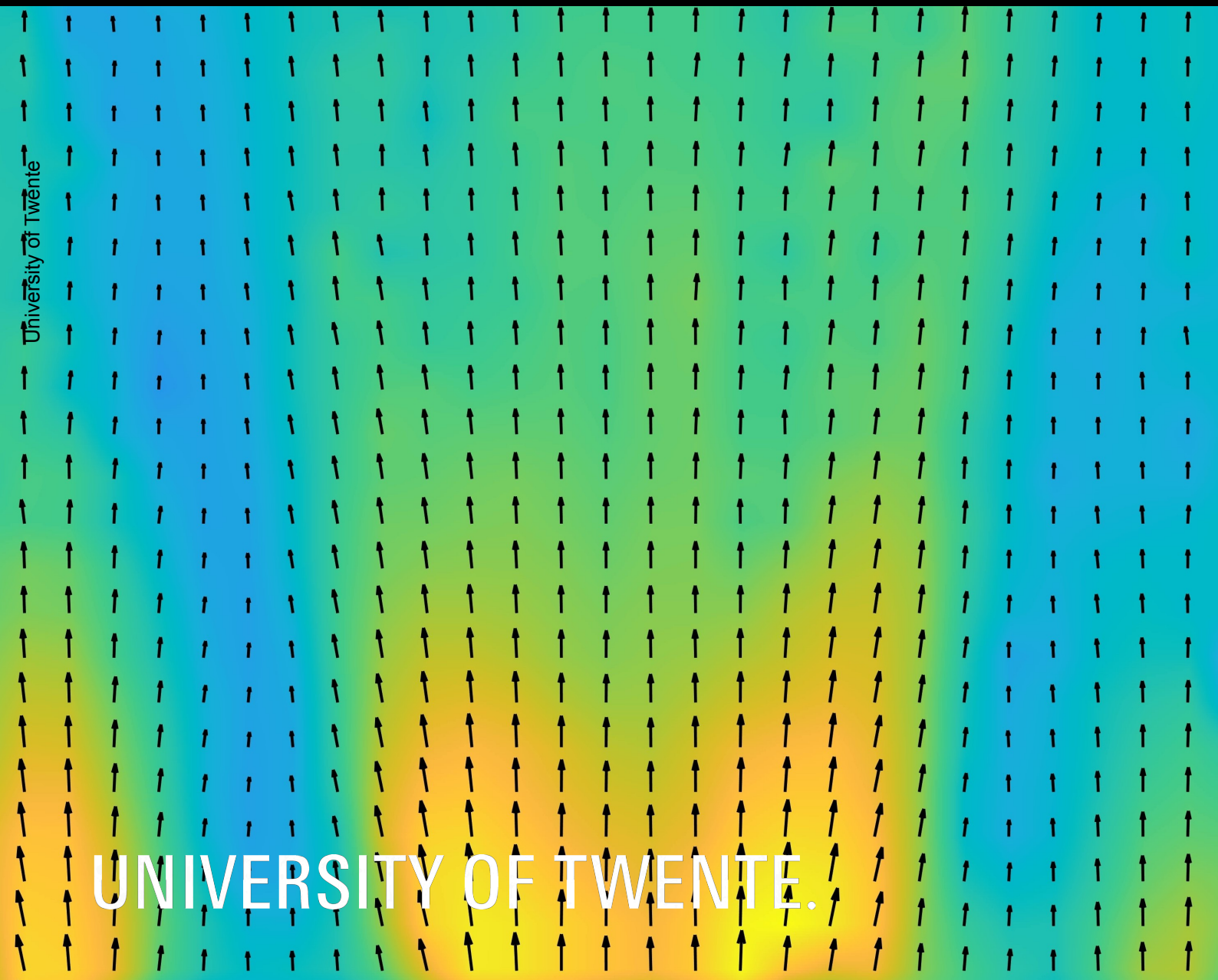

UNIVERSITY OF TWENTE.

Measuring surface water flow velocities by a drone and large-scale particle image velocimetry (LSPIV)

by

Omar Sharif

Student Number
S1929232

to obtain the degree of Master of Science
at the University of Twente,
to be defended publicly on August 24, 2022

Daily supervisor:	Dr. V. Kitsikoudis (Vasileios)
Head graduation committee:	Dr.ir. D.C.M. Augustijn (Denie)
Institution:	University of Twente
Place:	Faculty of Engineering Technology, Enschede
Programme:	Water Engineering & Management (WEM)
Document version:	Final version (15-08-2022)
Project duration:	April, 2022 - August, 2022

Cover Image: Vector field representing surface water flow velocities downstream of a weir in the Dinkel River.

UNIVERSITY
OF TWENTE.

Preface

Before you lies the Master Thesis *"Measuring surface water flow velocities by a drone and large-scale particle image velocimetry (LSPIV)"*. This thesis project was carried out to fulfil the graduation requirements for the degree of Master of Science in Civil Engineering & Management. The research work that it presents was conducted from April to August 2022 at the Water Engineering & Management department at the University of Twente in Enschede.

First and foremost, I would like to take this opportunity to express my full appreciation and gratitude to my supervisors, Vasileios Kitsikoudis and Denie Augustijn. Completing this thesis would not have been possible without their excellent guidance, involvement and expertise. My sincere gratitude goes to Vasileios Kitsikoudis, whose enthusiasm and encouragement kept me motivated throughout my thesis project. I really enjoyed the fun conversations during our weekly meetings. I would also like to thank Denie Augustijn for his willingness to help and insightful suggestions. Additionally, I want to acknowledge the excellent work of Emre Ozturk during the field campaigns; without his efforts, expert advice and drone flying skills, I would not have been able to carry out the research work. Finally, I thank Rijkswaterstaat for allowing us to collect field data at the Sambeek lock-weir complex.

Last but not least, I am extending my heartfelt thanks to my family and friends for always supporting me.

I hope you enjoy reading my work!

Omar Sharif
Enschede, August 2022

Summary

Purpose – The infeasibility and impracticality of using intrusive measurement equipment to collect information on flow velocities in complex environments created a compelling need for alternative, non-intrusive velocimetry approaches. Several studies have already demonstrated that drone-borne imaging techniques allow for quick, safe and comprehensive quantification of surface flow velocities. Despite the efforts of the existing studies, there is still limited experience in using such techniques. Within this context, this research aimed to assess the feasibility of using drone-borne imaging techniques and large-scale particle image velocimetry (LSPIV) to infer surface flow velocities within large-scale fluvial applications. This research also aimed to provide a process-based explanation as to why or how certain methods are effective or ineffective when applying LSPIV. A fundamental requirement in LSPIV is that the surface of the flow must be seeded with tracers. This research investigated whether it is feasible to apply LSPIV in flows seeded by naturally occurring features, such as foam and air bubbles generated by turbulent activities in the flow.

Methods and materials – A detailed workflow was developed to guide the LSPIV analyses performed in this study. The LSPIV workflow can be characterised by four main stages, including (1) data acquisition and preparatory work; (2) image pre-processing; (3) image evaluation; and (4) post-processing. The first stage involved the collection of video recordings of the flowing water near hydraulic structures at two study areas in the Netherlands, namely the Dinkel River at Lattrop-Breklenkamp and Meuse River at Sambeek. These recordings were collected by both a drone and terrestrial camera system. In the second stage, images obtained from the field campaign were processed through the application of image stabilisation and orthorectification to reduce the effects of image distortions, deformations and instabilities; the imagery was also enhanced with various filters to improve the detectability and traceability of features on the water surface. Subsequently, the LSPIV algorithm was applied to the pre-processed imagery to obtain a vector field representing the surface water flow velocities at both study areas. The LSPIV algorithm essentially attempts to estimate the displacement of distinct features on the water surface through the application of a statistical pattern matching technique; more specifically, the cross-correlation function is computed to achieve this. The algorithm then relates the recorded displacements to the velocity field of the observed flow. In the final stage, spurious vectors in the vector field were corrected, and an accuracy assessment was performed using reference velocity measurements obtained from the so-called float method. This research further explored the influence of various experimental configurations and image processing parameters on the LSPIV outputs through an extensive sensitivity analysis. Finally, this study performed a comparative analysis of drone-based LSPIV with conventional, fixed camera LSPIV implementations.

Results and discussion – Naturally occurring features on the water surface were found to be omnipresent in the Dinkel River study area at the time of the field campaign; the seeding density was estimated to be around 10%, and overall adequate seeding homogeneity was observed. The LSPIV-derived surface water flow velocities for the Dinkel River case were in relatively good agreement with the reference velocity measurements, with mean absolute velocity deviations in the order of 10^{-2} m/s and normalised root mean squared values ranging between 5% and 9%. The velocity fields could accurately describe the bulk flow behaviour and capture horizontal flow structures at different spatial scales. The LSPIV analysis in the case of the Meuse River study area yielded comparatively worse agreement with the reference measurements; the accuracy assessment revealed mean absolute deviations from the reference values in the order of 10^{-1} m/s and a normalised root mean squared error value around 35%; the poor performance was attributed to the low seeding densities (±5%) and strong seeding inhomogeneity. The sensitivity analysis highlighted the importance of specifying the appropriate sampling frequency at which the images are collected. In low flow conditions, it was required to resample the data to lower sampling frequencies (2-5 Hz) to achieve adequate LSPIV performance. Other key parameters in LSPIV implementations are the image sequence duration, interrogation area size and image resolution. The appropriate image sequence duration is highly case-specific and should be

selected with extreme care prior to the LSPIV analysis; durations of only several seconds may not be sufficient to obtain satisfactory results. The interrogation area size and image resolution are particularly important for flows that contain relatively large surface features. Based on experimental observations, the inclination of the camera axis with respect to the water surface must be kept as small as possible to minimise error associated with perspective distortions. Furthermore, the comparative analysis of drone-based LSPIV with fixed camera LSPIV implementations strongly favoured the use of drones in large-scale fluvial applications; the significant inclination of the camera axis and improper positioning of the stationary camera setup resulted in significant measurement error. Above all, low seeding densities (<10%) and seeding inhomogeneity were found to be detrimental for the measurement accuracy. In the case of tracer scarcity and seeding inhomogeneity, it is recommended that the LSPIV analysis is performed on the video portions that exhibit the best seeding conditions instead of the full video.

Conclusion – Based on the findings of this research, it can be argued that drone-based LSPIV offers a promising method for capturing the spatial and temporal structure of fluid motions without the need for artificial flow seeding. However, one must realise that the successful application of LSPIV requires a thorough understanding of its underlying principles and the parameters associated with data collection and image processing. Under the right conditions and by carefully selecting the appropriate experimental configurations and input parameters, accurate surface water flow velocity estimations may be obtained. Future research should focus attention on further establishing the validity of drone-based LSPIV; this can done by rigorously testing drone-based LSPIV implementations in different environments at different spatial scales under varying seeding and flow conditions.

Keywords: surface flow velocity; large-scale particle image velocimetry; sensitivity analysis; drone; river; hydraulic structure; Dinkel River; Meuse River

Contents

Nomenclature

Abbreviations

Abbreviation	Definition
CLAHE	Contrast Limited Adaptive Histogram Equalisation
FoV	Field of View
GCP	Ground Control Point
GNSS	Global Navigation Satellite System
GPS	Global Positioning System
GSD	Ground Sampling Distance
GUI	Graphical User Interface
LSPIV	Large-Scale Particle Image Velocimetry
MBE	Mean Bias Error
NMBE	Normalised Mean Bias Error
NRMSE	Normalised Root-Mean-Square Error
PDE	Partial Differential Equation
PIV	Particle Image Velocimetry
RMSE	Root-Mean-Square Error
ROI	Region Of Interest
SA	Sensitivity Analysis
SDI	Seeding Distribution Index
UAV	Unmanned Aerial Vehicle

List of Figures

List of Tables

1
Introduction

1.1. Background

Traditionally, flow velocities in water systems are measured by employing advanced and expensive velocity measuring equipment. Examples of such equipment are Acoustic Doppler Velocimeters (ADVs) and Acoustic Doppler Current Profilers (ADCPs). They can be characterised as intrusive instruments and are ill-suited for measurements in shallow water channels, large-scale flow phenomena (e.g., flood flows), or inaccessible locations (e.g., densely vegetated systems) (Perks et al., 2019). As a result of these challenges, it is often unfeasible to collect information on flow velocities in complex environments. However, to get a good understanding of the behaviour of these water systems, knowledge of the flow velocities is crucial. Non-intrusive velocity measuring approaches have been recently explored and may offer a solution to these challenges.

In recent years, non-intrusive measuring techniques to study flows in large-scale fluvial environments have gained much popularity (Aberle et al., 2017; Jolley et al., 2021). Several studies have already demonstrated that remote sensing techniques allow for quick, safe and comprehensive quantification of surface flow velocities. More specifically, both the scientific community and the commercial sector have paid increasing attention to the application of the so-called 'image velocimetry' approach combined with optical remote sensing technologies. Such imaging technologies are, for example, optical cameras mounted on ground-based or airborne platforms. The use of unmanned aerial vehicles (UAVs) (e.g., recreational drones) is of particular interest in this case, as it allows for relatively cheap image acquisition in inaccessible environments. The acquired imagery is subsequently processed through image velocimetry techniques. Based on the recorded motion of visible particles, a two-dimensional velocity field is created using image velocimetry (Koutalakis et al., 2019). Particle Image Velocimetry (PIV), for example, is a commonly used image velocimetry algorithm. Conventionally, PIV is applied in laboratory settings in the context of experimental fluid mechanics (Aberle et al., 2017). However, developments in the past three decades have facilitated the use of conventional PIV in large-scale fluvial environments. This particular application of PIV is often referred to as large-scale PIV (LSPIV).

LSPIV-derived surface flow velocity measurements can be used to understand the flow characteristics in water systems better. Existing literature and case studies (e.g., Bandini et al., 2021; Muste et al., 2008; Strelnikova et al., 2020) demonstrate that LSPIV could provide insight into crucial hydrodynamic, morphological and ecological processes in Hydraulic Engineering applications. While the recent advancements show that LSPIV holds much potential, it is important to realise that LSPIV technology and the results that it produces are still far from perfect. Furthermore, several technical and practical challenges in LSPIV remain unresolved. At the moment, there is still limited experience in using UAV-based LSPIV. For this reason, LSPIV is still regarded as a novel approach for non-intrusive remote sensing of fluvial flows and remains an active field of research.

It is within this context that this Master Thesis aims to upgrade the knowledge in the domain of UAV-based LSPIV and, ultimately, to provide new opportunities for practitioners and academics to support their field campaigns in Hydraulic Engineering applications.

1.2. Problem Context

A crucial fundamental requirement in LSPIV is that the flow must be seeded adequately and homogeneously by high-visibility surface features, also known as 'tracers' (Jolley et al., 2021; Muste et al., 2008); existing literature and case studies generally apply flow seeding using artificial tracers. However, an important limitation of this approach is that proper artificial flow seeding is unworkable for large-scale water systems (e.g., wide rivers) (Bandini et al., 2021). Due to the impracticality of deploying artificial tracers, there is a compelling need for LSPIV approaches that allow for reliable surface velocity measurements in unseeded flows (Legleiter & Kinzel, 2020). Existing studies (e.g., Veldhuizen, 2021; Koutalakis et al., 2019) convincingly demonstrated that flows near hydraulic structures are potentially highly suitable for applying LSPIV to measure surface flow velocities. The interaction between the flowing water and hydraulic structure may give rise to strong turbulence associated with the dissipation of energy of the flowing water (Chanson, 2007); turbulence resulting from this interaction is often accompanied by foam and air bubble entrainment in the mixing layer. However, despite the aforementioned efforts, there is still limited knowledge and experience on using such natural features on the water surface as flow seeding in LSPIV. Furthermore, LSPIV has mainly used ground-based imaging platforms to obtain remotely sensed imagery for the purpose of measuring surface flow velocities (Jolley et al., 2021). A disadvantage of ground-based platforms is that they cannot be used to broadly image the water surface due to scale issues (Rhee et al., 2018). Moreover, it is often difficult to employ such platforms in inaccessible or hazardous environments. The use of UAVs in LSPIV has been recently explored and offers a solution to these limitations. Even though UAVs have been employed extensively in various research areas and fluvial applications already, the use of UAV-based approaches in LSPIV is still relatively uncommon (Rhee et al., 2018). Because of this, there is also little knowledge as to how UAV-based LSPIV performs compared to the conventional, ground-based LSPIV implementations (Tauro et al., 2016a,b). Lastly, even though the basic steps of the LSPIV workflow are generally well-established, there is still no clear precedence or research indicating which specific approaches or techniques are most suitable for the problem at hand. Because of this, the use of LSPIV to measure surface flow velocities still relies heavily on ad hoc, heuristic guidelines (Jolley et al., 2021). Previous studies have attempted to address this issue by proposing systematic guidelines for optimising the experimental conditions and parameter specification process. However, they often fail to move beyond the trial-and-error approach. A drawback of such heuristic approaches is that they give little insight as to how specific solutions or configurations affect the performance of LSPIV in measuring surface flow velocities.

The problem outlined in this section essentially amounts to the following: *research on the feasibility and efficacy of UAV-based LSPIV approaches to measure surface flow velocities in unseeded flows is severely lacking at the moment*. All in all, the research work presented in this thesis is primarily motivated by the fact that UAV-based LSPIV provides a novel, exciting and promising method for collecting reliable surface water flow velocity measurements for the purpose of studying flow phenomena in large-scale fluvial environments. Furthermore, the identified challenges and limitations are great incentives to explore the possibilities of using naturally occurring surface features as flow seeding in LSPIV.

1.3. Research Dimensions

1.3.1. Research objective

The main objective of this research is *to assess the feasibility of using drone-borne imaging techniques and LSPIV methods to infer surface flow velocities in unseeded flows within large-scale fluvial applications*. It is important to note that, in this case, unseeded flows refer to flows in which no artificial tracers are introduced and, thus, strictly rely on naturally occurring features to achieve flow seeding. Having said that, this research further explores the influence of various experimental conditions and image processing techniques on the LSPIV outputs.

The expected results are two-dimensional vector fields characterising the surface flow velocities of relevant flow phenomena in the selected study areas. These drone-based LSPIV surface flow velocity estimates ought to be obtained under different experimental conditions, such as different study areas,

natural surface seeding conditions, or flow regimes. Furthermore, different experimental set-ups and configurations ought to be tested; this implies that one should explore, for example, different imaging platforms (e.g., ground-based or aerial platforms), camera configurations (e.g., camera angles), sensor configurations (e.g., image resolution), drone flight altitudes, imaging durations, ground control point (GCP) arrangements, image processing parameter settings, etc. With this in mind, this research is also expected to provide a process-based explanation as to why or how certain methods are effective or ineffective when applying LSPIV in unseeded flows.

1.3.2. Research questions

Based on the defined research objective, the main research question is formulated as follows:

What are the capabilities that drone-borne imaging techniques and LSPIV methods hold for estimating surface flow velocities in unseeded flows within large-scale fluvial applications?

The main research question can be divided into three sub-questions:

I. How can drone-based LSPIV be utilised to derive surface flow velocity estimates in unseeded flows, and how do the different parameters associated with the main identified error sources influence these measurement results?

II. To what extent do the quantity and spatial distribution of naturally occurring tracing material constrain the applicability of drone-based LSPIV in unseeded flows?

III. How does drone-based LSPIV perform compared to traditional, fixed camera LSPIV implementations with regard to estimating surface flow velocities?

1.3.3. Research methods and thesis outline

This thesis is structured as follows: *Chapter 2* elaborates on the materials and methods used to facilitate the research work in this thesis; herein presented are the the LSPIV working principle, overview of the dominant error sources in LSPIV, methods used for the purpose of the accuracy assessment, sensitivity analysis method and, finally, description of the study areas. In essence, this chapter partially addresses research question 1 already by providing guidance for the LSPIV analyses. *Chapter 3* presents and discusses the findings of the research work; presented herein are descriptions of the field data, results of the LSPIV analyses, the assessment of the LSPIV performance, a comprehensive sensitivity analysis and, finally, a comparison between drone-based and fixed camera LSPIV implementations. By performing a sensitivity analysis, the second part of research question 1 is addressed. To answer research question 2, LSPIV analyses were performed considering different study areas with different seeding conditions. More specifically, experimental observations were conducted at several locations along the Dinkel River and Meuse River in the Netherlands. The last section of chapter 3 is aimed at answering research question 3. *Chapter 4* provides a discussion on the main themes of this thesis; it discusses the practical significance of drone-based LSPIV and compares relevant findings to the literature. Furthermore, the discussion presents the main limitations of the research and, accordingly, provides recommendations for future research. Finally, *Chapter 5* summarises the key findings of the research by answering the research questions.

In the appendices, supplementary material can be found, such as additional figures and an overview of relevant statistics. In *Appendix A*, additional figures are presented to give an impression of the data acquisition campaigns. *Appendices B* and *C* contain additional results of the LSPIV analyses. Finally, *Appendix D* presents additional analyses in support of the discussion.

2

Materials and Methods

2.1. Large-Scale Particle Image Velocimetry (LSPIV)

The purpose of this section is to explore the current understanding of LSPIV and to provide guidance for the LSPIV analyses in this thesis; this is done by assembling, in one place, all relevant information regarding the theoretical fundamentals of LSPIV. The first subsection (section 2.1.1) practically serves as a general summary of the LSPIV working principle. In said subsection, the key considerations in LSPIV were identified and, correspondingly, a comprehensive workflow for conducting LSPIV analyses was developed. The subsections thereafter will delve deeper into the topic of LSPIV and provide a more detailed explanation concerning the key processes of the LSPIV workflow. The methods and tools used in this thesis to infer surface water flow velocities from remotely sensed imagery coincide with the overarching framework explained in this section.

2.1.1. LSPIV workflow

Several research papers have been published in which the authors attempted to develop a generalised system of required processes for inferring surface flow velocities in fluvial settings from remotely-sensed imagery. Research papers that were frequently cited include, inter alia, Fujita et al. (1998), Meselhe et al. (2004) and Harpold et al. (2006); some more recent papers that were often invoked are, for example, Koutalakis et al. (2019), Legleiter & Kinzel (2020), Perks et al. (2019), Strelnikova et al. (2020) and Jolley et al. (2021). The LSPIV workflows existing in the aforementioned research papers were carefully examined; this was done with the specific aim of setting out a standard practice for determining surface water flow velocities using LSPIV. Based on the methods proposed by the literature, the key processes and considerations in drone-based LSPIV were identified; with this information, a detailed, modular workflow was developed to support the LSPIV process in this thesis (Figure 2.1). It is important to mention that the workflow depicted in Figure 2.1 is implemented primarily within the MATLAB environment, utilising various open-source toolboxes. More specifically, the proposed LSPIV workflow mainly incorporates functionalities from the PIVlab and RIVeR add-ons (Thielicke & Stamhuis, 2014; Patalano et al., 2017). In brief, PIVlab is a widely-used, GUI-based MATLAB add-on that enables one to perform flow velocity analyses through the application of the PIV algorithm (Thielicke & Stamhuis, 2014). The RIVeR (short for 'Rectification of Image Velocity Results') toolbox should essentially be viewed as an extension of PIVlab. RIVeR was specifically developed with an eye towards processing and correcting remotely-sensed imagery that suffer from distortions induced by the oblique viewing angle of the imaging platform and external effects (wind effects, imperfect hovering of drone, etc.). With this in mind, functionalities offered within the RIVeR toolbox were used for pre- and post-processing purposes, as will be explained in greater detail later in this chapter. That being said, based on the reviewed literature, it can be concluded that the LSPIV workflow comprises four main stages: (1) data acquisition and preparatory work; (2) image pre-processing; (3) image evaluation; and (4) post-processing. The key components of the LSPIV workflow are depicted in Figure 2.1 and the most important considerations for each of the four stages are summarised in the subsections below:

Stage 1: Data acquisition and preparatory work

In the first stage, one must select the study area and plan the data acquisition campaign accordingly. As was mentioned in the introduction, flow seeding is one of the key considerations in applying image

velocimetry for estimating surface flow velocities. The presence of features on the water surface is essential to obtain useful results from LSPIV. The surface features must be sufficiently large, contrast the colour of the water surface and homogeneously distributed across the water surface (Meselhe et al., 2004; Fujita et al., 1998). Flow seeding can be achieved by means of natural as well as artificial tracers. In this thesis, the focus will be exclusively on using naturally occurring water surface features as flow seeding. With this in mind, the study site ought to be selected based on whether features are prevalent on the water surface. Such features are, for example, advecting turbulent structures, natural debris, suspended-sediment clouds, foam and air bubbles produced by turbulent mixing of water, etc. Unfortunately, the abundance of such features and adequate seeding homogeneity are not very common in natural environments (Koutalakis et al., 2019). However, under the right conditions, the presence of, for example, hydraulic structures (e.g., storm surge barriers, dams, weirs, sluice gates, etc.) in water systems can generate the necessary natural surface features. The interaction between the flowing water and hydraulic structure may give rise to strong turbulence, which is typically accompanied by foam and air bubble entrainment in the mixing layer; these features may potentially be highly suitable for the application of LSPIV and, therefore, may circumvent the need for artificial flow seeding (Veldhuizen, 2021; Koutalakis et al., 2019; Legleiter & Kinzel, 2020).

Other important considerations during the first stage of the LSPIV workflow are the placement of ground control points (GCPs) and camera configuration (Jolley et al., 2021). The aforementioned considerations will be elaborated in more detail in sections 2.1.3 and 2.2.3, respectively. Moreover, it is crucial to understand the effects of external environmental factors on the LSPIV performance. The LSPIV performance was found to be fairly sensitive to external environmental factors such as precipitation, wind effects, fog, sun glare, etc. (Jolley et al., 2021; Hauet et al., 2008a). These factors tend to introduce much noise and distortions onto the imagery. On top of that, it is important to realise that drones can only be employed under certain conditions. Even though most drones are able to withstand brisk rain, drone flight in harsh weather conditions must be avoided at all costs, since the electrical components of the drone may sustain severe damages in such conditions. With this in mind, the environmental conditions should be kept in mind when planning the data acquisition campaign.

The final step of this stage involves the execution of the measurement plan. This entails that an image sequence of the water surface of the river reach of interest is acquired using a camera mounted on an airborne (drone, helicopter, etc.) or a terrestrial platform. Reference surface water flow velocities should be collected during the data acquisition campaign as well if possible. Ideally, the reference velocities are obtained using conventional velocimetry instruments, such as an ADCP or ADV; these field measurements serve as benchmark values and are necessary to quantitatively assess the accuracy of the LSPIV performance at a later stage of the LSPIV workflow (stage 4 in Figure 2.1). Considering this, the measurement plan must also stipulate how reference measurements will be collected in the field. In this study, however, it was not possible to obtain in-situ velocity measurements due to safety reasons and inaccessibility of the study areas; for this reason, an alternative approach was considered to obtain reference velocity measurements for the purpose of the accuracy assessment, as will be explained later in this thesis (section 2.3.1).

Stage 2: Image pre-processing

In the second stage of the LSPIV workflow, the raw imagery and corresponding field data acquired in the first stage are imported into the MATLAB environment. From within MATLAB, pre-processing is applied to prepare the image sequence for the computation of the velocity field using the PIV algorithm. As can be seen in Figure 2.1, the pre-processing stage involves a wide array of steps. The main purpose of pre-processing is to correct for image distortions induced by camera lens aberrations, camera movements, and off-nadir camera positioning; this is done using image transformation techniques, such as image stabilisation and orthorectification. The orthorectification procedure requires the establishment of (real-world) coordinates at the GCPs that were placed in the field. Figure 2.1 suggests that orthorectification can be applied either explicitly or implicitly; meaning that either the raw images (explicit) or the PIV-derived vector fields (implicit) are rectified. In the latter case, the orthorectification procedure is applied in the final stage of the workflow. Next, once the appropriate image transformations have been applied, the imagery must be enhanced in order to optimise the detectability and traceability of the tracers. Various image enhancement techniques exist for this purpose, as will be explained in section 2.1.4.

Finally, the region of interest (ROI) is delineated and masks are drawn onto the static features (e.g., river banks) that are visible in each image of the image sequence. The ROI is defined based on the stream portion where the surface flow velocities ought to be computed. The image transformations (image stabilisation, orthorectification, etc.) are mainly performed within the RIVeR environment, while the image enhancement is applied using the PIVlab toolbox.

Stage 3: Image evaluation

In the image evaluation stage, the PIV algorithm is applied to the pre-processed image sequence obtained from the image pre-processing stage. In essence, the PIV algorithm attempts to estimate the displacement of distinct patterns, composed of tracer particles, on the water surface through the application of a statistical pattern matching technique (Perks et al., 2019); more specifically, the cross-correlation function is used to achieve this (section 2.1.5). The PIV algorithm then relates the recorded displacements to the velocity field of the observed flow. PIV implementations operate according to the so-called Eulerian method of description, which is typically used to describe inter-dimensional flows within the context of experimental fluid mechanics (Jolley et al., 2021). The Eulerian method of description focuses attention on the movement of a fluid past given points in space (i.e., control volume) (Fox et al., 2016). This means that, in PIV, the properties of the observed flow are described as a function of fixed space coordinates and time. The core activity during this workflow stage is the selection of appropriate PIV parameter settings (Legleiter & Kinzel, 2020); the reader is referred to section 2.1.5 for a detailed explanation of the PIV working principle and the associated parameters. It is important to note that, prior to the velocity field computation, one must decide which sampling frequency (frame rate) and image sequence duration to retain (Jolley et al., 2021). The aspired outputs are two-dimensional vector fields representing the instantaneous surface flow velocities in the selected ROI.

Stage 4: Post-processing and further analyses

In the final stage, spurious vectors in the vector field are corrected and further analyses are performed. Post-processing of the LSPIV-derived vector fields may improve the accuracy of the velocity estimates (Jolley et al., 2021). This process mainly involves the detection of outliers in the LSPIV data through the application of statistical methods. The detected erroneous vectors are then removed and replaced by means of interpolation techniques (Thielicke & Stamhuis, 2014). If needed, additional processing of the vector fields can be performed prior to the vector corrections. As was explained earlier in this subsection (description stage 2), one can decide to apply orthorectification to the vector fields rather than to the raw images (i.e., implicit orthorectification); in this case, the vector fields generated by PIVlab are exported to a directory and imported back into the RIVeR toolbox. The final product of the LSPIV workflow proposed in this section is a corrected vector field representing the (time-averaged) surface flow velocities in the stream portion of interest. Finally, further analyses are required to determine whether the LSPIV-derived velocity fields are well able to quantitatively and qualitatively describe the observed flow patterns. To quantitatively assess the accuracy of the LSPIV performance, the LSPIV-derived surface flow velocities ought to be compared to the reference measurements obtained during the data acquisition campaign (stage 1).

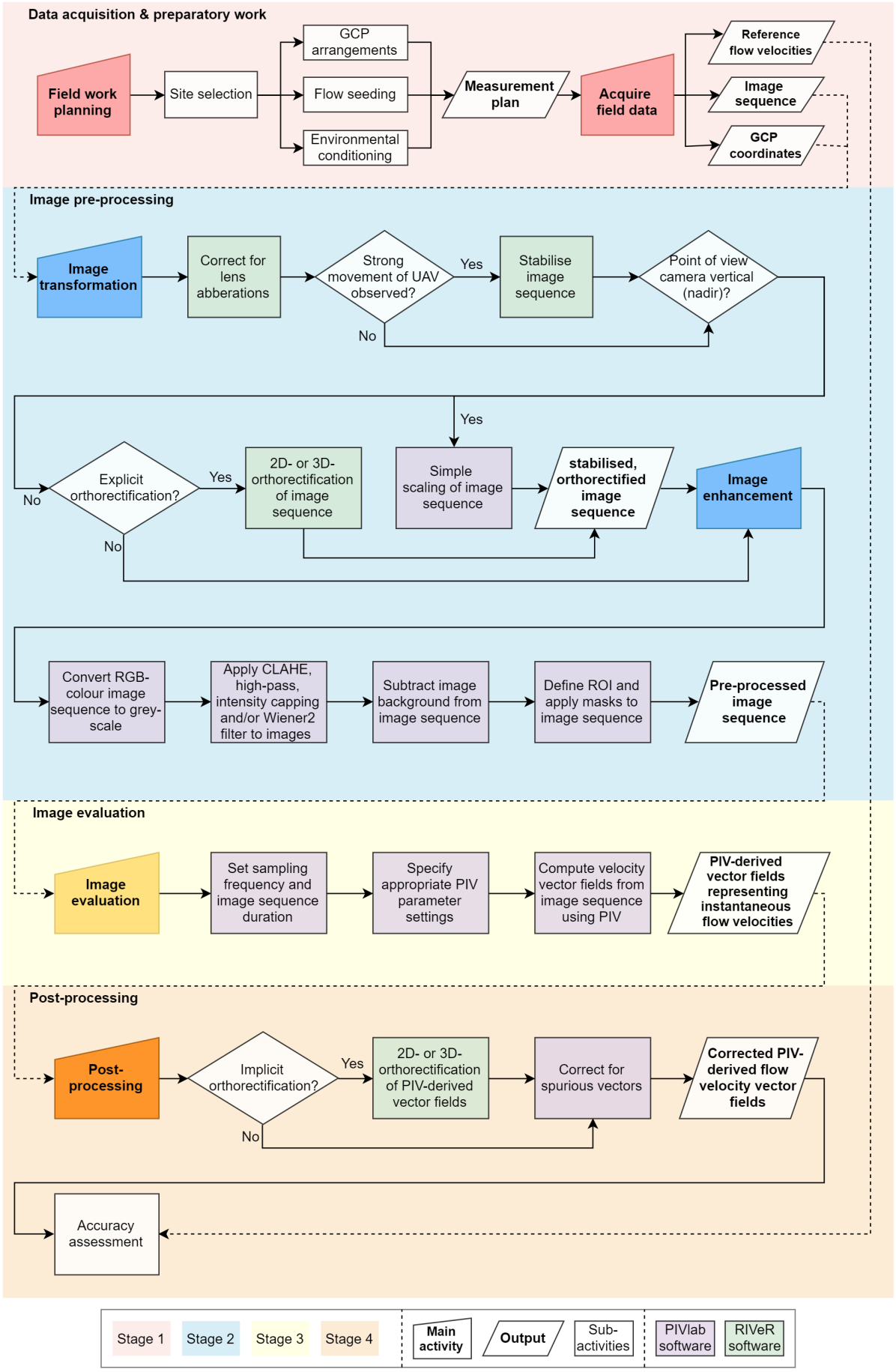

Figure 2.1: LSPIV workflow and generalised system of requirements in LSPIV to analyse surface flow velocities in fluvial environments. This flowchart is partially based on LSPIV workflows from the literature (i.e., Fujita & Komura, 1994; Legleiter & Kinzel, 2020; Jolley et al., 2021; Perks et al., 2019; Harpold et al., 2006; Meselhe et al., 2004)

2.1.2. Image stabilisation

Once the necessary field data have been acquired, stabilisation of the recorded videos may be required; this is especially true when a mobile or airborne imaging platform was used. In case of such imaging platforms, the quality of the recorded videos may suffer from unintentional and undesired effects. For example, imperfect hovering, wind effects and motor vibrations of the drone may lead to instability of the imagery. Consequently, the flow velocity estimations may be considerably impacted. As an example, the case study of Detert (2021) showed that velocity measurement errors could be reduced by 20% to 30% when correcting for residual movements of the imaging platform. The effect of applying image stabilisation to the raw drone-imagery is visualised in Figure 2.2; in the rightmost sequence of images in this figure, it can be seen that the undesired movement of the drone is eliminated by rotating and repositioning the frames such that the image sequence appears stable. The image stabilisation as shown in Figure 2.2 was applied using the image calibration tool of the RIVeR software; this tool is based on the so-called 'Point Feature Matching' algorithm. Tareen & Saleem (2018) outline the general steps of the Point Feature Matching-based approach for image stabilisation; in brief, the sequence of steps is as follows: (1) extracting a sequence of individual images from a video stream; (2) automatically detecting static features in the image; (3) matching of static features between images; (4) deriving a transformation function; and (5) reconstructing and stitching the images. For ground-based imaging platforms, image stabilisation is generally not required as the residual movements of the camera due to external factors (e.g., wind effects) are often negligible (Tauro et al., 2016b). In this study, image stabilisation was applied to drone-imagery for which strong movements of the camera was observed; this was done using the RIVeR software.

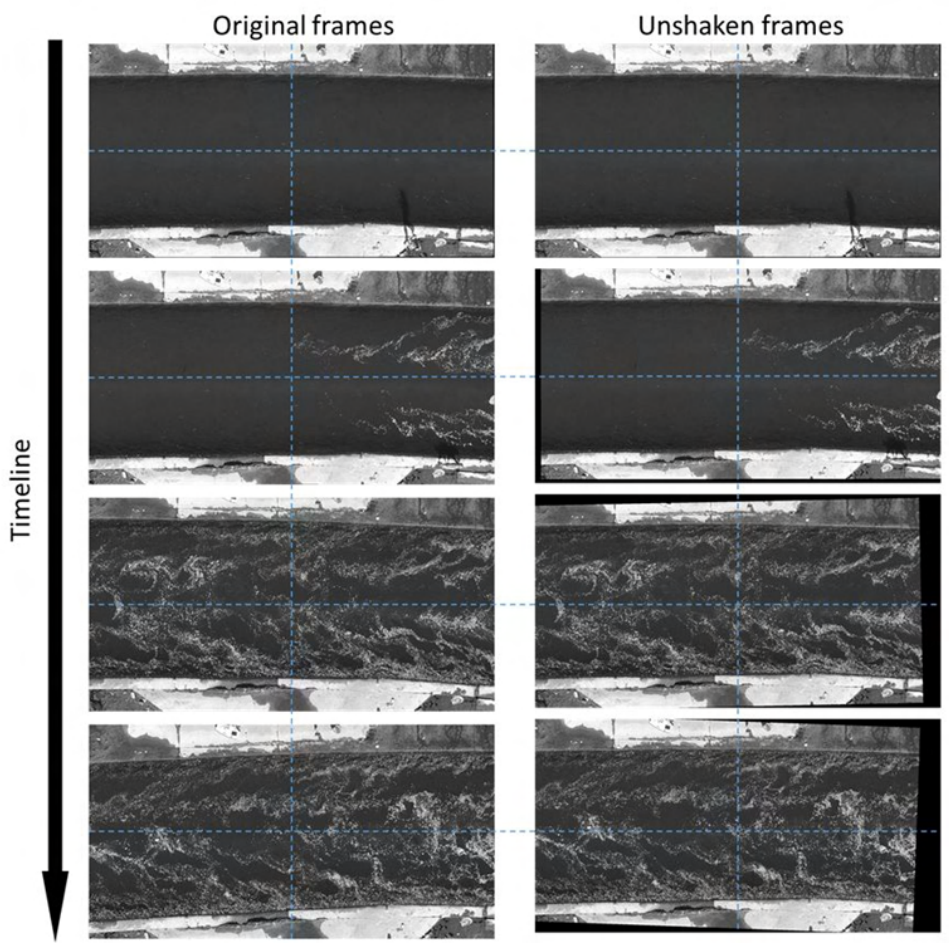

Figure 2.2: Example of applying stabilisation to an image sequence. The image sequence on the left hand side of the figure represents the raw, unstable imagery of the flow. The right hand side shows the same image sequence, but stabilised; stabilisation manifests itself through the appearance of black bars around the edge of the images as time progresses. Source: RIVeR (2020)

2.1.3. Orthorectification

Following image stabilisation, orthorectification of spatially distorted images is required in many cases. Spatial distortion, also known as perspective distortion, essentially prevails when images of the flow surface are recorded at an oblique angle (Figure 2.3). The process of orthorectification involves manipulating oblique images such that each pixel attains real-world dimensions (Perks et al., 2019). This process relies on so-called 'Ground Control Points' (GCPs). GCPs represent physical marker points in the field of view where real-world coordinates are established using GPS equipment. The established ground coordinates are then paired with the image coordinates (i.e., pixel locations) to rectify the spatially distorted image (Fujita et al., 1998; Muste et al., 2008). The relationship between the image coordinates (x, y) and the real-world ground coordinates (X, Y, Z) is generally established through the conventional photogrammetric relation as shown in Figure 2.3; the corresponding equation is expressed in Equation 2.1 (Aberle et al., 2017; Muste et al., 2008):

$$x = \frac{A_1X + A_2Y + A_3Z + A_4}{C_1X + C_2Y + C_3 + 1} \qquad y = \frac{B_1X + B_2Y + B_3Z + B_4}{C_1X + C_2Y + C_3 + 1} \tag{2.1}$$

Where:
A_1 *to* C_3 = *transformation coefficients*
X, Y *and* Z = *real-world coordinates of GCPs*
x *and* y = *image coordinates*

Using the known coordinates of the GCPs, the transformation coefficients in the above equation can be solved by using the so-called 'least square method'. For a more detailed explanation on this matter, the reader is referred to Muste et al. (2008). According to Muste et al. (2008), at least six GCPs are required to solve for the transformation coefficients. This is true in the case of 3D-transformation (Figure 2.3). 3D-transformation is generally applied when there are significant variations between the elevation of the water surface and GCPs. 2D-transformation, on the other hand, suffices when the GCPs are placed at a similar level as the water surface; in this case, a minimum of four GCPs is required (Fujita et al., 1998; Jolley et al., 2021). In this study, it was assumed that the GCPs were placed sufficiently close to the water surface. Therefore, only 2D-transformation was applied in this study. As a general rule, the accuracy of the image transformation can be increased by including more GCPs in the region of interest (Jolley et al., 2021). In addition to that, the GCPs should be placed directly around the region of interest.

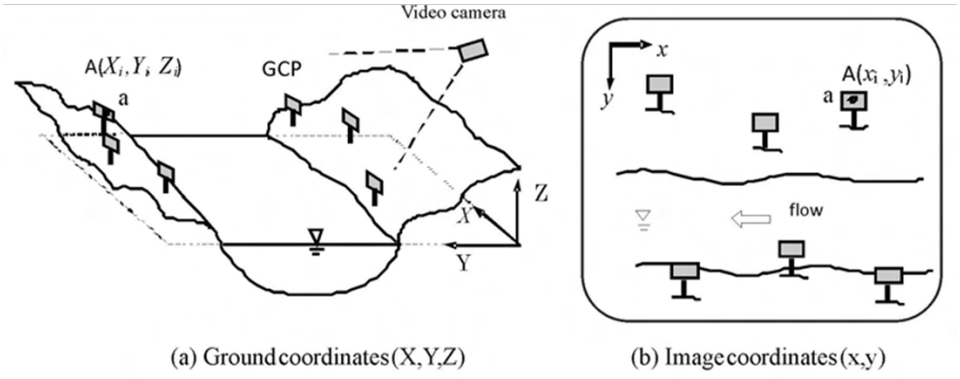

Figure 2.3: Relationship real-world coordinates and image coordinates. Source: Muste et al. (2008)

Once again, the image transformation tools available in the RIVeR software were used to orthorectify the acquired imagery. In the RIVeR software, the orthorectification process can be either explicit or implicit. This means that orthorectification can be applied to either the raw imagery (explicit) or to the LSPIV-derived velocity fields (implicit) (Jolley et al., 2021; Higham & Brevis, 2019). In the case of explicit orthorectification, the sequence of spatially distorted images is rectified prior to computation of the vector fields. Conversely, in the case of the implicit approach, orthorectification is applied to the

LSPIV-derived vector fields and not the raw imagery; which means that the vector fields are computed using the raw, unrectified imagery. At the moment, there is no general consensus regarding the appropriate orthorectification approach (Jolley et al., 2021). However, Higham & Brevis (2019) argue that applying orthorectification to the LSPIV-derived vector fields, rather than the raw imagery, may lead to more accurate velocity estimations. A possible reason for this could be that explicit orthorectification may introduce new, significant distortions onto the imagery. These distortions are likely to cause deterioration of the visibility of features on the water surface, which, in turn, may negatively affect the feature detection and tracking performance of the PIV algorithm (Higham & Brevis, 2019). In this study, both approaches were tested to determine whether explicit or implicit orthorectification is more effective in reducing the error associated with spatial distortions.

2.1.4. Image enhancement

A crucial fundamental requirement in LSPIV is that the flow must be seeded by high-visibility tracers. To optimise the detection and tracking performance of the PIV algorithm, it must be ensured that the features on the water surface are clearly distinguishable from the image background (i.e., water body colour). This stresses the importance of applying image enhancement techniques to the imagery. The main purpose of these techniques is to alter the intensity values of pixels across the image such that surface features visually contrast against the image background (Muste et al., 2008). First and foremost, the multi-spectral (RGB) images ought to be converted to greyscale (Jolley et al., 2021; Muste et al., 2008; Thielicke & Stamhuis, 2014). After greyscale-conversion, the imagery will only carry intensity information. Subsequently, further processing can be applied if necessary. The PIVlab software provides various image processing techniques, such techniques include: contrast limited adaptive histogram equalisation (CLAHE), intensity high-pass and, intensity capping. In brief, CLAHE is generally used to improve the local contrast in images; this means that areas with high or low exposure are optimised independently. This technique proved to be effective for images that show high variation in contrast levels. The high-pass filter removes low frequencies in the image background and retains high-frequency features (i.e., tracers). Thielicke & Stamhuis (2014) argue that inhomogeneous lighting conditions may result in low-frequency background information. With this in mind, the high-pass filter may be of particular interest for outdoor settings. For example, Strelnikova et al. (2020) found that the high-pass filter performed particularly well in fluvial settings with prevalent riverbed features (e.g. rocks, sand ripples, vegetation, etc.). Lastly, intensity capping aims to reduce the influence of very bright features by evening out the brightness across the image. Figure 2.4 shows the effects of the aforementioned processing techniques (i.e., CLAHE, intensity high-pass and intensity capping). Which particular technique to use is highly case-specific. In many cases, a trial-and-error approach is required to determine the appropriate enhancement technique and parameter settings. However, as a preliminary step, Patalano et al. (2017) recommend that CLAHE should be used for the application of PIV; based on this, CLAHE was used as the default filter in the LSPIV analyses performed in this study.

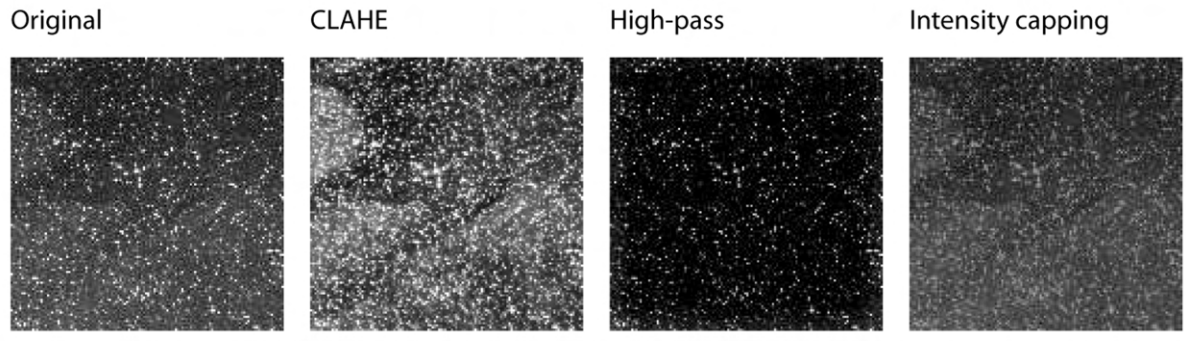

Figure 2.4: Available image enhancement options in the PIVlab software. Source: Thielicke & Stamhuis (2014)

2.1.5. Image evaluation

As a next step, the pre-processed images are evaluated through the application of image velocimetry. Image velocimetry is a technique involving the generation of a vector field representing flow velocities across a certain field of view (FoV). This velocity field is computed by applying statistical pattern matching techniques to an image sequence or video recording (Perks et al., 2019). The primary goal of such imaging techniques is to measure the displacement of distinct features in the flow. The feature displacements between successive images are determined within so-called, pre-defined 'searching areas' in the FoV. Firstly, each image in the image sequence is divided into a grid of interrogation areas (Figure 2.5a). Then, an interrogation area is selected in the first image ($t = t_0$) (Figure 2.5b). The features captured in the selected interrogation area in the first image are then compared to those captured in equally sized windows within the searching area in the second image ($t = t_0 + \Delta t$). In order to determine positions of pronounced correspondence between the image pair, image velocimetry algorithms typically calculate the cross-correlation coefficient between the selected interrogation area in the first image (e.g., window P in Figure 2.5b) and all possible windows within the searching area in the second image (e.g., windows Q, R, etc. in Figure 2.5c). The distance between the pair of features showing the maximum equivalence is assumed to be the most probable displacement of the features (Fujita et al., 1998; Muste et al., 2008). The corresponding velocity vector is then determined by dividing the measured displacement by the timestep between the successive images (Δt) (Fujita et al., 1998). A two-dimensional vector field is obtained once the velocity vectors are computed for all interrogation areas in the FoV. The local flow patterns, with a certain velocity magnitude and direction, can be inferred from this vector field. A simplified schematisation of the image-based velocimetry procedure as described above is illustrated in Figure 2.5.

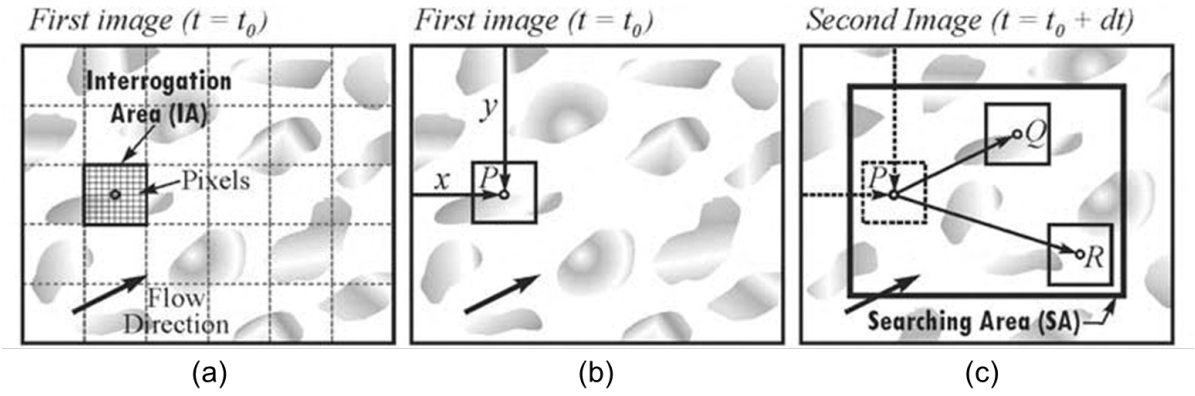

Figure 2.5: Schematisation of the PIV algorithm interrogation procedure. The sequence of steps is as follows: (a) divide each image in the image sequence into a grid of interrogation areas; (b) select an interrogation area P in the first image; (c) compute the cross-correlation coefficient between interrogation area P of the first image and all possible windows (Q, R, etc.) within the searching area in the second image; finally, determine the most probable displacement of the features based on the window match that shows maximum correspondence. This process is repeated for all interrogation areas. Source: Muste et al. (2008)

Various image-based velocimetry methods exist at the moment, examples are: PIV, particle tracking velocimetry (PTV) and space-time image velocimetry (STIV). In this thesis, the focus is on the PIV algorithm exclusively. PIV essentially follows the same procedure as described above (Aberle et al., 2017). Traditionally, PIV is applied in laboratory conditions in the context of experimental fluid mechanics. In PIV, the flow velocities are measured non-intrusively using an optical camera. A crucial fundamental requirement in conventional PIV is that the flow must be artificially seeded by so-called 'tracers' (Fujita et al., 1998). Using these tracers, PIV determines the displacements by calculating the spatial cross-correlation. The cross-correlation function, $\phi(m', n')$, for a window pair within a searching area is computed as follows (Aberle et al., 2017):

$$\phi(m', n') = \frac{A}{\sqrt{B \cdot C}} \tag{2.2}$$

with the following expressions for A, B and C respectively:

$$A = \sum_{m,n=0}^{W-1} \eta(m,n)\Big(g(m,n) - \mu_g\Big)\eta(m+m', n+n')\Big(h(m+m', n+n') - \mu_h\Big) \tag{2.3}$$

$$B = \sum_{m,n=0}^{W-1} \Big[\eta(m,n)\Big(g(m,n) - \mu_g\Big)\Big]^2 \tag{2.4}$$

$$C = \sum_{m,n=0}^{W-1} \Big[\eta(m,n)\Big(h(m,n) - \mu_h\Big)\Big]^2 \tag{2.5}$$

where W is the size of the windows (or interrogation areas), $g(m,n)$ and $h(m,n)$ are the grey-level intensity distributions of the first and second window respectively, μ_g and μ_h represent the mean grey-level intensity values of the respective windows and, finally, m' and n' are the spatial offsets of the second window with respect to the first window; in this case, the first window refers to the selected interrogation area in the first image (Figure 2.5b). For an 8-bit image, grey-level intensity values range between 0 and 255 (Muste et al., 2008); furthermore, it is worth noting that the units of the interrogation area size and image coordinates are generally expressed in terms of image pixels. Optionally, to improve the measurement accuracy, a weighting window, η, can be included in the cross-correlation computation. An example of the implementation of cross-correlation between two matching interrogation areas is depicted in Figure 2.6. In essence, the cross-correlation function (Equation 2.2) is calculated in two dimensions and the location of the correlation peak is determined (Figure 2.6b, c and d). The coordinates of the correlation peak are commonly determined with sub-pixel precision. This means that the position of the correlation peak ought to be refined by means of interpolation techniques. An example of a commonly used interpolation technique is the so-called 'three-point Gaussian fit', which is also used by the PIVlab toolbox (Thielicke & Stamhuis, 2014). From the discrete coordinates of the maximum correlation coefficient, the displacements (Δx_1 and Δx_2) of the tracers within the interrogation area can be inferred.

Once the displacements and the corresponding timescale are known, the velocity vector can be simply calculated using the following expression (Aberle et al., 2017; Fujita et al., 1998):

$$\vec{V} = M \cdot \frac{\vec{d}}{\Delta t} \tag{2.6}$$

Where:
$\vec{V}$ = *velocity vector for an interrogation area*
$\vec{d}$ = *feature displacement (in pixel units)*
M = *magnification factor*
Δt = *time interval between successive images*

a magnification factor then ought to be applied to obtain a velocity vector in terms of metric units. Finally, a velocity field is obtained once the velocity vectors have been computed for each interrogation area.

As was mentioned earlier, PIV was initially developed for laboratory conditions to study small-scale flows. However, developments in the past three decades facilitated the use of conventional PIV in large-scale fluvial environments (Aberle et al., 2017; Fujita & Komura, 1994). Using PIV to study large-scale flow phenomena is often referred to as LSPIV. The processes of PIV and LSPIV are fundamentally the same. However, there are some important differences. While PIV is generally used to study (small-scale) internal flow patterns, LSPIV is used to measure flow velocities at the free surface of water bodies. Furthermore, in LSPIV, features on the water surface advected by the flowing water are used as tracers. They can be artificial tracers as well as naturally occurring surface features (e.g. foam generated by turbulence patterns). Finally, recent efforts showed that mobile and aerial platforms (e.g. UAVs) can

be employed to acquire image recordings for the application of LSPIV. In this thesis, the main focus will be on UAVs, such as drones. However, it is important to realise that there are many different technical and practical challenges that might affect LSPIV-derived velocity measurements. Understanding the errors associated with LSPIV is essential in order to obtain meaningful results (Aberle et al., 2017). For the remainder of this thesis, the focus will be on LSPIV exclusively.

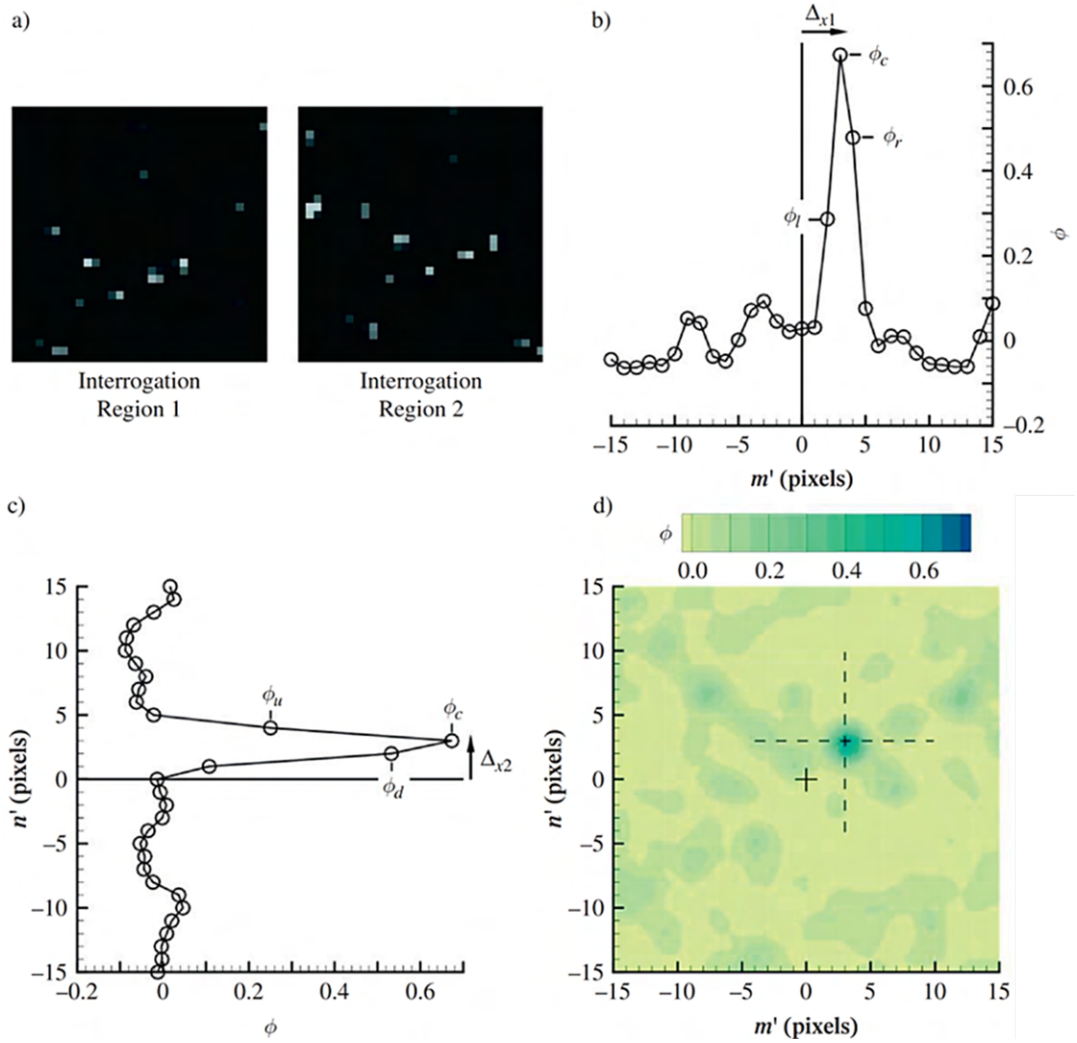

Figure 2.6: Example of the implementation of cross-correlation on an image pair in PIV. The figure depicts two matching interrogation areas and the corresponding cross-correlation distribution in two dimensions resulting from the procedure shown in Figure 2.5. (a) interrogation area pair; (b), (c) and (d) calculated cross-correlation functions in two dimensions. Source: Aberle et al. (2017)

2.1.6. Post-processing

Post-processing must be carried out to obtain reliable flow velocity estimations. Post-processing primarily involves the removal of spurious velocity vectors (Figure 2.7a). The PIVlab software uses a fairly simple outlier detection method for the aforementioned purpose; more specifically, erroneous velocity vectors are detected in the PIVlab software by manually defining the lower and upper limits for acceptable velocities (Thielicke & Stamhuis, 2014). If a particular velocity component does not fall within these limits, it is simply removed. In this study, the velocity limits were specified based on the values of the horizontal and vertical velocity components (u, v) of obvious outliers in the time-averaged vector field; these 'obvious' outliers were visually identified by generating a scatter plot of the LSPIV velocity measurements. The appropriate velocity limits for post-processing in this study were highly case-specific; for example, typical velocity limits for the Dinkel River study area would be 0.0 to 0.72 m/s and -0.30 to 0.28 m/s for the horizontal and vertical velocity components, respectively. In the case

of the Sambeek Weir study area, representative velocity limits are -0.10 to 0.71 m/s and -0.20 to 0.13 m/s for the horizontal and vertical velocity components, respectively. After removal of the erroneous vectors, the missing vectors (Figure 2.7b) are replaced by means of interpolation techniques. The PIVlab software uses a boundary value solver approach for interpolation. More specifically, PIVlab uses the so-called 'inpaint_nans' MATLAB function, which was originally developed by D'Errico (2022) (Thielicke & Stamhuis, 2014). The 'inpaint_nans' interpolator essentially solves a partial differential equation (PDE) to ensure that the interpolated values are consistent with the neighbouring values. Finally, data smoothing is applied to reduce noise caused by image processing. A simplified schematisation of the post-processing procedure is visualised in Figure 2.7.

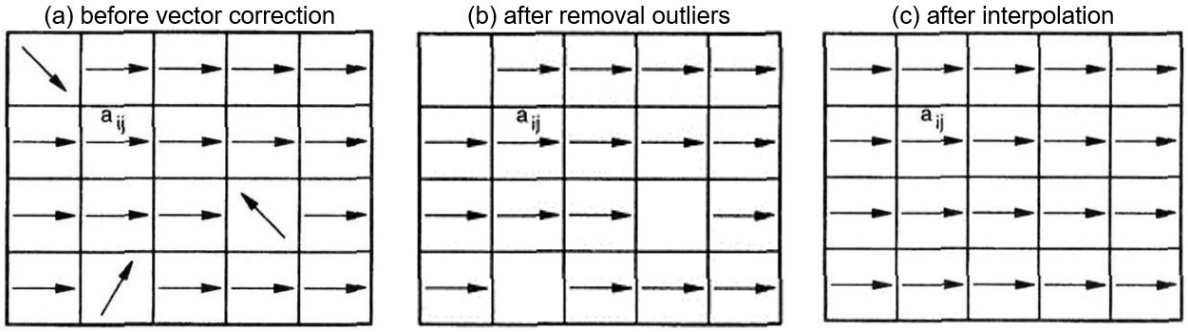

Figure 2.7: General procedure for correction of erroneous vectors. Source: Fujita et al. (1998)

2.2. Sources of error in LSPIV

This section will discuss relevant sources of uncertainty in drone-based LSPIV that may significantly influence the flow velocity estimation accuracy. Based on the results presented in existing research papers (e.g., Legleiter & Kinzel, 2020; Tauro et al., 2016a; Strelnikova et al., 2020), it may be concluded that drone-based LSPIV holds much potential in Hydraulic Engineering applications. However, one must realise that LSPIV technology and the results that it produces are still far from perfect (Sciacchitano, 2019). Due to various (practical) challenges and limitations, flow velocity measurements are subject to error. In order to effectively reduce the errors associated with drone-based LSPIV, it is essential to get a better understanding of these potential sources of error. On top of that, an important element of this thesis is the assessment of the sensitivity of velocity estimations to parameters associated with the main identified error sources in LSPIV; with this in mind, all known uncertainty sources must be properly acknowledged prior to the sensitivity analysis (SA) (Saltelli et al., 2006).

2.2.1. Flow seeding

Tracer size

Amongst existing literature and case studies, there exists a substantial variation regarding the adopted tracer sizes in LSPIV implementations. The aforementioned statement is reinforced by an extensive literature review of Sharif (2022), in which the tracer characteristics of 17 recent case studies were examined; it was found that tracer diameters used in these case studies generally ranged between 1 and 30 mm. A limited number of case studies even used tracers up to tens of centimetres in diameter. The disparity in the literature indicates that there is no clear precedence as to how large the tracer particles must be. Nevertheless, a general rule of thumb exists to provide guidance for the selection of appropriate tracers. It is suggested that the tracer particles must have a diameter of at least 1 or 1.5 pixels (px) in the images (Dal Sasso et al., 2020; Liu et al., 2021; Weitbrecht et al., 2002); diameters smaller than this may lead to significant measurement errors, as the PIV algorithm may not be able to recognise the tracers on the water surface in this case. Therefore, the appropriate tracer size also strongly depends on the image resolution and ground sampling distance (GSD). Based on the above information, it can be concluded that the tracer size is an important source of uncertainty and should be kept in mind when conducting the LSPIV analyses.

Seeding density and homogeneity

Next to the tracer size, the density and homogeneity of flow seeding are crucial controls of the velocity estimation accuracy (Aberle et al., 2017). Raffel et al. (2018) claim that a reduction of detectable and traceable features on the flow surface may result in a large number of spurious vectors in the LSPIV velocity field output. For example, a study carried out by Bandini et al. (2021) showed that low-density and inhomogeneous seeding contributed to flow velocity measurement errors between 15% and 45%. In Dal Sasso et al. (2020), inhomogeneous seeding resulted in measurement errors up to 81%. Despite the efforts of the aforementioned research papers, quantitative guidelines regarding the seeding density are still lacking at the moment. However, Meselhe et al. (2004) found, by means of a process-based sensitivity analysis, that flow tracers must cover 10% to 30% of the flow surface in order to minimise measurement errors. Additionally, it is essential that the tracers are distributed uniformly across the water surface as much as possible; otherwise, LSPIV may erroneously show low- or zero-velocity spots scattered around the generated vector fields.

Tracer visibility

In LSPIV, one must ensure that the tracer material on the water surface visually contrasts the image background (i.e., water colour). As was mentioned in section 2.1.5, the PIV algorithm attempts to estimate the displacement of distinct patterns in the flow by computing the cross-correlation function based on pixel intensity values. With this in mind, high contrast of water surface features greatly favours the image evaluation process, as the PIV algorithm is much better able to recognise and track features in successive images (Hauet et al., 2008b). Conversely, tracers that poorly contrast the image background tend to induce much error in the LSPIV results. In outdoor settings, it was found that a bright and colourful or a light colour palette is appropriate in many cases (Tauro et al., 2016a).

Tracing error

Additional errors in the flow velocity estimates may be induced by flow-independent motions of the tracer particles. This means that, under the influence of wind effects or other free surface processes, there is a difference between the true surface water flow velocity and the velocity of the tracers. This type of error especially prevails for tracer particles that have low specific gravity, such as foam and air bubbles (Sciacchitano, 2019). Moreover, clustering of tracer particles may also lead to measurement inaccuracies, as the appearance of patterns on the water surface may change over time. This phenomenon is likely to affect the ability of the PIV algorithm to recognise and match patterns in successive images (Aberle et al., 2017).

2.2.2. Ground sampling distance

Whether the camera system can resolve the tracers on the flow surface strongly depends on the image GSD (size of one image pixel) (Jolley et al., 2021). The GSD, in turn, is dictated by the drone flight altitude and camera specifications. A higher flight altitude of the drone generally results in coarser resolution images with a larger GSD. If the GSD is too large (or tracer particles too small), the features of the flow surface might not be resolved by the camera and the LSPIV procedure will be less accurate (Liu et al., 2021; Weitbrecht et al., 2002). As a general rule, the GSD must be smaller than the features present on the flow surface. Based on this, one might argue that the GSD must be as small as possible in order to optimise the LSPIV performance. However, Legleiter & Kinzel (2020) showed that a fine image resolution might have an adverse effect on the LSPIV measurement accuracy; this can often be attributed to the fact that the image pixels are small relative to the size of the advected surface features. Legleiter & Kinzel (2020) found that carefully increasing the GSD might actually enhance the detectability and traceability of water surface features; this is especially true in the presence of naturally occurring surface features, as they tend to be relatively large in size (Legleiter & Kinzel, 2020). Based on this information, the GSD can be an important source of error. Therefore, the appropriate GSD (or drone flight altitude) should be carefully chosen.

2.2.3. Camera tilt angle

Another important source of error relates to the camera configuration. More specifically, imaging at oblique angles with respect to the water surface (Figure 2.8a,c) may result in significant measurement inaccuracies. If one decides to perform explicit orthorectification (section 2.1.3), it is important to realise that the transformed image will be less accurate after the rectification procedure. The level of inaccuracy that is introduced in the image after (explicit) orthorectification depends on the tilt angle of the camera (Hauet et al., 2008a). As can be seen in Figure 2.8, the orthorectified images look different from the original images; the patterns from the original images are not well reconstructed. This is especially true for images recorded at a more significant tilt angle (Figure 2.8c,d). Through a sensitivity analysis, Hauet et al. (2008a) evaluated the influence of varying camera tilt angles (i.e., 55° and 70°) on the LSPIV measurement accuracy. They found an error variance up to 17%, which indicates that the tilt angle is indeed an important source of error. Based on these findings, Hauet et al. (2008a) recommend keeping the camera tilt angle as small as possible. Ideally, the images should be recorded at nadir. This way, orthorectification is not required and the LSPIV procedure will be more accurate (Hauet et al., 2008a; Jolley et al., 2021; Kim, 2006).

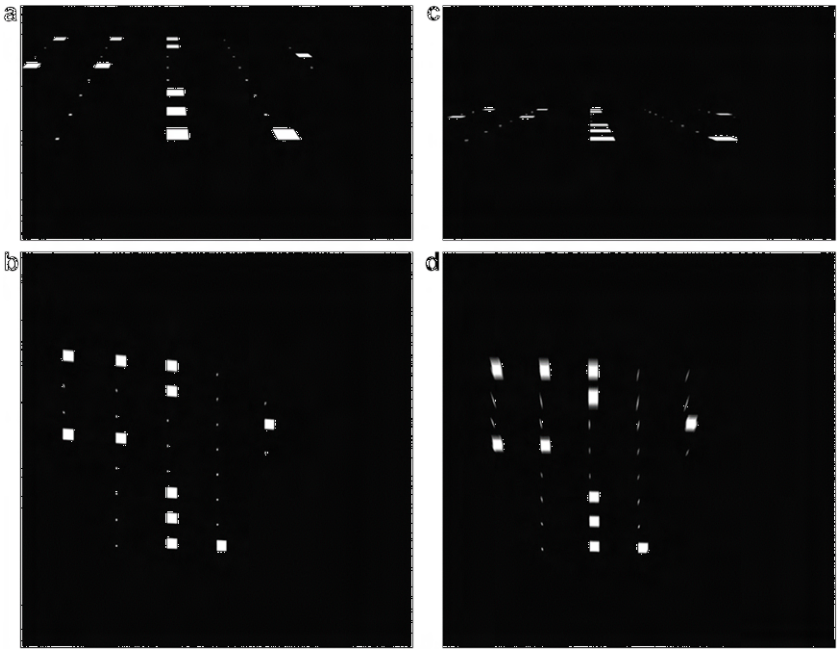

Figure 2.8: Effect of orthorectification on the same image with different camera tilt angles of respectively (a) 55° and (c) 70°. Source: Hauet et al. (2008a)

2.2.4. External environmental factors

The sources of error discussed in this subsection relate to the physical system. External environmental factors such as precipitation, fog, wind, illumination non-uniformity, and glare may impact the performance of the LSPIV application considerably (Jolley et al., 2021). Precipitation and fog induce much noise on the water surface, making the imagery unusable for LSPIV applications. Furthermore, global and local illumination of the water surface strongly affects the quality of the image-based velocity measurements (Hauet et al., 2008a). The global illumination, or overall sunlight intensity, must allow for adequate visibility of the surface features. Therefore, images cannot be collected under low-light conditions, such as dusk and night-time. Additionally, local illumination non-uniformity, due to shade and sunlight glare, is also an important error source in LSPIV (Hauet et al., 2008b; Peña-haro et al., 2020). Problems related to non-uniform illumination can generally be avoided by planning the data acquisition campaign during overcast weather. Finally, drones can only be operated under certain conditions. Keeping this in mind, precipitation and fog should be avoided at all costs, as it is difficult to operate a drone in these conditions.

2.2.5. Other sources of error

Only a selected number of error sources were outlined in the subsections above. However, many more error sources exist for (drone-based) LSPIV. Kim (2006) identified 27 different sources of error that all potentially affect LSPIV measurements in the context of studying fluvial flows. Not all error sources were analysed in the previous sections. Neither will they be in this subsection. However, it is interesting to list other relevant error sources that may affect the LSPIV results. Below, some of these elemental errors, as identified by Kim (2006) and Sciacchitano (2019), are listed and very briefly described:

- *Background noise* – In outdoor fluvial settings, the background is often non-uniform. In such environments, image noise is practically unavoidable. Many different factors may induce noise in the image recordings (e.g., features on the bed in clear-water streams). This may lead to deterioration of the image quality and, therefore, affects the usability of LSPIV applications.
- *GCP error* – GCP errors, or surveying errors, can result from inaccuracies associated with the establishment of real-world coordinates at GCPs during the data acquisition campaign. This may lead to image transformation errors and, therefore, may affect the LSPIV measurements.
- *Interrogation area* – During the image processing stage, one must determine the interrogation area size in the PIV software. The appropriate interrogation area size strongly depends on the size of the traceable surface features. If the interrogation area is too small, the PIV algorithm may not be able to detect and trace these features. This will lead to measurement errors.
- *Out-of-plane motion* – Out-of-plane displacements of particles commonly occur for highly three-dimensional flows. Such displacements may lead to loss of detectable particles and, therefore, may influence the performance of the PIV algorithm.
- *Sampling frequency* – The sampling frequency (or frame rate), that is the time interval at which successive images are recorded, deserves careful consideration, as it directly impacts the flow velocity computation. If the sampling frequency is too high, the displacements of particles between successive images may become excessively small; this will likely lead to significant error, as the PIV algorithm may be unable to detect tracer displacements. On the other hand, if the sampling frequency is too small, the frame-by-frame particle displacement may exceed the scope of the searching area, causing loss of correlation between image pairs (Pumo et al., 2021).

2.3. Accuracy Assessment

2.3.1. Reference measurements using float method

In this study, the so-called float method was used to quantify the surface water flow velocities; the resulting reference velocity estimates were used to facilitate the accuracy assessment. The working principle of the float method is relatively straightforward; in this method, a buoyant object is allowed to drift in the stream for a known distance. The time needed for the object to displace over that distance is then used to calculate the surface water flow velocity (Liu et al., 2021; Hilgersom & Luxemburg, 2012). Standard practice is to manually release objects into the stream and record the time it takes for these objects to travel a certain distance using a stopwatch (Liu et al., 2021). However, in this study, the float method was applied retroactively by inspecting the video recordings of the drone; this means that naturally occurring features on the water surface (i.e., foam and air bubbles) were visually tracked in the video recordings. Using the distance measurement tool of the MATLAB Image Viewer add-on, the travel distance of the features could be deduced. An advantage of this retroactive approach is that the flow velocity can easily be determined at several points along the stream. With this in mind, a grid consisting of several grid nodes was established onto the stream portion of interest (e.g., see Figure 3.11). The grid nodes represent the measurement points in this case. The average surface flow velocity was determined at each of the measurement points by tracking surface features along a certain linear trajectory. Figure 2.9 provides an example of how the float method was applied in this study to obtain reference velocity measurements. To minimise error, Dobriyal et al. (2017) argue that 5 to 10 features should be recorded along each trajectory.

Important reasons for using the float method are the operational ease, cost effectiveness, and time effectiveness (Dobriyal et al., 2017). Moreover, the float method can be categorised as non-polluting,

since it is non-intrusive and no harmful substances are deployed in the water system. Furthermore, in this study, the flow conditions at the selected study areas do not allow for safe in-situ data collection. Therefore, the float method is considered a good alternative to the other methods. However, one should realise that significant measurement error due to human factors is more likely to occur; because of this, the float method is often regarded as less accurate compared to methods that utilise advanced velocimetry instruments (Dobriyal et al., 2017). Even though the float method may be less accurate, it still provides educated estimates suitable for validation purposes (Hilgersom & Luxemburg, 2012).

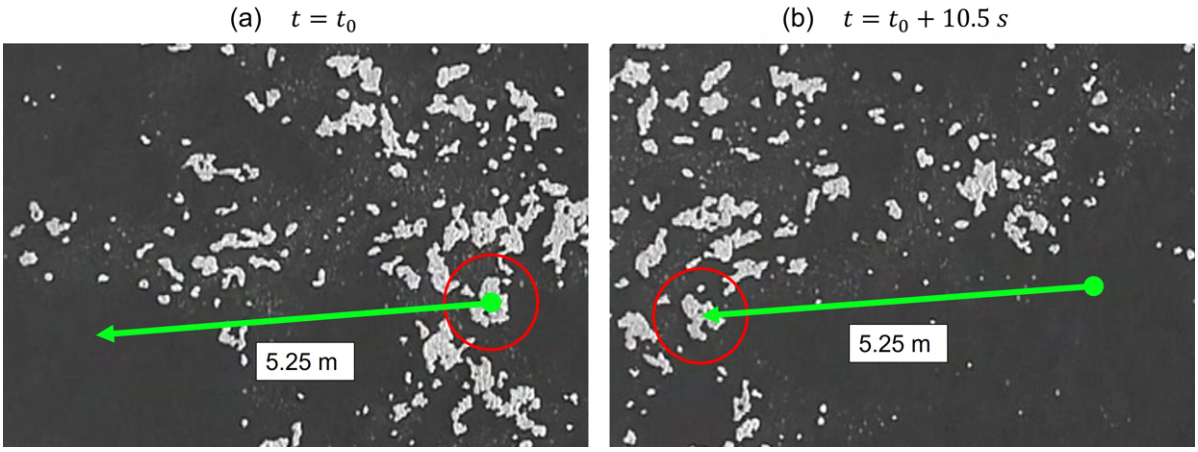

Figure 2.9: Example float method. To determine the surface water flow velocity, patterns on the water surface are tracked along a linear trajectory for a certain period of time. Red solid circle highlights the pattern that is tracked; green dot represents the location of the tracked pattern at time $t = t_0$; green arrow shows the trajectory which is travelled by the pattern during a time period of 10.5 s. The velocity is simply calculated by dividing the travelled distance with the travel time. In this example, a velocity of approximately 0.5 m/s (5.25m/10.5s) was measured.

2.3.2. Statistical error

To assess the performance of the LSPIV analyses in this study, the LSPIV-derived surface water flow velocities were compared to benchmark values obtained using the float method (section 2.3.1). Various error metrics were calculated to quantify the error between the LSPIV results and benchmark values. More specifically, the mean bias error (MBE) and root mean squared error (RMSE) were calculated. The MBE was adopted to summarise the average error in the velocity estimations and reveal whether LSPIV underestimates or overestimates the velocity; in this study, a negative MBE value suggests that the LSPIV-derived velocities are greater than the velocities obtained using the float method. A positive MBE, on the other hand, indicates underprediction of the flow velocities by LSPIV (Legleiter & Kinzel, 2020). The RMSE is also a commonly used error metric that serves as a precision index of the LSPIV results. Additionally, the obtained MBE and RMSE values were normalised using the mean surface water flow velocity magnitudes obtained from the float method; this was done to facilitate the comparison of error metrics between different locations considered in this study. Without further delay, the MBE can be calculated in the following manner (Liu et al., 2021):

$$MBE = \frac{1}{N}\sum_{i=1}^{N}(V_i^o - V_i^p) \tag{2.7}$$

The RMSE can be expressed as:

$$RMSE = \sqrt{\frac{1}{N}\sum_{i=1}^{N}(V_i^o - V_i^p)^2} \tag{2.8}$$

where V_i^o indicates the observed velocity magnitude at measurement point i obtained from the float method, V_i^p expresses the LSPIV-derived time-averaged velocity magnitude at measurement point i, and N denotes the total number of measurement points in the ROI.

2.4. Sensitivity Analysis

An important objective of this research is to gain insight as to how different experimental configurations and parameter settings affect the LSPIV-derived surface flow velocity estimations. It is within this context that this research performed an extensive sensitivity analysis (SA). A SA is particularly interesting in this case; this is true as it allows for the identification of which particular experimental configurations and parameter settings are the main controls of the model behaviour and, hence, are most responsible for good performance of the PIV algorithm (Saltelli et al., 2006). The SA performed was mainly based on the so-called 'one-factor-at-a-time' (OAT) method. In OAT, one parameter is varied each time while the other parameters remain fixed at their nominal (baseline) value. The SA in this study distinguishes between the sensitivity to experimental configurations and image (pre-)processing. Experimental configurations, in this case, refer to parameters related to the data acquisition (stage 1 in Figure 2.1), while image (pre-)processing focuses attention on mainly image manipulation and PIV parameter-settings (stage 2 and 3 in Figure 2.1). Finally, various error metrics (RMSE, MBE, etc.) were computed to quantitatively assess the sensitivity of the LSPIV outputs; additionally, velocity fields and velocity profiles along predefined transects were generated as well for qualitative assessment purposes.

2.4.1. Experimental configurations

Practical questions regarding remote sensing of surface water flow velocities were addressed by doing a SA on relevant experimental configurations. Based on the potential error sources identified in section 2.2, the following aspects were taken into account in the SA:

- *Camera tilt angle* – During the data acquisition campaign, drone-borne imagery was collected at varying camera tilt angles. This was done to analyse the influence of spatial distortion effects on the LSPIV-derived velocity fields. As part of the SA, the orthorectification procedure was applied both explicitly and implicitly.
- *Drone flight altitude* – It was established earlier that the GSD, or image pixel size, is potentially an important uncertainty source. The GSD is partially dictated by the height at which the images are captured. Therefore, the data acquisition campaign also involved recording the water surface at different drone flight altitudes.
- *Image sequence duration* – LSPIV analyses were performed using image sequences of different durations to address the practical question of how long the flowing water should be recorded to obtain reliable velocity estimations. The whole-field, time-averaged surface flow velocity magnitude was computed and plotted as a function of the image sequence duration; the time it would take for the average velocity magnitude to stabilise is considered to be an estimate of the 'optimal' measurement time (Clasing & Muñoz, 2018). The analyses were performed using image sequences with sampling frequencies of respectively 10, 30 and 60 Hz; this was done to account for the possible confounding effect of the sampling frequency (Legleiter & Kinzel, 2020).

2.4.2. Image (pre-)processing

Below, the image (pre-)processing parameters that were considered in the SA are described:

- *Sampling frequency* – The high-frequency sampling capabilities of the camera system mounted on the drone allowed for the exploration of the effects of the sampling frequency (frame-rate) on the LSPIV output. In the SA, sampling frequencies ranging from 2 to 60 Hz were tested.
- *Image resolution* – As was explained in the previous subsection, the sensitivity of the LSPIV results to the GSD was assessed in this study by considering different drone flight altitudes. However, only a limited number of altitudes could be tested at the time of the data acquisition campaign. To enable more rigorous testing of the effects of the GSD on LSPIV, the GSD of the acquired image sequences was also changed artificially; this was done by repeatedly resampling the original image sequence, such that it attained a resolution ranging from coarse (1280x720 px) to very fine (3840x2160 px).
- *Interrogation area size* – In LSPIV implementations, interrogation areas commonly vary between 16 to 512 px and often attain a value that is the power of two (e.g., 16, 32, 64, etc.) (Legleiter & Kinzel, 2020; Aberle et al., 2017); these values were also considered in the SA. However, an

interrogation area of 512 px was found to be unreasonably large and, therefore, a value of 320 px was considered instead. Correspondingly, the searching area size was set at 50% of the interrogation area size.

- *Image enhancement technique* – The following filters were applied to the image sequence prior to the velocity field computation: CLAHE, high-pass, intensity capping and, Wiener2 denoise and low-pass filters. In LSPIV, it is also common practice to apply multiple filters concurrently. Therefore, various combinations of the aforementioned filters were considered as well.

Table 2.1 summarises the abovestated parameters and their corresponding value ranges. Additionally, Table 2.2 was compiled to maintain an overview of the different parameter combinations that ought to be considered in the SA. It should be noted that Case 1 (C1) in Table 2.2 represents the baseline parameter-setting; the baseline acts as a reference in this case.

Table 2.1: Overview key image (pre-)processing parameters and values (or methods) adopted for the sensitivity analysis.

Parameter	Unit	Abbreviation	Adopted values / methods
Sampling frequency	Hz	SF	60, 30, 10, 5, 2
Image resolution	px	IR	1280x720, 1920x1080, 2560x1440, 3840x2160
Interrogation area size	px	IA	320, 256, 128, 64, 32, 16
Searching area size	px	SS	160, 128, 64, 32, 16, 8
Image enhancement technique	-	IE	CLAHE, High-pass filter, Intensity capping, Wiener2 denoise and low-pass

Table 2.2: Implementation of the sensitivity analysis with reference to image (pre-)processing; each case (C1, C2, …) represents a unique combination of parameter values considered in the LSPIV analysis. See Table 2.1 for an explanation of the abbreviations and units.

	SF					IR				IA						SS						IE			
Case	**60**	**30**	**10**	**5**	**2**	**3840**	**2560**	**1080**	**720**	**320**	**256**	**128**	**64**	**32**	**16**	**160**	**128**	**64**	**32**	**16**	**8**	**CLAHE**	**High-pass filter**	**Intensity capping**	**Wiener2 denoise**
C1 (base)			x				x						x						x			x			
C2	x						x						x						x			x			
C3		x					x						x						x			x			
C4				x			x						x						x			x			
C5					x		x						x						x			x			
C6			x						x				x						x			x			
C7			x					x					x						x			x			
C8			x			x							x						x			x			
C9			x				x			x						x						x			
C10			x				x				x						x					x			
C11			x				x					x						x				x			
C12			x				x							x						x		x			
C13			x				x								x						x	x			
C14			x				x						x						x				x		
C15			x				x						x						x			x	x		
C16			x				x						x						x					x	
C17			x				x						x						x			x		x	
C18			x				x						x						x						x
C19			x				x						x						x			x			x
C20			x				x						x						x				x	x	
C21			x				x						x						x				x		x
C22			x				x						x						x					x	x
C23			x				x						x						x			x	x	x	x
C24			x				x						x						x						

2.5. Study Areas

The LSPIV implementations presented in this thesis involved data acquisition campaigns at two different study areas. More specifically, experimental measurements were performed at the Dinkel River and Meuse River in the Netherlands. The two study areas considered differ from each other with respect to mainly the following aspects: flow conditions, seeding conditions, scale, and accessibility. The collection of field data in these different environments enabled thorough testing of the LSPIV process. A description of the study areas is presented in the following subsections.

2.5.1. Dinkel River

Surface water flow observations were carried out at various sections along the Dinkel River. The transboundary Dinkel River originates in the state of North Rhine-Westphalia in Western Germany. The main stream of the Dinkel River flows from south to north; with its source in the vicinity of Rosendahl (Germany), the river flows towards Gronau, crosses the Germany-Netherlands border into the Dutch province of Overijssel at Glane, then proceeds to flow to Denekamp, and finally re-enters Germany where it merges with the Vecht River near Neuenhaus (Figure 2.10). The main stream of the Dinkel River extends for approximately 93 km, of which 46 km runs through the Netherlands. The total area of the catchment basin is roughly 650 km^2 (Kabo-bah, 2010). The average channel width is approximately 10 to 20 m (Yin, 2010). The first data acquisition campaign took place in the Netherlands at a specific reach of the river. Figure 2.10 delineates the study area that was considered. The study area is located near the village of Lattrop-Breklenkamp, close to the Netherlands-Germany border. An important reason for selecting this particular reach is that the site is well-accessible. On top of that, the river banks allow for easy placement of GCPs. Based on past observations, the water surface at this reach is generally covered by naturally occurring features. As can be seen in Figure 2.11a, a small hydraulic structure is located directly upstream of the selected reach. The flow of water through the weir gives rise to turbulence patterns along with the generation of foam and air bubbles on the water surface. With this in mind, the selected study area fits the focus of this study.

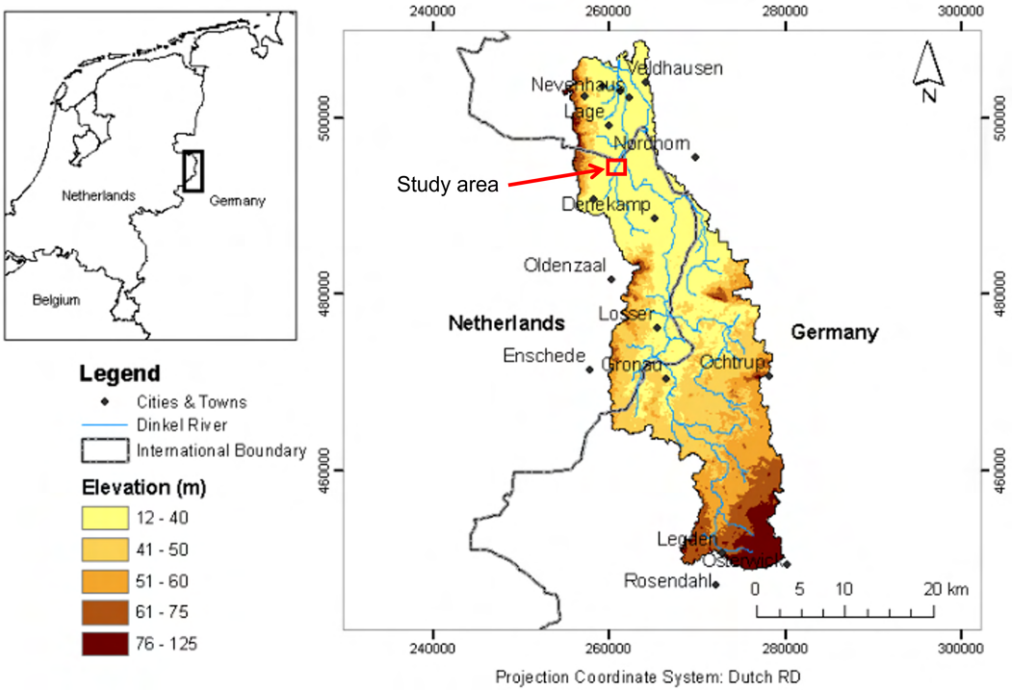

Figure 2.10: Map showing the Dinkel river catchment, the study area is outlined in red. Source: Kabo-bah (2010)

Figure 2.11b shows an aerial view of the locations where the first data acquisition campaign was carried out. As can be seen in this figure, experimental observations were performed at three different sections downstream of the hydraulic structure as shown in Figure 2.11a. The first section (location 1) is located

directly downstream of the hydraulic structure; features on the water surface tend to be omnipresent at this location. The second section (location 2) is located further downstream at a distance of approximately 75 m from the structure. Foam and air bubbles can still be observed on the water surface at this section, albeit in lower quantities. Nevertheless, the surface features remain highly visible and cover virtually the entire water surface. Finally, experimental observations were also conducted roughly 150 m downstream of the structure (location 3). The seeding conditions at location 3 were found to differ greatly from those at the other sections. To illustrate this, the average particle size was observed to be significantly smaller; this causes strong deterioration of the tracer visibility. Interestingly enough, the features seem to be distributed more homogeneously as compared to the other sections. The different seeding conditions at the aforementioned sections allow for more rigorous testing of LSPIV implementations in this study (Tauro et al., 2016a; Weitbrecht et al., 2002).

Figure 2.11: Dinkel River study area (52°25'23.8"N 6°57'35.3"E): (a) photograph of the hydraulic structure upstream of the selected measurement locations; (b) aerial view of the study area, the solid boxes outline the locations along the reach where the surface water flow was observed. Source: Google Earth

2.5.2. Meuse River at Sambeek

The second study area considered in this thesis is located in the Meuse River near the village of Sambeek, the Netherlands. The Meuse is a major European transboundary river flowing through France, Belgium and the Netherlands, with its originating source being in the French region of Grand Est. Flowing from France and Belgium, the Meuse crosses the Belgium-Netherlands border at Eijsden (the Netherlands); the river then continues to flow through the Netherlands until it drains into the North Sea via the Rhine–Meuse–Scheldt delta (De Oliveira et al., 2020). The main course of the Meuse River has a total length of approximately 950 km, of which 250 km extends through the Netherlands (De Oliveira et al., 2020). The total area of the river catchment is roughly 34,548 km^2 and the average channel width of the river is approximately 100 m (Breukel et al., 1992). Figure 2.12 outlines the study area that was considered; an important reason for selecting this particular reach is the presence of a lock-weir complex therein. Within the lock-weir complex, there exists a variety of hydraulic structures, including a weir, two navigation locks, and a fish passage. With this in mind, the site in question is considered highly suitable for the purpose of this study, as this study focuses attention on flows near hydraulic structures. Moreover, the weir-lock complex at Sambeek is easily accessible from a logistics point of view, which is yet another important reason for selecting this study site. The property owner, Rijkswaterstaat (Dutch Directorate-General for Public Works and Water Management), was informed about the measurement activities and has formally granted an exemption to fly the drone on the premises of the lock-weir complex.

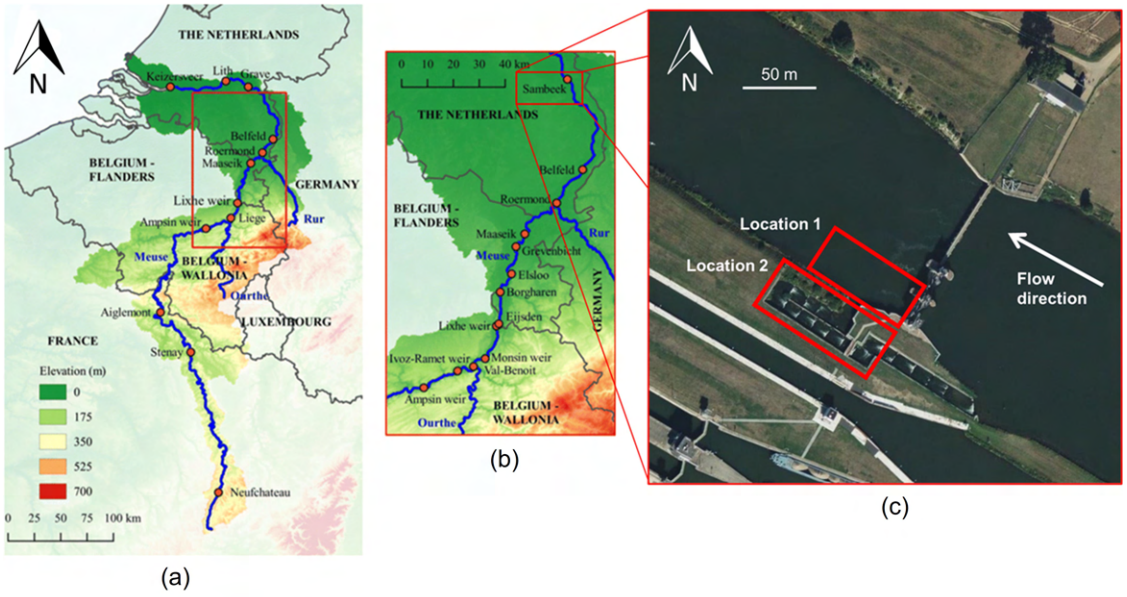

Figure 2.12: Map showing the Meuse River study area: (a) and (b) Meuse River catchment, topography and main weirs along the river; (c) delineation of the study area at Sambeek, the Netherlands (51°38'26.5"N 5°59'06.3"E). Sources: Kitsikoudis et al. (2020); Google Earth

The study area covers two sections at which experimental observations were carried out (Figure 2.12c). The first section (location 1) is located directly downstream of the weir (Figure 2.13); this weir is commonly referred to as Weir Sambeek and is part of a cascade of seven weirs along the Dutch part of the Meuse. Weir Sambeek makes part of a large lock-weir complex and is essentially made up of two structures: a so-called Poirée weir (left part of weir in Figure 2.13) and a Stoney weir (right part of weir in Figure 2.13). The Poirée weir consists of 13 openings which are collectively 63.0 m wide (Rijkswaterstaat, 2014a). The Stoney weir, on the other hand, consists of two gates, each exactly 17.0 m wide (Rijkswaterstaat, 2014b). In this study, the focus will be mainly on the flow near the Stoney weir. Directly next to the weir, a fish passage was constructed to allow for the upstream and downstream migration of aquatic animals (Kranenbarg & Kemper, 2006); the structure in question is made up of a series of descending pools, and is roughly 250 m long and 10 m wide. As can be seen in Figure 2.13, the rushing water through the passage gives rise to turbulence patterns along with the generation of foam on the water surface. With this in mind, the characteristics of the flow within the fish passage fit the purpose of this study as well. Therefore, this study will also conduct experimental measurements at the fish passage to assess whether LSPIV is also well-able to characterise the flow in such settings.

Figure 2.13: Bird's-eye view of the measurement locations as delineated in Figure 2.12c. The left hand side of the figure shows the weir (location 1) and the right hand side shows the fish passage (location 2). Source: *www.binnenvaartinbeeld.com*

2.6. Experimental setups

2.6.1. Remotely sensed data at the Dinkel River

The first data acquisition campaign took place at the Dinkel River on 11 April 2022. Video recordings of the flowing water were collected at three sections along the selected river reach (Figure 2.11b); this was done with the use of the commercially available DJI Phantom 4 Pro drone (Figure 2.14a). The DJI Phantom 4 Pro is a lightweight (1.4 kg) and relatively inexpensive (approximately EUR 1,500) quadcopter drone with a built-in camera system. The flight time of the drone on a full battery charge is approximately 30 minutes and the maximum wind speed that it is able to resist is 10 m/s. The maximum video resolution of the camera system is 3840x2160 px at a sampling frequency up to 60 Hz. The camera system is also equipped with a three-axis gimbal to eliminate part of the residual movements of the drone caused by wind effects and unstable hovering. Next to drone-borne imagery, video recordings were collected using a stationary camera as well (Figure 2.14b); this was to facilitate the comparison between drone-based and fixed camera LSPIV (section 3.3). The stationary camera setup comprised a handheld camcorder mounted on a tripod stand; the camera in question is able to record videos with a maximum resolution of 1920x1080 px and sampling frequency of 30 Hz. Lastly, five GCPs were placed on the river bank at each side of the river at both locations 2 and 3. It is worth noting that no GCPs were placed at location 1, as there were no plans for collecting imagery with tilted camera angles at this location; this means that the flow at location 1 was recorded with a nadir camera orientation exclusively. For an impression of the field campaign, the reader is referred to Appendix A.

(a) (b)

Figure 2.14: Experimental setup Dinkel River: (a) DJI Phantom 4 Pro drone; (b) stationary camera setup.

At the time of the data acquisition campaign, the average wind speed measured at the nearest weather station was 2.5 m/s at a height of 10 m (KNMI, 2022). Unfortunately, hydraulic data sets for the Dinkel River, such as data sets containing discharge and water level measurements, are not available for that period. Notwithstanding, it can be stated that moderate to high flow conditions were observed; this is assumed to be true as large patches of emergent vegetation are generally visible during low flow conditions in the study area (Appendix A: Figure A.4), which was not the case during this campaign. That being said, a multitude of video recordings were collected. At each of the three sections, the flow was captured at an altitude of 40 m at nadir (tilt angle of 0°) using the drone. With an eye towards the SA, different drone flight altitudes were considered as well at each section. On top of that, different camera tilt angles were considered at locations 2 and 3. Recordings with the stationary camera, on the other hand, were limited to one video recording for location 2 as well as location 3, as no SA will be performed using ground-based imagery. The stationary camera was positioned on the river bank and had an oblique view towards the water surface (Figure 2.14b). Table 2.3 shows an overview of all different experimental configurations that were adopted.

Table 2.3: Overview of video recordings collected at the Dinkel River study area and corresponding details.

Location	Camera height w.r.t. water surface [m]	Camera tilt angle [°]	Recording duration [s]	Spatial resolution [px]	Sampling frequency [Hz]
		Drone			
1	40	0	60	3840x2160	60
1	56	0	60	3840x2160	60
2	40	0	60	3840x2160	60
2	40	45	60	3840x2160	60
2	56	0	60	3840x2160	60
2	15	70	60	3840x2160	60
3	40	0	60	3840x2160	60
3	40	45	60	3840x2160	60
3	56	0	60	3840x2160	60
3	15	70	60	3840x2160	60
		Stationary camera			
2	$\sim$5	80	1435	1920x1080	30
3	$\sim$2.5	80	1047	1920x1080	30

2.6.2. Remotely sensed data at the Meuse River at Sambeek

The second data acquisition campaign took place on 03 June 2022 at the weir-lock complex located in the vicinity of the village of Sambeek, the Netherlands. Video recordings of the flowing water were collected by hovering a drone above a section of the weir (location 1) and the fish ladder (location 2). The same drone was employed as the one used in the Dinkel River study area. An overview of the video recordings collected at the Sambeek study area can be found in Table 2.4. It is important to realise that the camera system of the drone failed to record at the highest possible resolution of 3840x2160 px. Instead, the resolution was set at 1280x720 px. Furthermore, the sampling frequency was set at 30 Hz instead of 60 Hz. It is also important to mention that the river banks of the Meuse at the lock-weir complex were inaccessible, meaning that GCPs could not be placed; this, in turn, means that video recordings could not be collected at different camera tilt angles, as orthorectification could not be performed without GCPs. With this in mind, a comprehensive SA could not be performed using the imagery collected at the Meuse River. Consequently, only different drone flight altitudes were considered for the purpose of the SA, namely altitudes of 56 and 70 m for both locations 1 and 2. It was not possible to consider lower flight altitudes due to the aggressive and territorial behaviour of birds trying to enforce their exclusive use of the air space. Finally, fixed camera LSPIV was also disregarded in this case, since the study area did not allow for the collection of imagery using a stationary camera setup.

Table 2.4: Overview of video recordings collected at the Meuse River at Sambeek and corresponding details

Location	Height w.r.t water surface [m]	Camera tilt angle [°]	Recording duration [s]	Spatial resolution [px]	Sampling frequency [Hz]
1	56	0	120	1280x720	30
1	70	0	120	1280x720	30
2	56	0	120	1280x720	30
2	70	0	120	1280x720	30

At the time of the data acquisition campaign (10:00 to 13:00), the average discharge rate measured in the Meuse River upstream the study area was 31 m^3/s, which is considered to be exceptionally low (Rijkswaterstaat, 2022). Because of the low discharge rate, only the two southernmost gates of the weir (i.e., Stoney gates) were opened at the time. Furthermore, the average water levels measured directly upstream and downstream the weir were 11.2 and 7.8 m+NAP respectively (Rijkswaterstaat, 2022). The average daily wind speed measured at a height of 10 m at a nearby weather station was 4 m/s (KNMI, 2022).

3
Results

3.1. Dinkel River

3.1.1. Data acquisition campaign

Figures 3.1, 3.2 and 3.3 show snapshots taken by the drone at locations 1, 2 and 3, respectively. The area encompassed by the water surface in these figures delineates the ROI that was considered in the LSPIV analyses. The aforementioned figures show that the water surface at each of the three locations is relatively well-coated with foam and air bubbles at the time of the measurement campaign. Directly downstream of the weir at location 1, intense momentum exchange (mixing) of the flow can be observed in the video recordings. Because of the turbulent processes occurring in the mixing layer, the flow patterns were highly irregular directly downstream of the weir. Continuous clustering and disintegration of the surface features were taking place, which makes it quite challenging to recognise distinct patterns at this location. As one moves further downstream at location 1, the flow appears to decelerate and the surface features tend to attain a more permanent and distinctive shape. Regarding the flow seeding characteristics at location 1, there exists a large disparity in tracer diameters and the tracer material seems to be distributed quite heterogeneously. As one moves to locations 2 and 3 at a distance of respectively 75 m and 150 m downstream of the weir, the flow conditions appear to be much more uniform. Moreover, the surface features seem to have been disintegrated considerably as they travelled downstream, this is especially true for location 3. Nevertheless, surface features were still abundant on the water surface at these locations. Interestingly, at locations 2 and 3, the tracer material appears to be scattered more homogeneously across the water surface than at location 1. Finally, the disparity in tracer diameters was less prominent at the two downstream locations.

To quantitatively analyse the flow seeding characteristics within the ROIs, particle analysis was applied using the image analysis software ‘ImageJ’ (Schneider et al., 2012). Using this software, it was found that for location 1, the average seeding density in each frame of the image sequence is roughly 10% (Table 3.1); meaning that more or less 10% of the water surface within the ROI of location 1 was covered by foam and air bubbles. Furthermore, the fact that there is a particularly large spread in the observed diameters of the surface features at location 1 is corroborated by Figure 3.4 and Table 3.1. The mean tracer diameters at locations 1, 2 and 3 are estimated to be roughly 12 cm, 9 cm and 8 cm, respectively. Finally, even though tracer characteristics changed significantly downstream, the seeding density was preserved and maintained a value of around 10%.

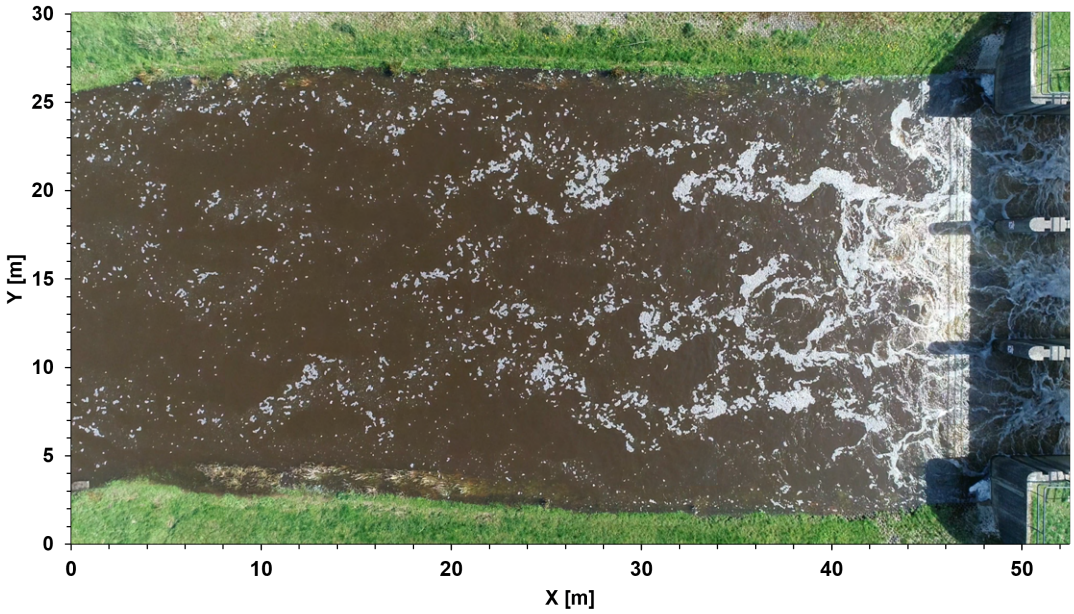

Figure 3.1: Snapshot of location 1 at Dinkel River representing the ROI considered in the LSPIV analysis. Image was captured on 11 April 2022 by a drone at a flight altitude of 40 m and camera tilt angle of 0°.

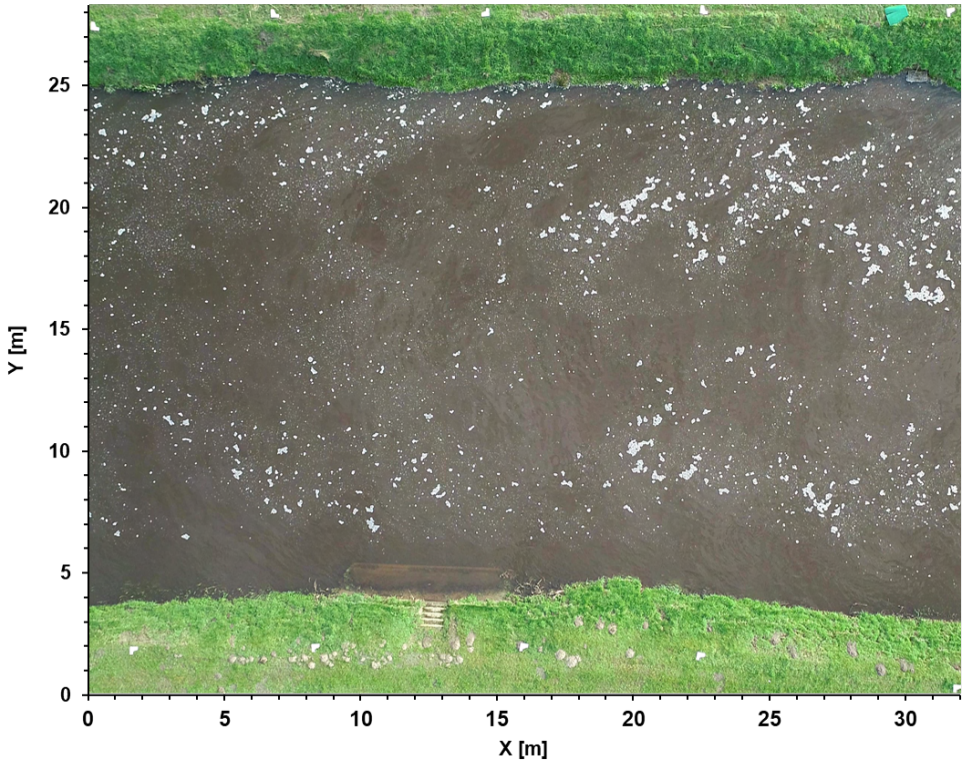

Figure 3.2: Snapshot of location 2 at Dinkel River representing the ROI considered in the LSPIV analysis. Image was captured on 11 April 2022 by a drone at a flight altitude of 40 m and camera tilt angle of 0°.

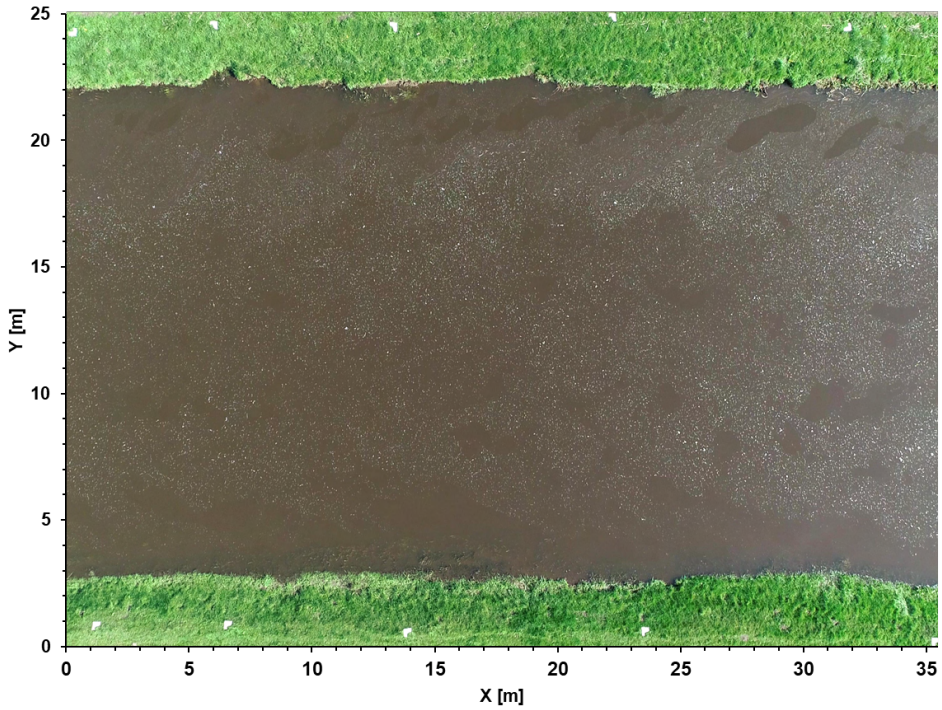

Figure 3.3: Snapshot of location 3 at Dinkel River representing the ROI considered in the LSPIV analysis. Image was captured on 11 April 2022 by a drone at a flight altitude of 40 m and camera tilt angle of 0°.

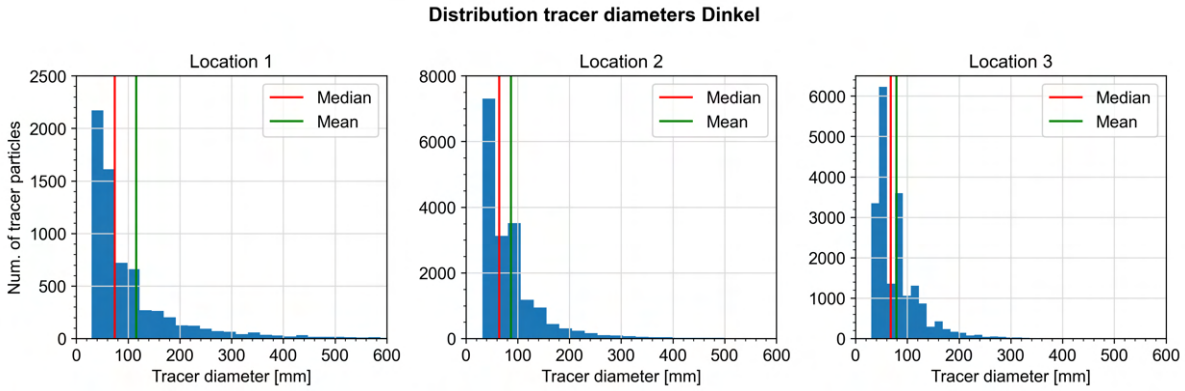

Figure 3.4: Distributions of tracer diameters at the three locations along the Dinkel River

Table 3.1: Summary seeding characteristics at each of the three locations along the Dinkel river

Location	Seeding density [%]	Mean diameter [mm]	Mean diameter [px]	Median diameter [mm]	Median diameter [px]	Std diameter [mm]
1	9.7	116	5.6	75	3.6	169
2	11.3	87	3.8	64	2.8	83
3	10.6	79	3.7	68	3.2	56

3.1.2. LSPIV analysis

Location 1

Following the steps of the LSPIV workflow, vector fields representing the surface water flow velocities were generated using the drone-borne imagery collected at the Dinkel River study area. Figure 3.5 visualises the velocity field at location 1 averaged over a time period of 60 s. The velocity field was computed using the parameter settings specified in Table 3.2. The default resolution of the collected imagery (3840x2160 px) was resampled to a slightly lower resolution to reduce the computational cost of the image pre-processing and LSPIV analysis. Furthermore, a sampling frequency of 10 Hz was selected based on findings in the literature (e.g., Liu et al. 2021; Legleiter & Kinzel 2020; Perks et al. 2019). The reader is referred to Appendix B for an impression of the sequence of steps undertaken to obtain the velocity field presented in this section.

Table 3.2: Default parameter settings used in the drone-based LSPIV implementation of location 1 at the Dinkel River.

Flight altitude [m]	Camera tilt angle [°]	Image resolution [px]	Sampling frequency [Hz]	Interrogation area size [px]	Pixel size [m]	Vector spacing [m]	Image enhancement technique(s)
40	0	2560x1440	10	64	0.0207	0.0662	CLAHE

The time-averaged LSPIV output in Figure 3.5 shows a coherent vector field and velocity magnitudes that seemingly align with the expectations. The video recordings showed that the flow directly downstream of the hydraulic structure was particularly unsteady and quite turbulent. Accordingly, the LSPIV results show the greatest velocity magnitudes here, with the inflow from the centre opening of the weir exhibiting the greatest surface flow velocities (Figure 3.6). Interestingly, when moving downstream, the velocity magnitude decreases before it increases again (between X = 20 m and X = 40 m); this phenomenon might be related to the development of a new boundary layer and the transition of the flow into the relaxation zone, where the velocity attains a normal logarithmic profile again (Ali, 2013; Robert, 2003). It is also likely that the phenomenon in question is due to lateral mixing occurring between the faster moving flow in the middle and slower moving flow at the sides of the channel, causing deceleration of the faster moving flow (Robert, 2003). The gradual increase of the flow velocity further downstream may then be caused by, for example, the narrowing of the channel. Another possible explanation for the phenomenon in question is the presence of a scour hole causing an expansion of the flow; this flow expansion, in turn, may cause a local reduction of the flow velocities (Guan et al., 2014). Lastly, the presence of large vegetation patches in the river (see Appendix A, Figure A.4) may also be a reason for the observed local flow velocity reduction. However, it is important to mention that there is limited experimental evidence to support any of the aforementioned claims.

The velocity profile along transect B in Figures 3.5 and 3.6 shows alternating zones of high and low velocity magnitudes; despite the limited experimental evidence, it is presumed that this phenomenon is related to the interaction between the streams exiting from the openings of the weir. To illustrate this, the flow geometry at location 1 contains three inflowing parallel streams that experience a lateral velocity difference amongst themselves. At the confluence of these streams, significant transverse shear is believed to occur, causing the development of two-dimensional flow structures extending over several meters in the downstream direction. Such streamwise horizontal structures at the confluence of two streams are often referred to as shallow mixing layers (Talstra, 2011; Van Prooijen, 2004). The above-mentioned process is illustrated in Figure 3.7a through a simplified schematisation adapted from Talstra (2011). Large-scale turbulent structures can be witnessed within the developing mixing layers, which are bounded by the dashed lines in Figure 3.7a. With increasing streamwise distance, lateral shear experienced among the inflowing streams tends to decrease as an exchange of momentum occurs from the high-velocity side towards the low-velocity side; this causes the horizontal structures to dissipate further downstream (Talstra, 2011). An example of the geometry of a two-dimensional shallow mixing layer is visualised on a laboratory scale in Figure 3.7b; the low-velocity trails as observed in the LSPIV output (Figure 3.5) show some resemblance to this and, therefore, possibly indicate the development of shallow mixing layers at location 1 at the time of the measurement campaign. Based on the findings

in this section, it can be argued that LSPIV offers a promising method for capturing the spatial and temporal structure of fluid motions in large-scale fluvial flows.

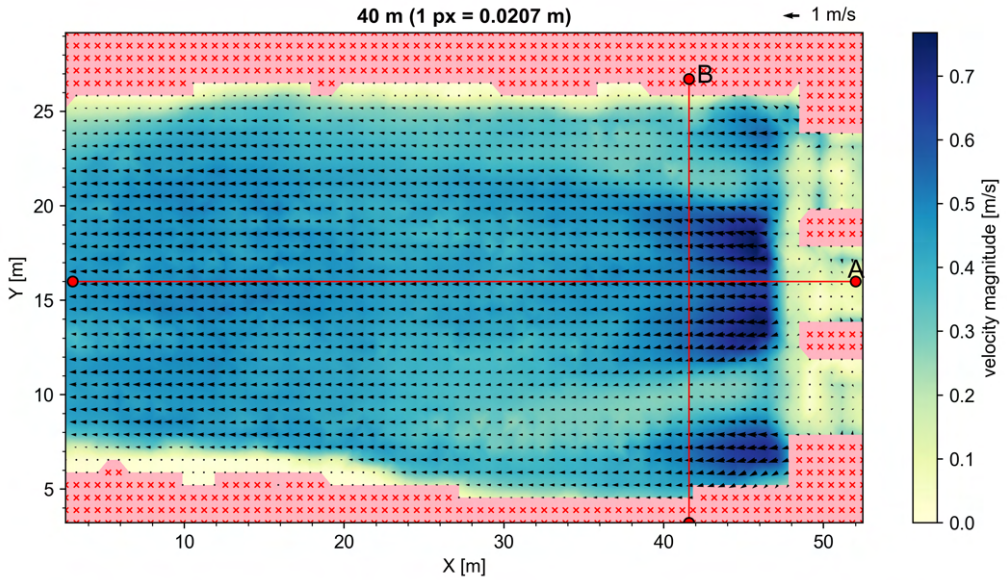

Figure 3.5: Time-averaged surface water flow velocity field for imagery acquired from a drone at location 1 in the Dinkel River study area. Experimental configurations and PIV parameter settings used for the computation are specified in Table 3.2. Red cross marks indicate the presence of static features in the FoV (e.g., weir, river banks, etc.). Red solid lines with red dots at the endpoints represent transects from which velocity profiles are extracted (Figure 3.6).

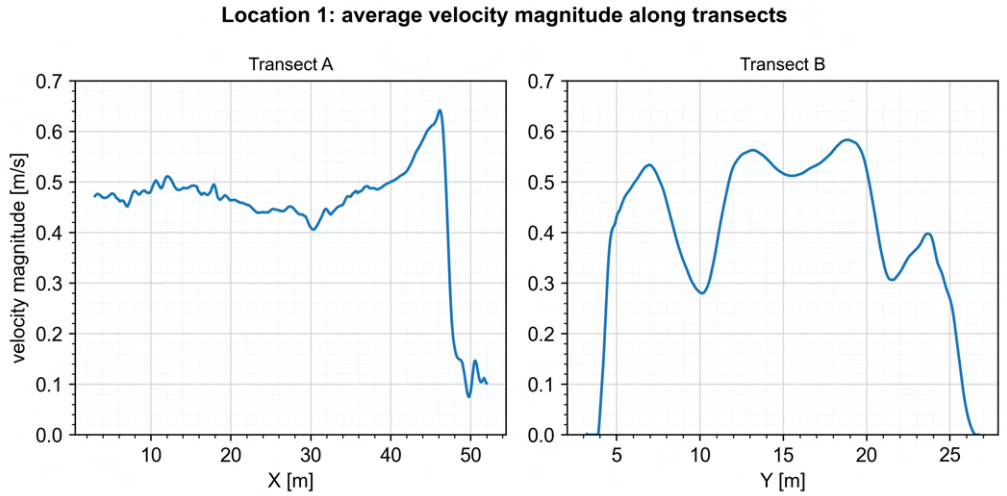

Figure 3.6: Velocity profiles extracted from the transects defined in Figure 3.5.

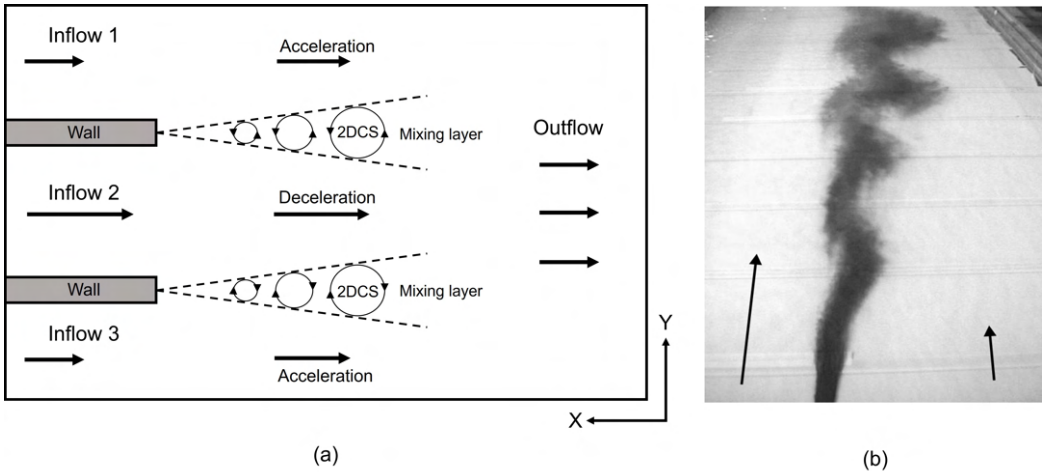

Figure 3.7: (a) Top view schematisation of suspected shallow flow geometry at location 1 of the Dinkel River, dashed lines represent boundaries of the mixing layer. Within the mixing layer, two-dimensional coherent structures (2DCS) are to be found; (b) two-dimensional shallow mixing layer visualised by dye injection at the confluence of two streams with different velocity magnitudes. Figures partially adapted from Talstra (2011) and Van Prooijen (2004).

Location 2

Figures 3.8 and 3.9 show the time-averaged velocity map and corresponding velocity profiles along the transects for location 2. The parameter settings and experimental configurations specified in Table 3.2 were considered again. Yet again, the drone-based, LSPIV-derived velocity field appears to be well able to characterise the flow in the channel qualitatively; this is assumed to be true as the centre of the channel is experiencing the greatest surface water flow velocities. Moreover, it is expected that the flow is encountering more resistance around the perimeter of the channel, causing a reduction of the velocity. In conformity with expectation, lower velocity magnitudes are to be observed at the river banks; interestingly enough, the surface flow velocity magnitudes were found to be slightly greater along the edge of the northern river bank. This may be related to the fact that the river channel is slightly curved (Figure 2.11b). According to Robert (2003), an important feature of curved rivers is the outward transfer of flow momentum, accompanied by a gradual shift of the high-velocity zone towards the outer bend. However, the aforementioned phenomenon may also be due to error sources, such as image instabilities, causing an unintentional shift of the velocity field despite the efforts of the image stabilisation software.

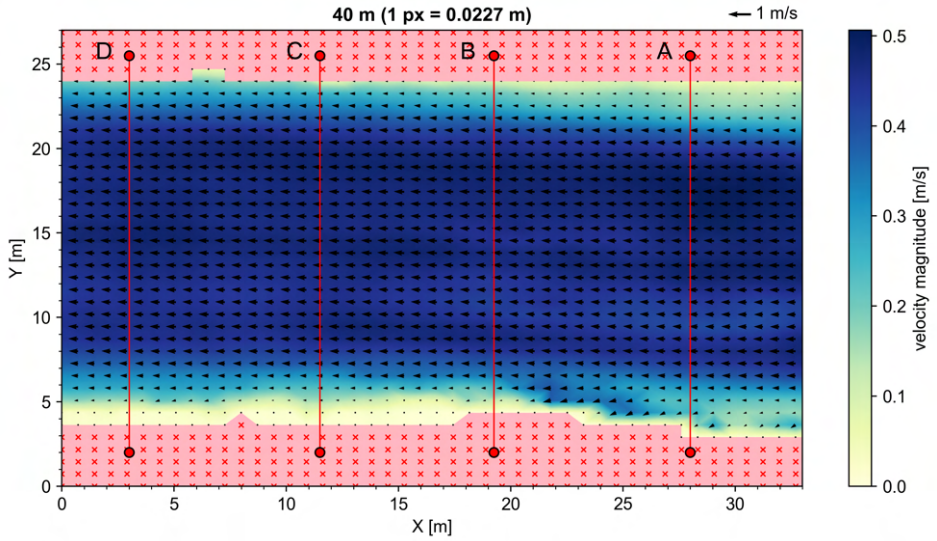

Figure 3.8: Time-averaged surface water flow velocity field for imagery acquired from a drone at location 2 in the Dinkel River study area. Experimental configurations and PIV parameter settings used for the computation are specified in Table 3.2.

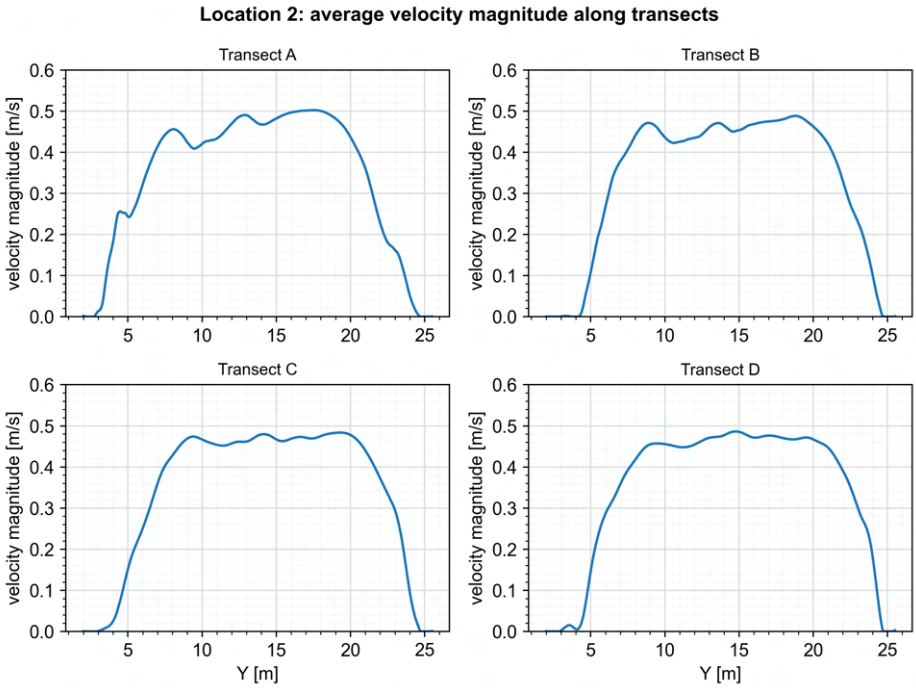

Figure 3.9: Velocity profiles extracted from the transects defined in Figure 3.8.

Location 3

The LSPIV-derived velocity field of location 3, which is visualised in Figure 3.10, is quite similar to the velocity field of location 2 (Figure 3.8). Once again, the centre of the river channel experiences the greatest surface water flow velocities, while the flow at the edges of the channel tends to decelerate. This shows that, even with considerable disintegration of the tracer material, LSPIV can generate a coherent vector field consistent with the results of the other locations. A final observation worth mentioning is that, when carefully inspecting the velocity field, preferential flow paths with slightly higher velocity magnitudes can be observed within the stream (e.g., along Y = 10 m and Y = 15 m in Figure 3.10); this was observed in Figures 3.8 and 3.9 as well. Such preferential streamlines often develop due to in-stream features, such as submerged vegetation covers; for example, high-velocity trails may appear between vegetation patches due to flow contraction (Cotton et al., 2006).

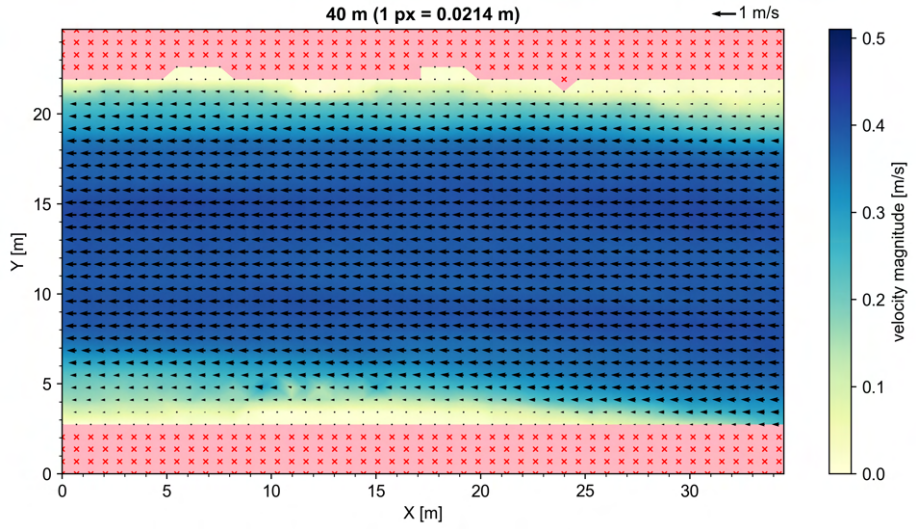

Figure 3.10: Time-averaged surface water flow velocity field for imagery acquired from a drone at location 3 in the Dinkel River study area. Experimental configurations and PIV parameter settings used for the computation are specified in Table 3.2.

3.1.3. Accuracy assessment

An accuracy assessment was carried out to quantitatively assess whether the LSPIV results presented in the previous section (section 3.1.2) agree with the actual surface water flow velocity magnitudes. Reference measurements were collected for each of the three locations using the float method to facilitate the accuracy assessment. Based on this method, a grid of twelve points was established on the ROIs of the locations, with each point representing a reference measurement (e.g., Figure 3.11); the measurement point arrangements of locations 2 and 3 can be found in Appendix B. At each of the 12 measurement points, the mean velocity was determined using ten observations. The collected reference velocities and corresponding details are summarised in Table 3.3; these reference velocities were subsequently used to compute various error metrics. Table 3.4 presents the summary of the error metrics for each location. It was found that the mean absolute velocity deviations of LSPIV are in the order of 10^{-2} m/s. Furthermore, the NRMSE values do not exceed 9% for any of the three locations, while the NMBE values are less than 5%. On top of that, the MBE attained a positive value in each case, indicating a slight tendency to underestimate the velocity magnitudes. Interestingly enough, the downstream locations showed increasingly higher measurement accuracy, implying that the flow seeding conditions are indeed important controls of the LSPIV performance; this may also suggest that the PIV settings considered in the analyses were possibly more appropriate for the seeding conditions at locations 2 and 3. Nonetheless, the error metrics suggest that LSPIV provided quite accurate velocity estimations relative to the reference measurements; this is especially true vis-à-vis the results existing in the literature, as will be addressed in the discussion later in this thesis.

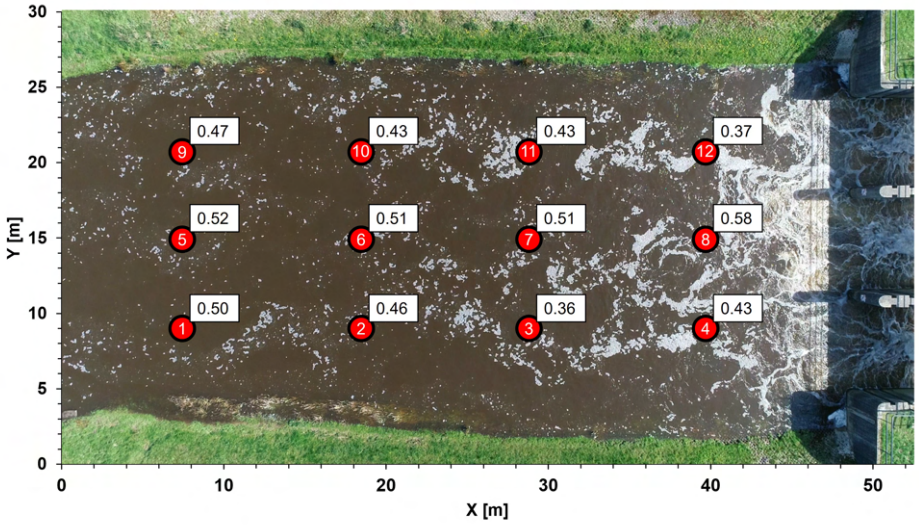

Figure 3.11: Reference measurement points with surface water flow velocity magnitudes (m/s) at location 1 Dinkel River.

Table 3.3: Overview details reference measurements of surface flow velocities (m/s) for the three locations in Dinkel River.

Reference measurement	Num. of replications	Location 1				Location 2				Location 3			
		Mean	Min	Max	Std	Mean	Min	Max	Std	Mean	Min	Max	Std
1	10	0.50	0.45	0.54	0.03	0.44	0.39	0.50	0.03	0.35	0.31	0.40	0.03
2	10	0.46	0.40	0.50	0.03	0.47	0.38	0.56	0.05	0.39	0.35	0.42	0.02
3	10	0.36	0.29	0.45	0.05	0.46	0.37	0.50	0.04	0.38	0.36	0.42	0.02
4	10	0.43	0.32	0.59	0.07	0.44	0.38	0.53	0.05	0.39	0.36	0.43	0.02
5	10	0.52	0.49	0.54	0.02	0.49	0.43	0.56	0.04	0.41	0.40	0.50	0.03
6	10	0.51	0.46	0.55	0.04	0.53	0.42	0.52	0.03	0.40	0.38	0.42	0.01
7	10	0.51	0.43	0.67	0.08	0.46	0.47	0.59	0.04	0.42	0.38	0.46	0.03
8	10	0.58	0.48	0.91	0.13	0.49	0.43	0.56	0.03	0.43	0.38	0.47	0.03
9	10	0.47	0.44	0.51	0.02	0.43	0.43	0.49	0.03	0.38	0.33	0.40	0.02
10	10	0.43	0.37	0.48	0.04	0.51	0.44	0.52	0.02	0.39	0.36	0.42	0.02
11	10	0.43	0.35	0.49	0.05	0.47	0.43	0.56	0.03	0.40	0.38	0.42	0.01
12	10	0.37	0.28	0.50	0.08	0.46	0.37	0.48	0.04	0.41	0.38	0.43	0.02

Table 3.4: Summary of error metrics for LSPIV results presented in section 3.1.2. RMSE = root mean squared error; MBE = mean bias error; RMSE and MBE were normalised by the mean velocity magnitude obtained from the float method (0.47, 0.39 and 0.40 m/s for locations 1, 2 and 3 respectively)

Location	Pixel size [m]	Vector spacing [m]	RMSE [m/s]	MBE [m/s]	NRMSE [%]	NMBE [%]
1	0.0207	0.662	0.041	0.023	8.8	4.9
2	0.0227	0.726	0.028	0.002	6.1	0.5
3	0.0214	0.685	0.020	0.015	5.0	3.9

3.1.4. Sensitivity to experimental configurations

Camera tilt angle

In this subsection, the effects of the camera tilt angle on the LSPIV performance were examined. Concurrently, different orthorectification procedures, that is explicit and implicit orthorectification, were tested. It should be noted that location 1 was disregarded in this analysis due to time constraints. Firstly, the water surface of locations 2 and 3 was recorded in streamwise direction considering a tilt angle of 45° at a flight altitude of 40 m. For the second configuration, a tilt angle of 70° and flight altitude of 15 m was considered; in this case, the drone had to be moved closer to the water surface to be able to capture all GCPs within the ROI. The resulting time-averaged velocity maps are illustrated in Figures 3.12 and 3.14 for locations 2 and 3, respectively. Additionally, one can find the respective velocity profiles in Figures 3.13 and 3.15. The LSPIV-derived velocity fields of the different experimental configurations were found to differ from each other quite considerably. To illustrate this, the velocity fields corresponding to the first configuration (40 m & 45°) are qualitatively in relatively good agreement with the baseline configuration (40 m & 0°), while the velocity fields of the second configuration (15 m & 70°) tend to show erratic behaviour; in the case of location 2, seemingly indecipherable smudges of high-velocity magnitude values are present in the velocity fields (Figure 3.12). It remains unclear what caused these high-velocity smudges; nonetheless, it is believed that this erratic behaviour is attributed to the non-uniformity of the water surface luminosity. More specifically, local illumination non-uniformity caused by glare and sun glitter could be observed on the water surface, possibly due to the significant tilt of the camera angle. The illumination non-uniformity, in turn, may have affected the visibility of the surface features. Furthermore, depending on the adopted orthorectification procedure, one may obtain a very sparse or dense vector field. It is important to realise that orthorectification of imagery prior to the velocity field computation is accompanied by significant deterioration of the image resolution and will, therefore, lead to a sparser vector field. With implicit orthorectification, on the other hand, one is able to retain the native resolution of the imagery as no additional image manipulation is required prior to the application of the PIV algorithm. Lastly, the velocity estimations are inconsistent along the channel; this is especially true in the case of location 3. Figures 3.14 and 3.15 show that the velocity magnitude tends to be underestimated or overestimated considerably as one moves downstream location 3. This phenomenon is attributed to the fact that distortions resulting from the orthorectification process are most prominent in the far field of the image (Hauet et al., 2008a); these distortions may have caused strong deterioration of the tracer visibility. However, it was found that this effect is less noticeable with implicit orthorectification.

For each experimental configuration, various error metrics were calculated (Table 3.5); this was done for both locations 2 and 3. The experimental configurations considered in this SA yielded NRMSE values up to 15% and 45% for locations 2 and 3, respectively. Similarly, the NMBE jumps up to 11% and 42% for locations 2 and 3, respectively. These results demonstrate that the camera tilt angle is indeed a key parameter in LSPIV. The greatest errors were found to correspond to the image sequences that were orthorectified explicitly. Moreover, the experimental configuration comprising the largest tilt angle (70°) also showed particularly poor results. With this in mind, the results presented in this section convincingly demonstrate that error may be minimised by keeping the camera tilt angle as small as possible (preferably at nadir). If it is not possible to record at nadir, one should keep in mind that the LSPIV analysis will be less accurate due to fact that distortions will be introduced onto the imagery as a result of the orthorectification process; error associated with image transformations, however, can be

kept to a minimum by performing orthorectification implicitly rather than explicitly.

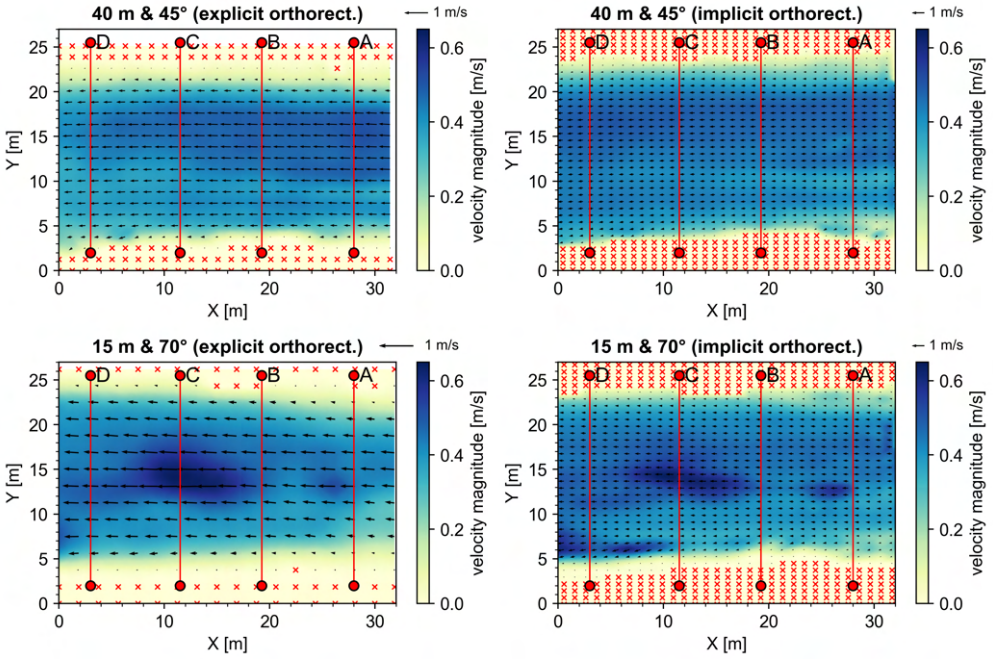

Figure 3.12: Visual comparison of time-averaged surface water flow velocity fields computed with different camera tilt angles and orthorectification procedures. Imagery was acquired from a drone at location 2 in the Dinkel River study area.

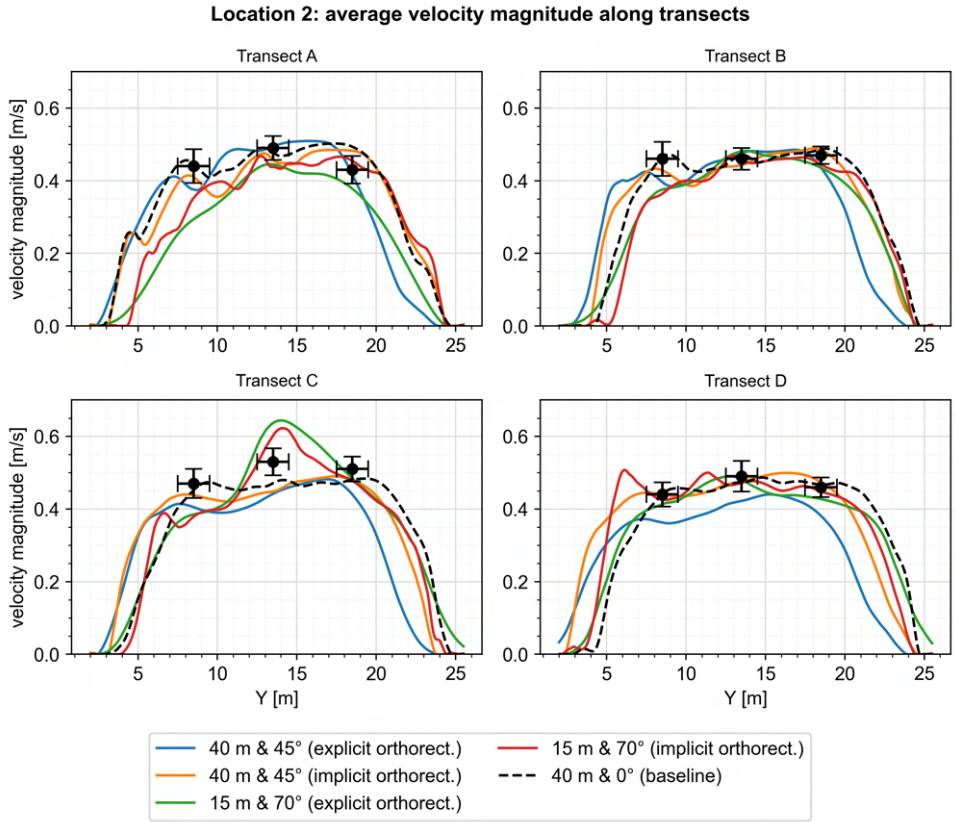

Figure 3.13: Velocity profiles extracted from the transects defined in Figure 3.12 for different camera tilt angles and orthorectification procedures. Markers represent mean surface water velocity magnitudes obtained from the float method. Uncertainty intervals surrounding the markers represent the standard deviation.

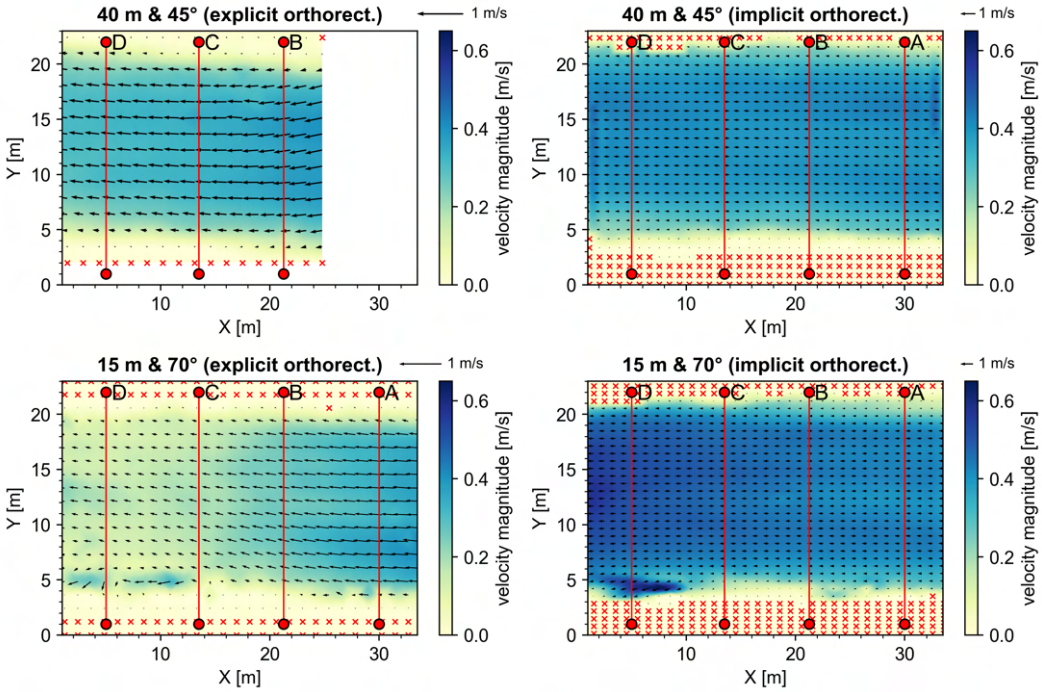

Figure 3.14: Visual comparison of time-averaged surface water flow velocity fields computed with different camera tilt angles and orthorectification procedures. Imagery was acquired from a drone at location 3 in the Dinkel River study area. Note that in the top left plot the orthorectification tool was unable to process the entire ROI.

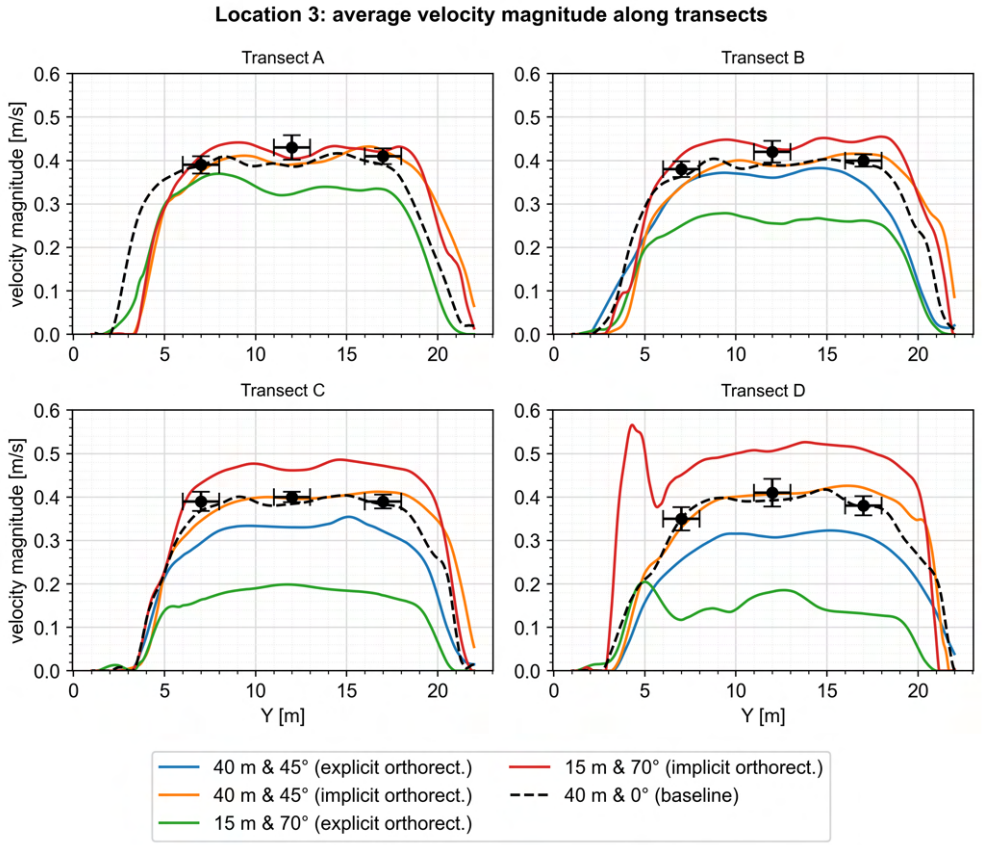

Figure 3.15: Velocity profiles extracted from the transects defined in Figure 3.14 for different camera tilt angles and orthorectification procedures. Markers represent mean surface water velocity magnitudes obtained from the float method. Uncertainty intervals surrounding the markers represent the standard deviation.

Table 3.5: Summary of error metrics for LSPIV results from the Dinkel River for different camera tilt angles and orthorectification procedures. RMSE = root mean squared error; MBE = mean bias error; RMSE and MBE were normalised by the mean velocity magnitude obtained from the float method (0.39 and 0.40 m/s for locations 2 and 3 respectively)

Explicit/ implicit rect.	Flight altitude [m]	Camera tilt angle [°]	Inter. area [px]	Step size [px]	Vector spacing [m]	RMSE [m/s]	MBE [m/s]	NRMSE [%]	NMBE [%]
Location 2									
N/A	40	0	64	32	0.726	0.028	0.002	6.03	0.449
Explicit	40	45	64	32	1.257	0.060	0.050	12.78	10.68
Implicit	40	45	64	32	0.963	0.036	0.016	7.57	3.33
Explicit	15	70	64	32	1.873	0.068	0.035	14.51	7.35
Implicit	15	70	64	32	1.038	0.055	0.028	11.66	6.03
Location 3									
N/A	40	0	64	32	0.685	0.020	0.015	4.97	3.91
Explicit	40	45	64	32	1.458	0.075	0.073	19.25	18.56
Implicit	40	45	64	32	0.915	0.028	0.009	7.14	2.30
Explicit	15	70	64	32	1.210	0.180	0.167	45.41	42.11
Implicit	15	70	64	32	1.001	0.066	-0.050	16.78	-12.68

Drone flight altitude

This subsection examined the effects of the GSD on the LSPIV performance. The GSD was varied by collecting imagery at two different drone flight altitudes, namely 40 and 56 m; these flight altitudes correspond to GSDs of roughly 2 and 3 cm/px, respectively. This already suggests that for an altitude of 56 m, for example, surface water features smaller than 3 cm will remain unresolved in the application of the PIV algorithm. Figure 3.16 visualises the comparison of the time-averaged velocity maps for the two different flight altitudes at location 1; correspondingly, the velocity profiles derived from the transects therein are depicted in Figure 3.17. The figures of the velocity maps and velocity profiles for locations 2 and 3 at the Dinkel River can be found in Appendix B. Straightaway, for all three locations, the imagery corresponding to an altitude of 56 m provided a lower density vector field and showed a slightly worse agreement with the reference measurements. More specifically, the NRMSE increased from baseline values of 8.8%, 6.1% and 5.0% to values of 14.8%, 7.9% and 6.4% for locations 1, 2 and 3, respectively (Table 3.6). The NMBE values in Table 3.6 suggest that the LSPIV results corresponding to an altitude of 56 m tended to overestimate the velocity magnitudes. Despite this, the absolute velocity deviations were still relatively small. Furthermore, from a visual standpoint, the velocity fields and velocity profiles along the transects do not differ much from the baseline; this is especially true for locations 2 and 3, where the velocity profiles seem to align quite well. At location 1, on the other hand, the spatial structure of large-scale fluid motions (e.g., horizontal turbulent structures) tends to be less discernible when adopting a larger GSD; the reason for this is that a larger GSD is accompanied by a loss of spatial information in the flow field (Legleiter & Kinzel, 2020). Moreover, the slightly worse NRMSE values at location 1, relative to the other locations, may suggest that LSPIV is possibly less effective when estimating surface flow velocities in highly turbulent flows. All in all, despite the higher NRMSE values, the LSPIV result corresponding to the higher drone flight altitude can still provide meaningful insights regarding the surface water flow velocities.

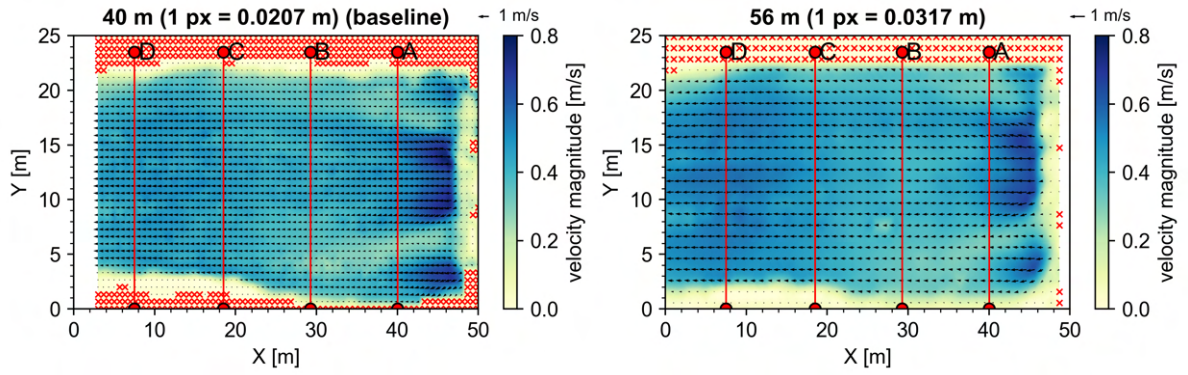

Figure 3.16: Visual comparison of time-averaged surface water flow velocity fields computed with imagery obtained at drone flight altitudes of 40 and 56 m. Imagery was acquired from a drone at location 1 in the Dinkel River study area.

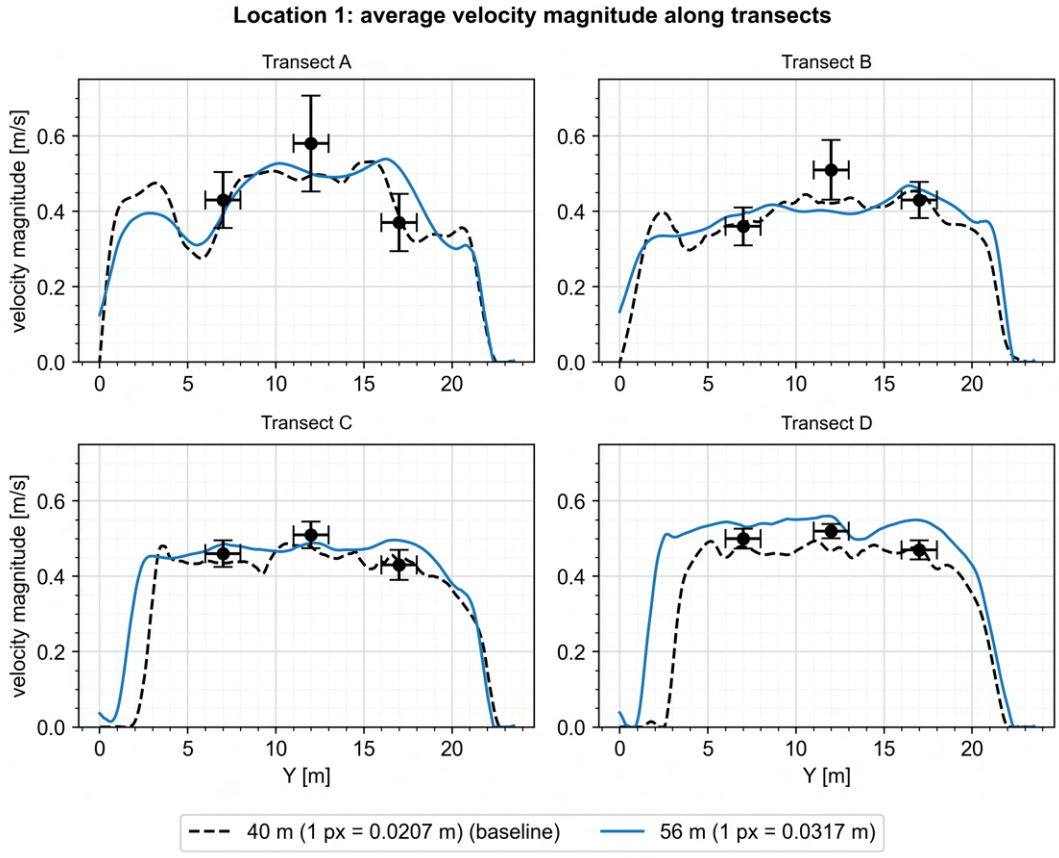

Figure 3.17: Velocity profiles extracted from the transects defined in Figure 3.16 for drone flight altitudes of 40 and 56 m. Markers represent mean surface water velocity magnitudes obtained from the float method. Uncertainty intervals surrounding the markers represent the standard deviation.

Table 3.6: Summary of error metrics for LSPIV results from the Dinkel River for drone flight altitudes of 40 and 56 m. RMSE = root mean squared error; MBE = mean bias error; RMSE and MBE were normalised by the mean velocity magnitude obtained from the float method (0.47, 0.39 and 0.40 m/s for locations 1, 2 and 3 respectively)

Flight altitude [m]	Pixel size [m]	Interrogation area size [px]	Step size [px]	Vector spacing [m]	RMSE [m/s]	MBE [m/s]	NRMSE [%]	NMBE [%]
			Location 1					
40	0.0207	64	32	0.662	0.043	0.023	8.80	4.97
56	0.0317	64	32	1.015	0.069	-0.017	14.84	-3.59
			Location 2					
40	0.0227	64	32	0.726	0.028	0.002	6.03	0.449
56	0.0293	64	32	0.936	0.037	-0.008	7.93	-1.67
			Location 3					
40	0.0214	64	32	0.685	0.020	0.015	4.97	3.91
56	0.0300	64	32	0.961	0.025	-0.015	6.41	-3.84

Image sequence duration

LSPIV generates a sequence of vector fields representing instantaneous surface water flow velocities. Within each instantaneous velocity field, chaotic behaviour can be recognised amongst the velocity vectors. Furthermore, these velocities continuously change and fluctuate across the successive velocity fields. By averaging the instantaneous velocities over a certain period of time, one may obtain a velocity field exhibiting coherent behaviour (Robert, 2003). It is within this context that the sensitivity of LSPIV to the image sequence duration was examined; this was done to address the practical question of how long the flowing water should be recorded such that the temporal variability of the instantaneous velocity fields and their contribution to the quality of the LSPIV results are no longer significant. The whole-field mean, time-averaged surface flow velocity magnitude ought to be computed and plotted as a function of the image sequence duration. The time it takes for the whole-field mean velocity magnitude to stabilise was considered to be an estimate of the minimum measurement time required to obtain reliable LSPIV results (Clasing & Muñoz, 2018). With this in mind, the full-length image sequence was progressively truncated such that image sequences with durations of 0.1, 0.2, 0.3, 0.5, 0.7, 1, 2, 4, 10, 20, 30, 40, 50 and 60 s were obtained; this process was repeated for sampling frequencies of 10, 30 and 60 Hz. The truncated image sequences were then used as input in the LSPIV analysis. It is important to note that only the imagery acquired by a drone at location 2 of the Dinkel River was considered in the analysis presented in this subsection. It is assumed that these results are also representative of the other locations.

Figure 3.18 shows the whole-field mean of the time-averaged surface water flow velocities obtained from LSPIV plotted against the image sequence duration. As can be seen in Figure 3.18, the whole-field mean velocity magnitude very quickly stabilises at values of approximately 0.39, 0.38 and 0.36 m/s for sampling frequencies of 10, 30 and 60 Hz, respectively. For all three sampling frequencies, the stabilisation appeared after 4 s. Only little change in the whole-field mean velocity is observed from 4 s onward. This means that for longer than 4 s, sufficiently reliable LSPIV results could already be obtained in this particular case. Conversely, large variations amongst the whole-field mean velocity magnitudes were found between image sequence durations of 0 and 4 s, implying that image sequence durations within this range would have been inadequate for the LSPIV implementations in this study. Additionally, the whole-field mean of the standard deviation of the velocity magnitudes was plotted against the image duration as well (Figure 3.19); this was done to assess how long it would take for the amount of temporal variability in the data set to stabilise. Once again, the standard deviation stabilised after 4 s, while the standard deviation between 0 and 4 s is quite erratic. In conclusion, the findings presented in this subsection suggest that the image sequence duration of 60 s considered in this study was plentiful.

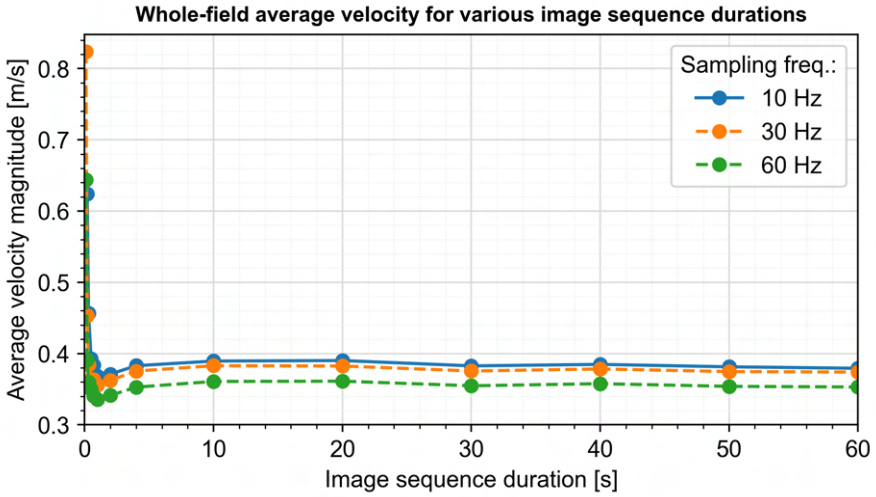

Figure 3.18: Effects of the image sequence duration on the whole-field average of the time-averaged velocities obtained by LSPIV for different sampling frequencies. Note that the LSPIV analyses were performed using images acquired at location 2.

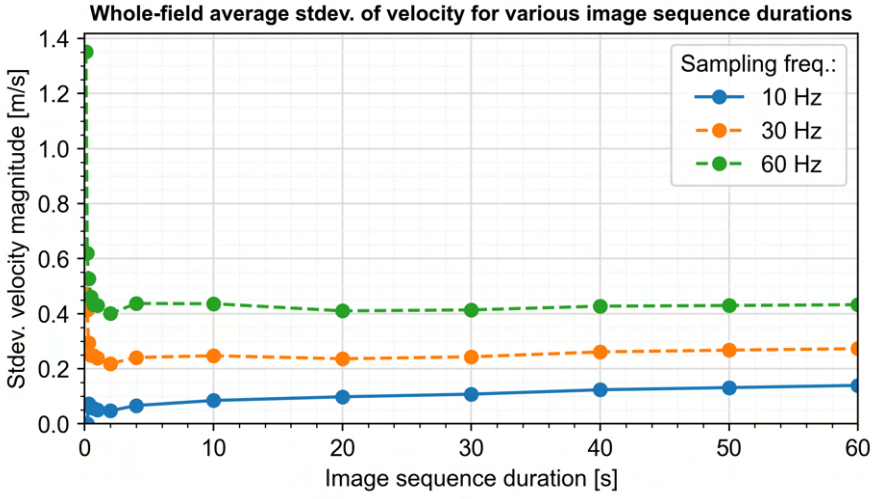

Figure 3.19: Effects of the image sequence duration on the whole-field average of the standard deviation of velocities obtained by LSPIV for different sampling frequencies. Note that the LSPIV analyses were performed using images acquired at location 2.

3.1.5. Sensitivity to image (pre-)processing

Sampling frequency

The sampling frequency, that is the time interval at which successive images are recorded, is considered an important parameter in LSPIV and directly influences the performance of the LSPIV analysis (Liu et al., 2021). However, selecting the appropriate sampling frequency is highly application-driven, meaning that the optimum sampling frequency depends on the flow conditions and PIV parameter settings (Meselhe et al., 2004). To evaluate to what degree the LSPIV performance is sensitive to the sampling frequency, image sequences sampled at five different sampling frequencies (i.e., 2, 5, 10, 30 and 60 Hz) were used as input in the LSPIV analysis (Figure 3.20). It is important to realise that the interrogation area size in this analysis was fixed at 64x64 px (approx. 2.1 m^2). From Figure 3.20 can be seen that, for all three locations, the NRMSE values increased for an increasing sampling frequency. LSPIV showed the worst performance for a maximum sampling frequency of 60 Hz; this was attributed to the fact that the particles displacements were very small in this case. Consequently, distance measurements by the PIV algorithm become inaccurate for very small particle displacements (Aberle et al., 2017). Interestingly enough, LSPIV performed much better for smaller sampling frequencies. The good

performance was attributed to the fact that the displacements of tracers between successive images were much greater for the smaller sampling frequencies; as a result, the PIV algorithm was better able to recognise the displacements of distinct patterns within the searching area. However, for a sampling frequency of 2 Hz, a quite significant increase in error was observed for location 1; this may be related to the higher flow conditions observed at location 1. Large particle displacements generally accompany high flow conditions. If the displacements are too large, a significant percentage of the tracer material may exceed the scope of the searching area, potentially leading to poor performance of the PIV algorithm (Aberle et al., 2017; Meselhe et al., 2004). With the above information in mind, it can be said that, ideally, the searching area size (or interrogation area size) should be proportional to the observed tracer displacements to obtain accurate velocity estimates.

Based on a series of laboratory tests, Meselhe et al. (2004) established an empirical relationship to estimate the optimum value for the sampling frequency in low-flow conditions. Meselhe et al. (2004) argue that the optimum sampling frequency is directly dependent on the interrogation area size and (whole-field average) surface water flow velocity. With this in mind, Meselhe et al. (2004) introduced a dimensionless number, TS, referred to as the so-called 'time step number'. The dimensionless number TS can be expressed as follows:

$$TS = \frac{\bar{V}}{SF \cdot \sqrt{A}} \tag{3.1}$$

where SF (s^{-1}) is the sampling frequency, $\bar{V}$ (m/s) is the whole-field mean velocity magnitude and A (m^2) is the interrogation area size. In their case, Meselhe et al. (2004) argue that the optimum sampling frequencies correspond to TS values ranging between 0.05 and 0.1; this is true for low-flow and uniform flow conditions. According to Equation 3.1, the optimum sampling frequency should lie between 2 and 6 Hz for both locations 2 and 3. To calculate the optimum sampling frequency for location 1, the maximum velocity magnitude in the time-averaged velocity field ought to be used rather than the whole-field average velocity, as the flow was observed to be quite nonuniform directly downstream of the weir (Meselhe et al., 2004). It was found that the optimum sampling frequency for location 1 should lie between 5 and 11 Hz. The optimum sampling frequency values obtained from the empirical relationship of Meselhe et al. (2004) (Equation 3.1) are in line with the findings of Figure 3.20; this shows that the method of Meselhe et al. (2004) may offer a helpful guide to aid the selection of the appropriate sampling frequency for LSPIV analyses. All in all, the analysis in this subsection shows that the sampling frequency is an important parameter and should be carefully selected when estimating surface water flow velocities using LSPIV.

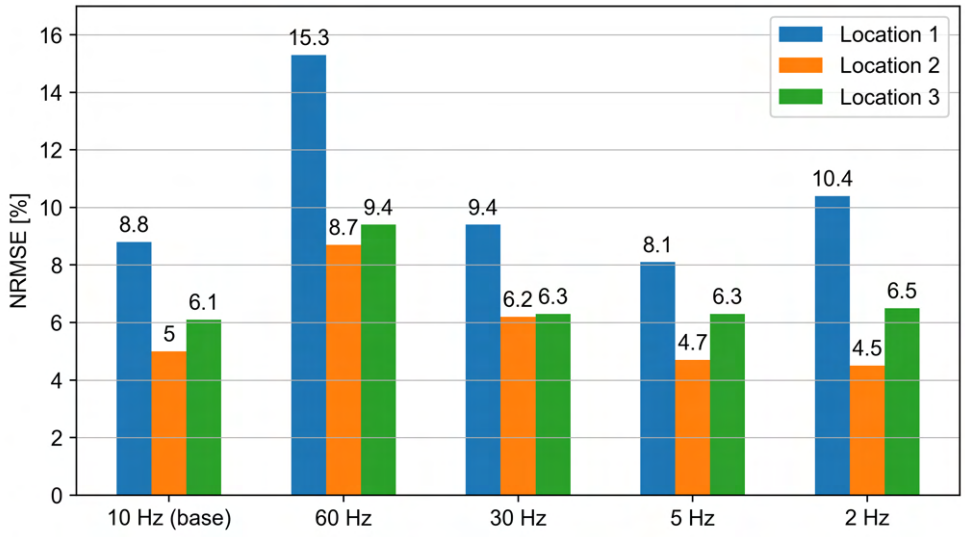

Figure 3.20: Sensitivity of the LSPIV performance to the sampling frequency for locations 1, 2 and 3 at the Dinkel River.

Image enhancement

The literature (e.g., Jolley et al., 2021; Patalano et al., 2017; Muste et al., 2008) often stressed the importance of applying image enhancement to the collected imagery; they argue that filters may significantly improve the detectability and traceability of the tracers and, therefore, may enhance the LSPIV performance. With this in mind, this subsection examined to what degree image enhancement techniques improve the accuracy of LSPIV-derived velocity estimations. Various combinations of filters were considered in this SA. More specifically, 12 different combinations of the following filters were tested: CLAHE, high-pass, intensity capping and the so-called Wiener2 denoise and low-pass filters (section 2.1.4). The reader is referred to section 2.4.2 for a complete overview of the filter combinations. Based on the findings in Figure 3.21, image enhancement did not improve the LSPIV performance in the case of the Dinkel River. If one were to use no filters at all (see C24 in Figure 3.21), the LSPIV output would be nearly identical. In addition, any other filter or combination of filters seemed to have adverse effects on the LSPIV performance. This could be because the surface features in the original, unprocessed images were already clearly distinguishable from the image background (i.e., water colour). The image enhancement techniques would then only cause deterioration of the tracer visibility. In summary, image enhancement techniques did not seem to be of great importance for the LSPIV analyses in the case of the Dinkel River.

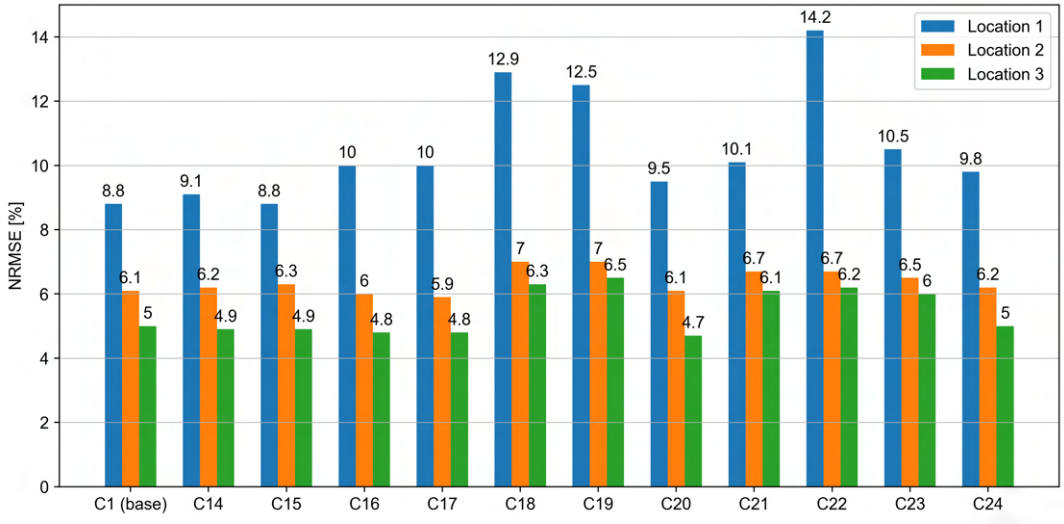

Figure 3.21: Sensitivity of the LSPIV performance to the application of image enhancement techniques for locations 1, 2 and 3 at the Dinkel River. Each case (C1, C14, C15, ...) represents a unique combination of image enhancement techniques. See Table 2.2 for an overview of the combination considered for each case.

Interrogation area size

In this subsection, the LSPIV analysis was performed for six different image interrogation area settings, namely 16x16, 32x32, 64x64, 128x128, 256x256 and 320x320 px; these interrogation area sizes correspond to coverage areas of approximately 0.36x0.36, 0.72x0.72, 1.5x1.5, 2.9x2.9, 5.8x5.8 and 7.3x7.3 m, respectively. Moreover, the searching area size is set at 50% of the interrogation area size, as this is common practice in LSPIV and PIV in general (Aberle et al., 2017; Raffel et al., 2018). It is important to note that the sampling frequency was fixed at 10 Hz during the LSPIV analyses. In Figure 3.22, the LSPIV-derived velocities showed the best agreement with the reference measurements for interrogation area sizes of 128x128 px and 256x256 px. On the other hand, the NRSME values increased for a decreasing interrogation area size. The lower accuracy associated with a smaller interrogation area may have multiple explanations. Firstly, as was mentioned earlier in this section, the tracer displacements were possibly too large; the displacement of a significant percentage of the tracers presumably exceeded the scope of the searching area as a result. Another explanation for the reduced accuracy could be that the interrogation area size was too small to recognise and capture a sufficient number of distinct surface features. For an interrogation area size of 320x320 px, the LSPIV performance was still quite satisfactory. However, one must realise that for a very large interrogation area, a consider-

able amount of spatial information will be lost in the velocity field. More specifically, adopting a very large interrogation area will lead to an unreasonably sparse vector field that cannot provide any meaningful information on the flow characteristics. In conclusion, as was established earlier, the selected interrogation area size should be proportional to the observed particle displacements and tracer sizes.

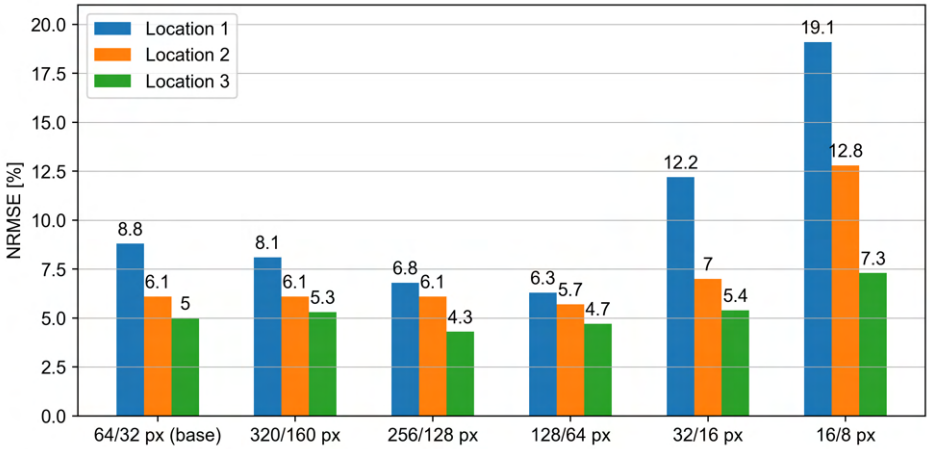

Figure 3.22: Sensitivity of the LSPIV performance to the interrogation area size for locations 1, 2 and 3 at the Dinkel River. The first value in each label in the x-axis refers to the interrogation area size, while the second value refers to the step size.

Image resolution

Earlier, the sensitivity of LSPIV to the GSD was explored by collecting imagery at different drone-flight altitudes. This time, the GSD was artificially changed by resampling the native resolution of the imagery, that is 3840x2160 px (GSD = 1.1 cm/px), to image resolutions of 2560x1440, 1920x1080 and 1280x720 px. The last three image resolutions correspond to GSDs of roughly 2.3, 3.0, and 4.6 cm/px, respectively. Figure 3.23 visualises the comparison of NRMSE values corresponding to the LSPIV analyses for the different image resolutions. Figure 3.23 shows that the accuracy of the LSPIV analysis for locations 2 and 3 was barely affected as a result of the image resolution changes. For location 1, on the other hand, the LSPIV results were found to be relatively sensitive to the image resolution. Curiously enough, the highest resolution images (1.1 cm/px) led to the worst LSPIV performance for location 1; this is possibly attributable to the fact that the advecting features on the water surface are very large relative to the pixel size, making it difficult for the PIV algorithm to recognise and match distinct patterns between interrogation areas. The aforementioned explanation is assumed to be quite plausible, since the average surface feature size at location 1 was observed to be much larger than at the other locations (Figure 3.4 and Table 3.1).

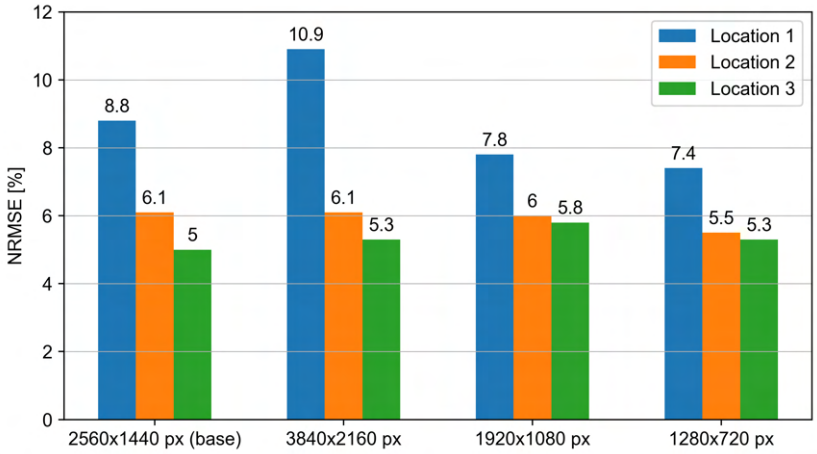

Figure 3.23: Sensitivity of the LSPIV performance to the image resolution for locations 1, 2 and 3 at the Dinkel River.

3.2. Meuse River at Sambeek

3.2.1. Data acquisition campaign

Location 1: Weir Sambeek

Figure 3.24 displays a drone-view of location 1, where the solid box delineates the ROI considered in the LSPIV analysis in this study. In Figure 3.24 can be seen that the water surface was relatively poorly coated with natural surface features. The imagery featured the highest seeding densities directly downstream of the gate of the weir, albeit spread quite inhomogeneously. Further downstream of the weir, the water surface exhibits significant tracer scarcity. Overall, the average seeding density within the ROI was estimated to be roughly 5%. In comparison, the Dinkel River showed seeding densities of 10%. Furthermore, there seems to exist a large disparity regarding the sizes of the surface features; this statement is reinforced by Figure 3.25, which shows a particularly large spread in the distribution of observed tracer diameters. The mean and median tracer diameters (25 and 17 cm, respectively) were also much larger than those observed at the Dinkel River. The most frequently observed tracer diameter was about 20 cm. Finally, continuous clustering and disintegration of the surface features could be observed close to the weir, which may have led to significant tracing errors (Kim, 2006).

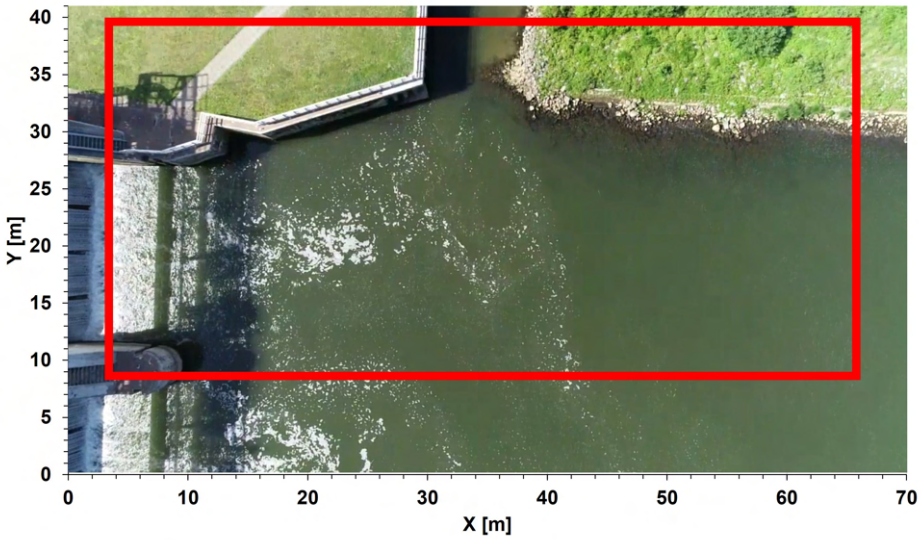

Figure 3.24: Snapshot of location 1 at Meuse River at Sambeek. Solid red box represents the ROI considered in the LSPIV analysis. Image was captured on 03 June 2022 by a drone at a flight altitude of 56 m and camera tilt angle of 0°.

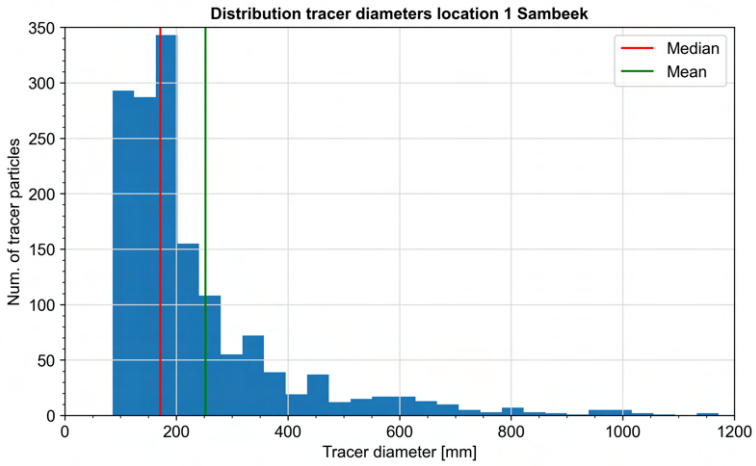

Figure 3.25: Distribution of tracer diameters at location 1 of Meuse River at Sambeek. Statistics: median diameter = 171 mm; mean diameter = 252 mm; seeding density = 5.2%

Location 2: Fish passage

Figure 3.26 displays a snapshot of the fish passage at the weir-lock complex at Sambeek (location 2). The area encompassed by the water surface in Figure 3.26 delineates the ROI considered in the LSPIV analysis in this section. The ROI features a cascade of 12 pools that discharge into each other. The average seeding density in these pools was estimated to be around 17%, which is relatively high compared to the seeding densities observed at location 1 and the Dinkel River. However, flow seeding is severely lacking at the entrance of the passage. Moreover, the mean and median tracer diameters observed at the fish passage were 18.5 and 34.2 cm, respectively (Figure 3.27). The most frequently observed tracer diameter was approximately 9 cm.

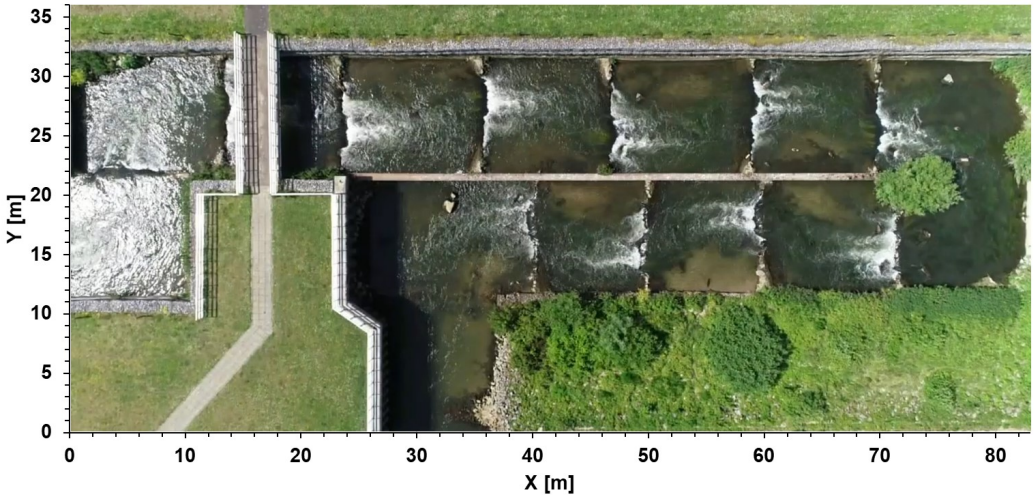

Figure 3.26: Snapshot of location 2 at Sambeek representing the ROI considered in the LSPIV analysis. Image was captured on 03 June 2022 by a drone at a flight altitude of 56 m and camera tilt angle of 0°.

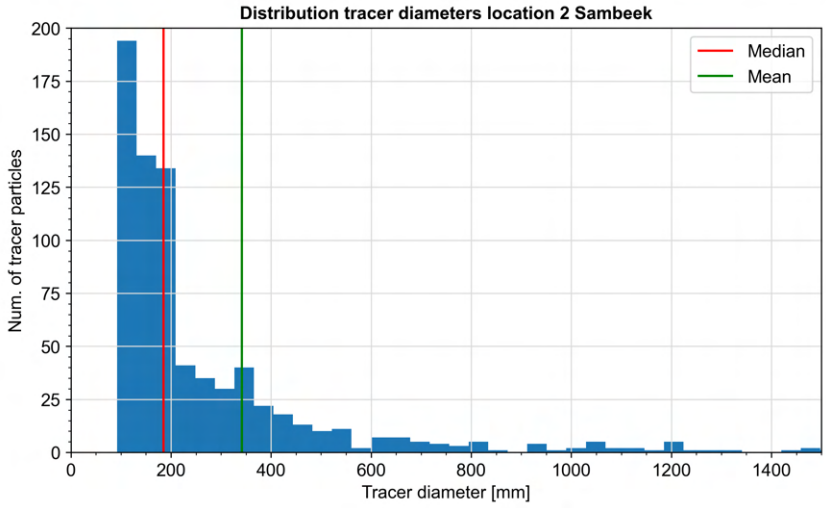

Figure 3.27: Distribution of tracer diameters at location 1 of Meuse River at Sambeek. Statistics: median diameter = 185 mm; mean diameter = 342 mm; seeding density = 17.1%

3.2.2. LSPIV analysis

Location 1: Weir Sambeek

The steps of the LSPIV workflow were followed once again to generate a time-averaged velocity map using the drone-borne imagery collected at location 1 of the Meuse River at Sambeek (Figure 3.28). Table 3.7 lists all relevant parameter settings and camera configurations employed for the LSPIV analysis. It is important to note that, in contrast to the previous LSPIV analyses, an interrogation area size of 32x32 px (1.9x1.9 m) was used instead of the conventional size of 64x64 px; this is because the spatial resolution of the drone-borne imagery was relatively coarse in this case. With this in mind, a smaller interrogation area size was required to maintain adequate vector spacing. An interrogation area size of 32x32 px should theoretically be large enough for the PIV algorithm to capture and recognise a sufficient number of surface features; this is assumed to be true, since the great majority of observed surface feature diameters are much smaller than this interrogation area size (Figure 3.25). Analogous to the LSPIV analyses of the Dinkel River, a sampling frequency of 10 Hz was deemed appropriate. Finally, the velocity fields were averaged over a time period of 120 s.

Table 3.7: Default parameter settings used in the drone-based LSPIV implementation of location 1 at the Meuse River.

Flight altitude [m]	Camera tilt angle [°]	Image resolution [px]	Sampling frequency [Hz]	Interrogation area size [px]	Pixel size [m]	Vector spacing [m]	Image enhancement technique(s)
56	0	1280x720	10	32	0.0605	0.96	CLAHE

Figures 3.28 and 3.29 visualise the output of the LSPIV analysis. Various noteworthy flow patterns can be identified in the vector field (Figure 3.28). Firstly, similar to location 1 at the Dinkel River, the greatest flow velocity magnitudes (with a maximum of 0.7 m/s) can be observed directly at the gate of the weir. As you move downstream, the surface water flow velocities quickly decrease to values between 0 and 0.25 m/s. Next, the flow exiting from the weir opening was found to interact with the water flowing in from the fish passage; approximately 30 m downstream of the weir, a convergence zone was identified at which the two inflowing streams met and diverged. Furthermore, special attention should be paid to the circulating flow structure near the fishway entrance, confirming that LSPIV can characterise relatively complex large-scale flow patterns. Such hydrodynamic characterisation capabilities of LSPIV are potentially very valuable for examining the fishway attraction efficiency under different flow conditions in the context of fish migration, as will be further elaborated in the discussion. Despite the promising results, the velocity field output appears severely impacted by the lack of flow seeding. No visible movement could be identified within the poorly seeded areas, likely resulting in a significant underestimation of velocity magnitudes.

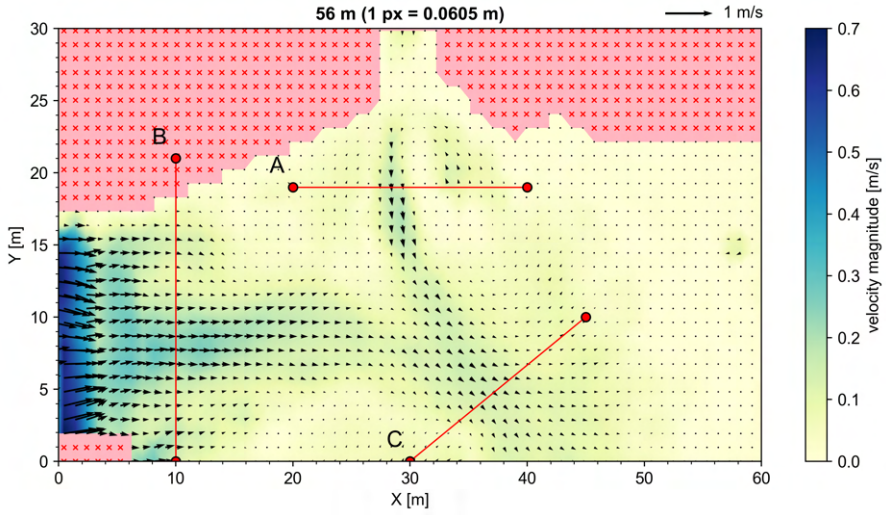

Figure 3.28: Time-averaged surface water flow velocity field for imagery acquired from a drone at location 1 in the Meuse River at Sambeek. Experimental configurations and PIV parameter settings used for the computation are specified in Table 3.7.

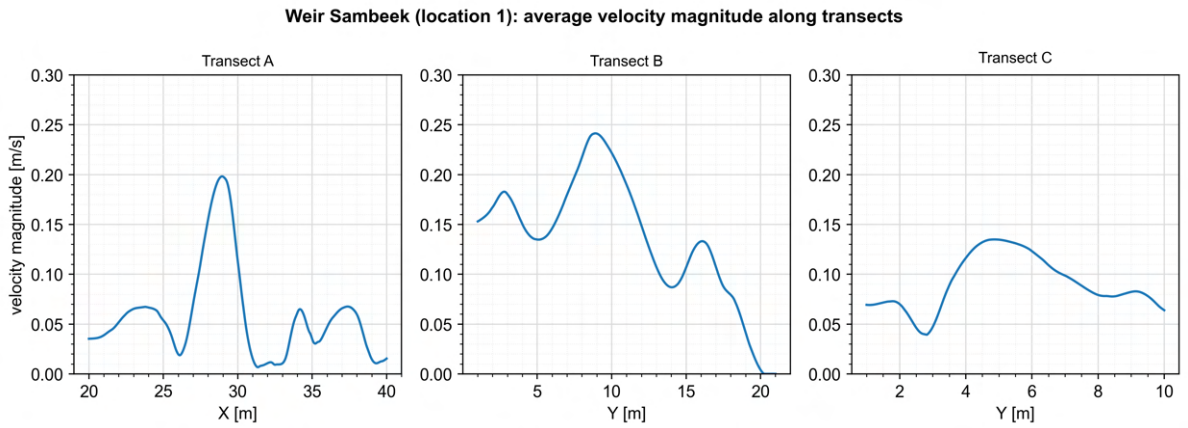

Figure 3.29: Velocity profiles extracted from the transects defined in Figure 3.28.

Location 2: Fish passage

In the drone-borne recordings of the fish passage, meandering behaviour of the flowing water could be observed. In other words, the direction of the flow within the fish passage continuously alternates with the dominant current flowing along the outer sides of the pools; at the inner side, accumulation of sediments takes place (Figure 3.26). The time-averaged LSPIV-derived velocity map (Figure 3.30) is well-able to characterise the aforementioned behaviour and seems to adequately capture the dominant flow path that is established in the fish passage. In conformity with expectation, the velocity field shows that the flow tends to concentrate towards the walls; which is quite logical, as outward transfer of flow momentum can be expected in bends (Robert, 2003). Moreover, the velocity field features relatively large flow-calmed areas where the surface flow velocity magnitudes are close to zero; the accumulated sediments in these areas suggest that this is indeed the case. Low velocity magnitudes can also be observed at the entrance (i.e., most downstream part) of the fish passage, which is most likely due to the poor seeding conditions in this area. Finally, Figure 3.31 shows the velocity profiles extracted from the transect defined in Figure 3.30. In Figure 3.31, one can see that the greatest surface velocities tend to occur just below each slot, which is where the water discharges into the downstream pool. Each pool subsequently dissipates the hydraulic energy of the inflowing water, causing a decrease in the flow velocity. The qualitative descriptions provided in this subsection are very much in line with the literature on pool-type fishways (e.g., Thorncraft & Harris 2000). This implies that LSPIV offers a promising method for capturing the spatial and temporal structure of fluid motions in fish passages and other similar hydraulic structures.

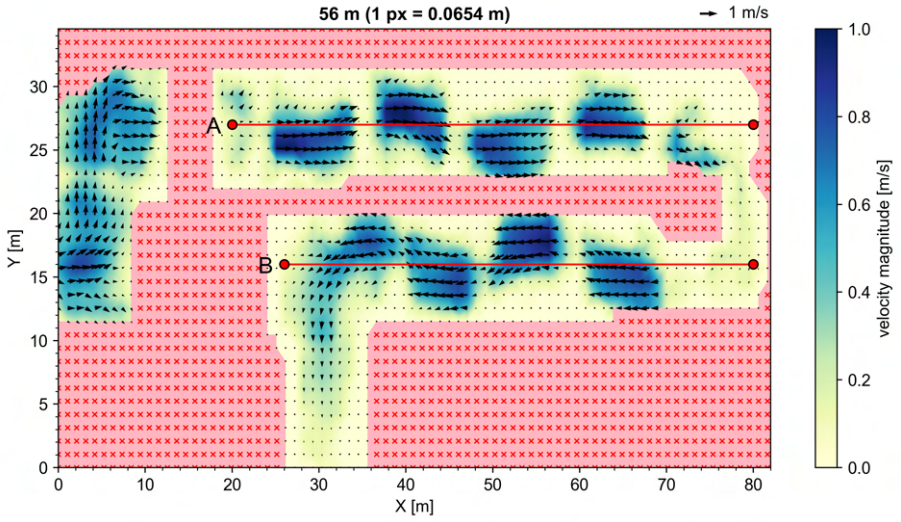

Figure 3.30: Time-averaged surface water flow velocity field for imagery acquired from a drone at location 2 in the Meuse River at Sambeek. Experimental configurations and PIV parameter settings used for the computation are specified in Table 3.7.

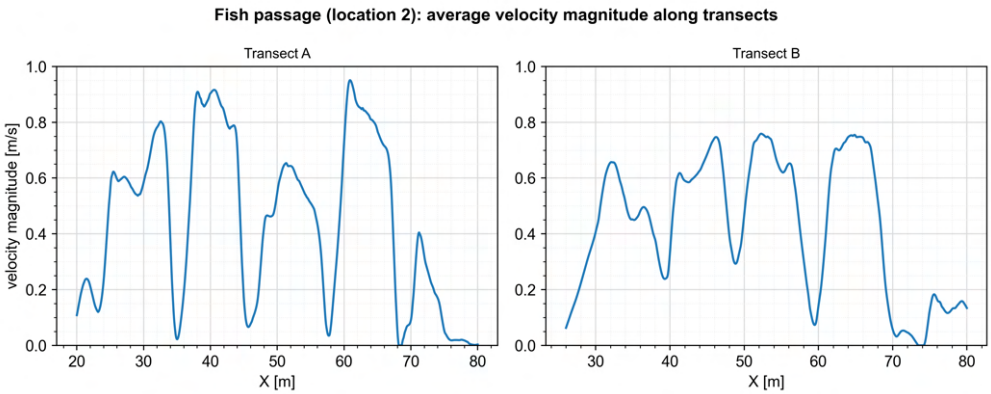

Figure 3.31: Velocity profiles extracted from the transects defined in Figure 3.30

3.2.3. Accuracy assessment

Location 1: Weir Sambeek

Once again, the float method was used to determine the accuracy of the LSPIV-derived velocity estimations at location 1 in the Meuse River. Figure 3.32 shows the arrangement of the reference measurement points within the ROI of location 1. One must realise that the tracer scarcity and highly irregular surface feature movements seriously complicated the process of determining the reference velocities. Keeping this in mind, reference velocities could only be collected properly at five measurement points; despite the limited sample size ($N = 5$), it is believed that the accuracy assessment in this subsection still provides meaningful insight as to how the PIV algorithm performed.

Table 3.8 summarises relevant details corresponding to the collected reference velocities at each measurement point. Various error metrics were calculated to determine whether the LSPIV-derived velocities agree with the reference values (Table 3.9). The error metrics in Table 3.9 suggest that there is relatively poor agreement between the observed and estimated velocity magnitudes; this is especially true vis-à-vis the results obtained at the Dinkel River. The mean absolute deviations from the reference velocities were in the order of 0.1 m/s. The positive MBE value indicates that LSPIV tended to (significantly) underestimate the velocity magnitudes. Correspondingly, the NRMSE and NMBE were found to be around 35%. The relatively high error was attributed to the poor flow seeding conditions in this case. Other factors that potentially contributed to the poor performance were the low flow conditions, highly irregular fluid motions and the fact that the patterns at the water surface were continuously changing. The aforementioned factors possibly led to significant tracing errors.

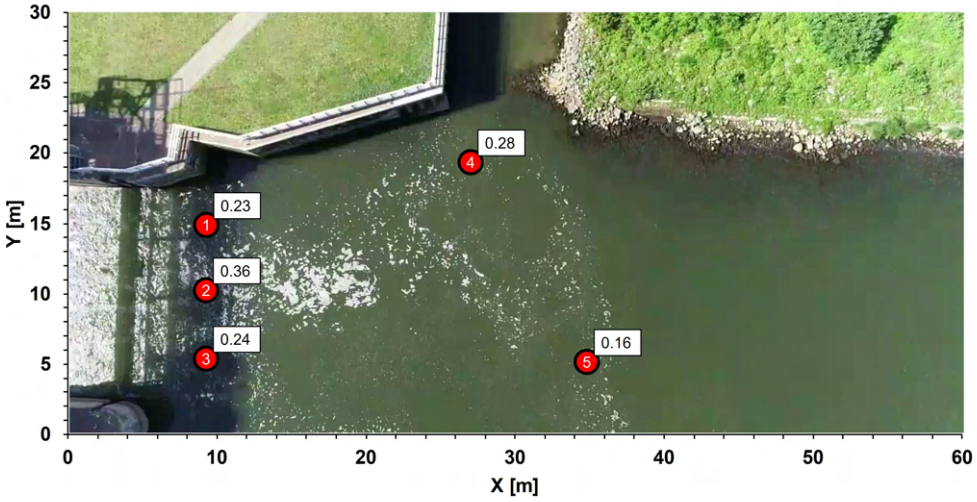

Figure 3.32: Reference measurement points with mean surface water flow velocity magnitudes (m/s) at location 1 Meuse River

Table 3.8: Overview reference measurements location 1 at Meuse River

Reference measurement	Num. of replications	Mean	Min	Max	Std
1	10	0.23	0.16	0.29	0.04
2	10	0.36	0.27	0.45	0.06
3	10	0.24	0.15	0.33	0.07
4	10	0.28	0.14	0.39	0.08
5	10	0.16	0.11	0.24	0.05

Table 3.9: Summary of error metrics for LSPIV results of location 1 at Meuse River. RMSE = root mean squared error; MBE = mean bias error; RMSE and MBE were normalised by the mean velocity magnitude obtained from the float method (0.25 m/s).

Location	Pixel size [m]	Vector spacing [m]	RMSE [m/s]	MBE [m/s]	NRMSE [%]	NMBE [%]
1	0.0605	0.96	0.092	0.089	35.73	34.51

Location 2: Fish passage

Despite the water surface being well-seeded at the fish passage, distinct features were difficult to recognise and track with the naked eye. For this reason, the float method was deemed unsuitable for the case of the fish passage. This means that direct comparisons of the flow velocities were not possible. Instead, findings in technical reports and design criteria existing in standards were used for indirect validation of the LSPIV output. Furthermore, a very rough estimation of the discharge through the fish passage was made by means of a simplified calculation according to the traditional velocity-area method ($Q = V \cdot A$); the resulting discharge value was then compared to typical discharge values.

The design of pool-type fishways along the Meuse River in the Netherlands, such as fishways located at Belfeld, Sambeek and Lith, were dictated by design criteria set by the Dutch Ministry of Agriculture, Nature and Food Quality (Lanters, 1995). The design criteria explicitly specify that the flow velocity at the slots of the pools must not exceed the maximum velocity of 1 m/s. Furthermore, the flow velocity at the entrance and exit of the fish passage must remain below 1 m/s as well. The aforementioned values give us a faint idea of the magnitude of the velocities within the fish passage at Sambeek. In this study, the LSPIV results (Figure 3.30) showed that the time-averaged velocity magnitudes at the slots of the pools generally remained below 0.9 m/s; at a few slots, maximum velocity magnitudes up to 1.0 m/s were observed. Finally, at the fish passage entrance, the velocity magnitudes ranged between 0.1 and 0.5 m/s. This shows that the velocity estimations obtained by LSPIV are plausible.

As additional validation, the discharge through the fish passage was estimated. However, one must realise that the calculation presented in this subsection was based on limited information and only provides a very crude estimation of the discharge. Firstly, based on technical drawings (Lanters, 1995), it was found that the width of the channel of the fishway is 9.90 m; it may be assumed that the cross-section of the channel is perfectly rectangular. Furthermore, according to Kranenbarg & Kemper (2006), the average water depth in the fish passage at Sambeek typically ranges between 0.5 and 1.5 m. Finally, the whole-field average surface flow velocity magnitude obtained by LSPIV is 0.25 m/s. Assuming that the surface flow velocity is representative of the depth-averaged velocity, a discharge range of 1.2 to 3.7 m^3/s was obtained. According to Lanters (1995), a typical discharge value for the fishway at Sambeek is 4 m^3/s. This again confirms that the LSPIV output is quite plausible.

3.2.4. Sensitivity to experimental configurations

As mentioned earlier in this section, conducting a comprehensive SA using the imagery collected at the Meuse River was not possible. To assess the sensitivity of LSPIV to different experimental configurations, only different drone flight altitudes and image sequence durations were considered. Different

camera tilt angles could not be tested in this case, as orthorectification of spatially distorted imagery was not feasible due to the lack of GCPs in the field. Finally, imagery of the fish passage (location 2) was disregarded in the SA, since the error metrics (e.g., RMSE) could not be calculated.

Drone flight altitude

Figure 3.33 displays the time-averaged velocity fields derived by LSPIV using image sequences collected at flight altitudes of 56 and 70 m. In this case, the altitudes of 56 and 70 m correspond to GSDs of 6.1 and 7.6 cm/px, respectively. At first glance, the velocity fields do not seem to differ much. However, the increase of the GSD did lead to a slight loss of spatial information. Nonetheless, the velocity field corresponding to the higher flight altitude is still quite capable of describing various large-scale flow structures; such as the flow at the convergence zone where the streams from the weir and fish passage meet each other. Next to that, Figure 3.34 visualises the velocity profiles corresponding to the transects. From Figure 3.34 can be seen that the effects of recording at a higher flight altitude were overall quite minor; this is especially true for transects A and B. The error metrics summarised in Table 3.10 also corroborate the aforementioned statement. The (normalised) RMSE and MBE values of the different configurations do not differ much.

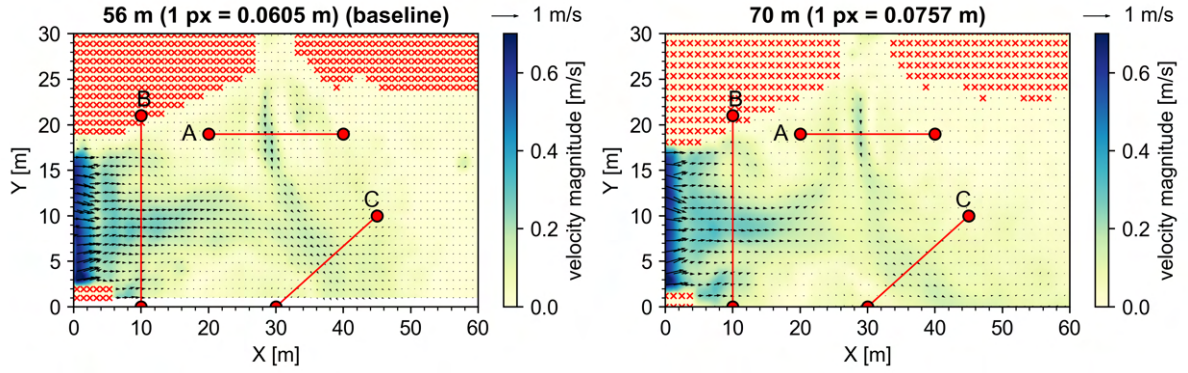

Figure 3.33: Visual comparison of time-averaged surface water flow velocity fields computed with imagery obtained at drone flight altitudes of 56 and 70 m. Imagery was acquired from a drone at location 1 at the Meuse River.

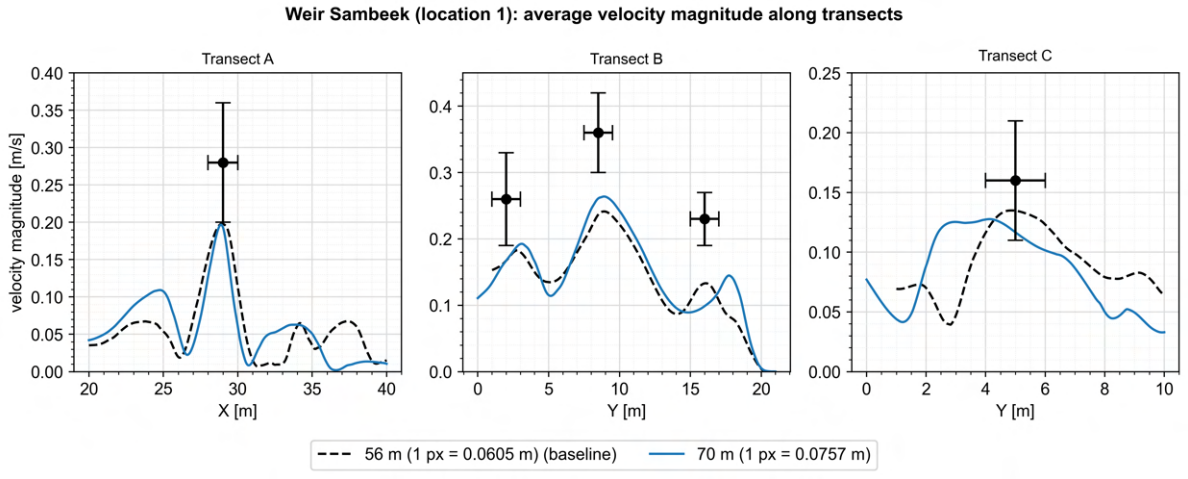

Figure 3.34: Velocity profiles extracted from the transects defined in Figure 3.33 for drone flight altitudes of 56 and 70 m. Markers represent mean surface water velocity magnitudes obtained from the float method. Uncertainty intervals surrounding the markers represent the standard deviation.

Table 3.10: Summary of error metrics for LSPIV results of location 1 at the Meuse River for drone flight altitudes of 56 and 70 m. RMSE = root mean squared error; MBE = mean bias error; RMSE and MBE were normalised by the mean velocity magnitude obtained from the float method (0.26 m/s).

Flight altitude [m]	Pixel size [m]	Interrogation area [px]	Step size [px]	Vector spacing [m]	RMSE [m/s]	MBE [m/s]	Normalised RMSE [%]	Normalised MBE [%]
56	0.0605	32	16	0.96	0.092	0.089	35.73	34.51
70	0.0757	32	16	1.21	0.096	0.094	37.39	36.26

Image sequence duration

For the Dinkel River, it was established that an image sequence duration of 4 s may already be enough for the LSPIV analysis. Figures 3.35 and 3.36 suggest, however, that a much longer image sequence duration is required for the case of location 1 at the Meuse River. The results of the SA presented in this subsection show that the whole-field mean (and standard deviation) converged only after 40 to 60 s; this is true for sampling frequencies of 10 as well as 30 Hz. The much longer observation time that is required for the Meuse River study area is likely due to the poor seeding conditions; this claim is reinforced by findings of Jolley et al. (2021), Pumo et al. (2021) and Pizarro et al. (2020), who argue that short image sequence durations tend to lead to inaccurate velocity field characterisations in poorly seeded flows. An increment in the image sequence duration allegedly increases the number of traceable particles within the ROI and, therefore, increases the number of velocity values sampled in space (Pumo et al., 2021). Nevertheless, it is important to realise that the time-averaged velocity fields, in this case, would still include spurious, zero-velocity measurements, likely resulting in an underestimation of the surface flow velocities (Pizarro et al., 2020). All things considered, the video duration of 120 s was deemed long enough in this case. However, it must be emphasised that the appropriate image sequence duration is highly case-specific and needs careful consideration prior to the LSPIV analysis.

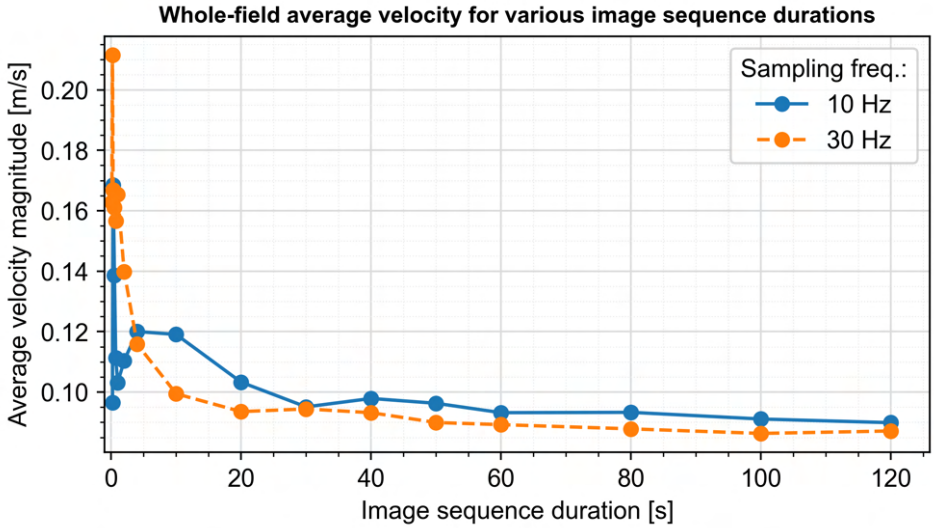

Figure 3.35: Effects of the image sequence duration on the whole-field average of the time-averaged velocities obtained by LSPIV for different sampling frequencies. Note that the LSPIV analyses were performed using images acquired at location 1 of the Meuse River study area

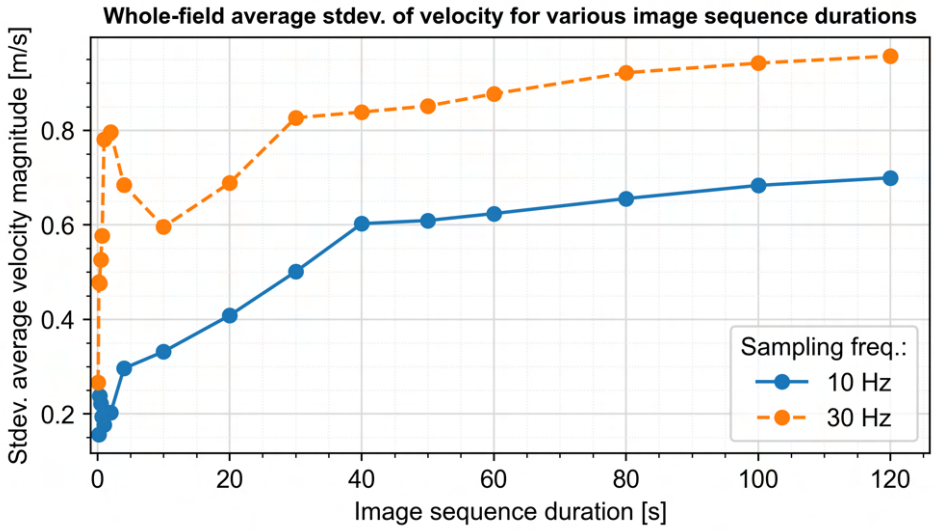

Figure 3.36: Effects of the image sequence duration on the whole-field average of the standard deviation of velocities obtained by LSPIV for different sampling frequencies. Note that the LSPIV analyses were performed using images acquired at location 1 of the Meuse River study area

3.2.5. Sensitivity to image (pre-)processing

Sampling frequency

Once again, the LSPIV analysis was performed with a variable sampling frequency (Figure 3.37). The findings of the SA yet again confirm that the sampling frequency is a key parameter in LSPIV and is one of the dominant controls of the LSPIV accuracy. The LSPIV-derived velocity estimations showed much better agreement with the reference measurements for lower sampling frequencies. By lowering the sampling frequency from the baseline value of 10 Hz to 2 Hz, the NRMSE value dropped from 36% to 20%. The poor performance associated with high sampling frequencies is again attributed to the particle displacements between successive images being very small relative to the interrogation area size. When using the optimum sampling frequency range proposed by Meselhe et al. (2004), i.e. $10\frac{\bar{V}}{\sqrt{A}} \leq SF \leq 20\frac{\bar{V}}{\sqrt{A}}$ (Equation 3.1), we find that the optimum value should lie between 1 and 3 Hz; the results of the SA verify that this is indeed the case.

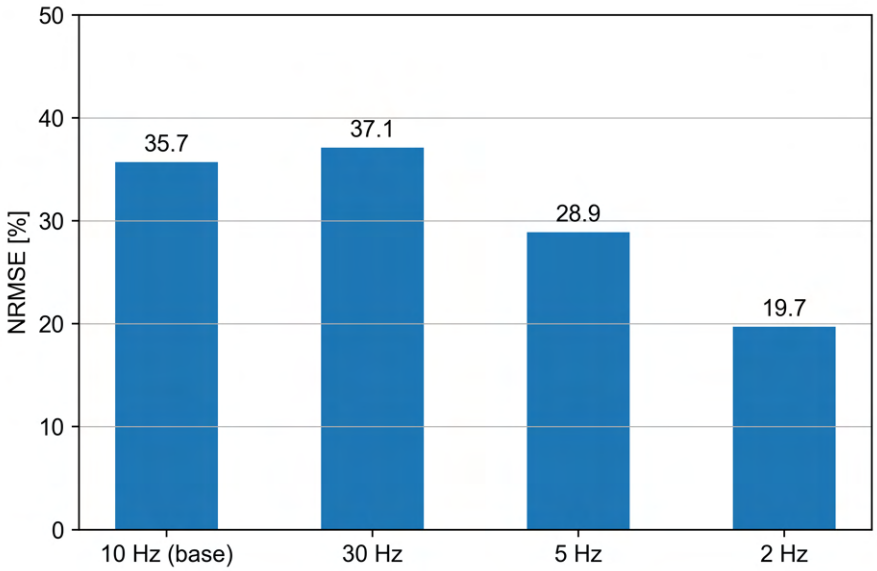

Figure 3.37: Sensitivity of the LSPIV performance to the sampling frequency for location 1 at the Meuse River.

Image manipulation

Figure 3.38 summarises the NRMSE values for 12 unique combinations of image enhancement techniques. The reader is referred to section 2.4.2 for an overview of all filter combinations considered in this SA. Again, the SA shows that the LSPIV output is not very sensitive to image enhancement. Analogous to the Dinkel River case, it can be concluded that image enhancement prior to the LSPIV analysis is not likely to improve the accuracy of the velocity estimations.

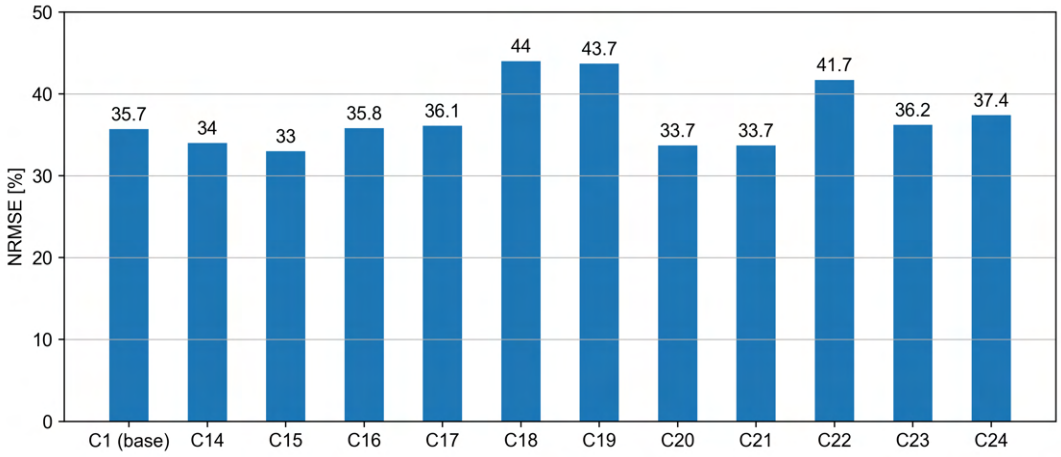

Figure 3.38: Sensitivity of the LSPIV performance to the application of image enhancement techniques for location 1 at the Meuse River. Each case (C1, C14, C15, ...) represents a unique combination of image enhancement techniques. See Table 2.2 for an overview of the combination considered for each case.

Interrogation area size

Figure 3.39 summarises the NRSME values corresponding to the LSPIV analyses performed using different interrogation area sizes. The best performance was observed for interrogation areas of 32x32 px (1.9x1.9 m) and 16x16 px (0.97x0.97 m). On the other hand, rather significant deterioration of the LSPIV performance was witnessed by enlarging the interrogation area size. This is presumably because the frame-by-frame particle displacements on the water surface were excessively small with respect to the interrogation area size, which negatively affected the pattern matching performance of the PIV algorithm.

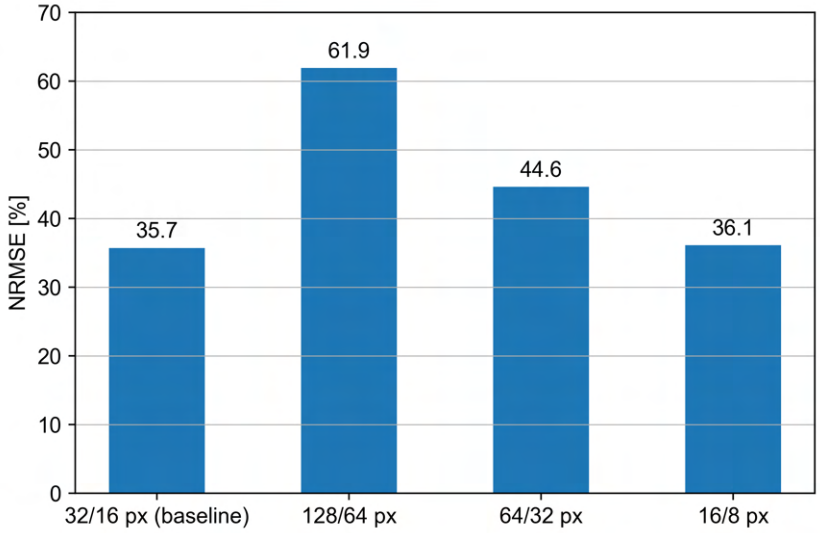

Figure 3.39: Sensitivity of the LSPIV performance to the interrogation area size for location 1 at the Meuse River. The first value in each label in the x-axis refers to the interrogation area size, while the second value refers to the step size.

3.3. Comparison drone-based and fixed camera implementations

Traditionally, LSPIV has mainly used ground-based imaging solutions to collect imagery to measure surface water flow velocities in fluvial applications. It was only until recently that drone-based approaches were considered viable alternatives in this regard (Rhee et al., 2018). However, there remains limited knowledge about how drone-based LSPIV performs compared to fixed camera implementations (Tauro et al., 2016a). Against this background, this thesis aimed to explore the differences between drone- and ground-based LSPIV implementations with an eye toward surface water flow velocity estimation capabilities. As was mentioned earlier in this chapter, video recordings were collected at locations 2 and 3 of the Dinkel River using a camcorder mounted on a tripod; these recordings were then used as input in LSPIV analyses. Measurements from the fixed LSPIV configurations were then compared to the drone-borne data.

3.3.1. Location 2 Dinkel River

This subsection compares drone-based and fixed camera LSPIV implementations for location 2 of the Dinkel River. Figure 3.40a presents the ROI considered in the comparison; as can be seen from this figure, the perimeter of the ROI was defined based on the common area of coverage. Furthermore, it is worth noting that the ROI does not reach beyond the area encompassed by the GCPs. This was to ensure that the orthorectification procedure could be carried out correctly. Moreover, Figure 3.40b provides an impression of the FoV captured by the stationary camera; from this figure can be seen that the camera axis of the stationary configuration is inclined quite considerably with respect to the water surface. Experience tells that such a camera tilt angle is already a harbinger of inadequate LSPIV performance. An important reason for this is that significant distortion will be introduced onto the imagery due to the (explicit or implicit) orthorectification process (Hauet et al., 2008b). To illustrate this, Figure 3.41 shows which pixel size (m/px) each pixel attains within the ROI for the images captured by the stationary camera; this figure suggests that a large portion of the ROI (especially far field of image) will be subject to significant error associated with converting pixel sizes to real-world dimensions.

For the drone-based LSPIV implementation, an experimental configuration comprising a drone flight altitude of 40 m and camera tilt angle of 0° was considered. Furthermore, analogous to the previous sections, an image resolution of 2560x1440 px and image sequence duration of 60 s were considered for the LSPIV analysis. In addition, based on the findings of the SA performed earlier, it had been decided that an interrogation area size of 64x64 px and sampling frequency of 5 Hz would be most appropriate in this case. Lastly, the images were enhanced prior to the vector field computation by applying the CLAHE filter. For the fixed camera LSPIV implementation, a 1920x1080 px image resolution was used; apart from that, the same parameter settings as for the drone-based LSPIV were adopted. Finally, the LSPIV analysis in the fixed camera case involved reconstructing the spatially distorted images through orthorectification. The orthorectification procedure was performed implicitly rather than explicitly, as the SA in this thesis showed particularly good results for the implicit approach.

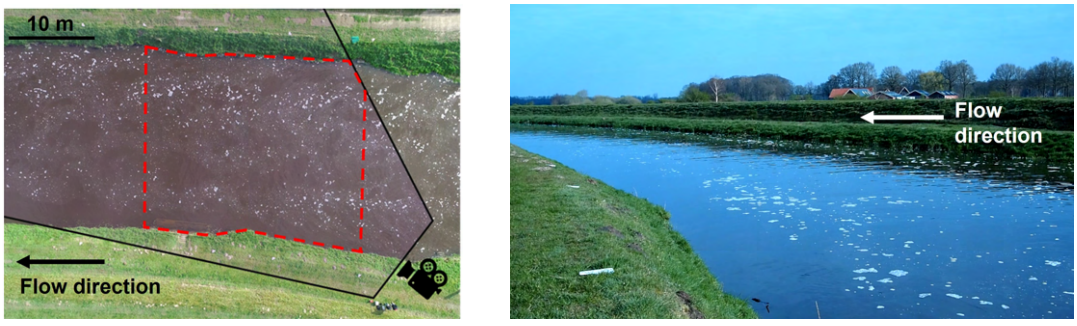

(a) (b)

Figure 3.40: Location 2 at the Dinkel River: (a) drone-view of location 2, the solid black box represents the FoV of the stationary camera and the dashed red box delineates the ROI considered for the comparison between drone-based and fixed camera LSPIV; (b) snapshot of the video recorded by the stationary camera.

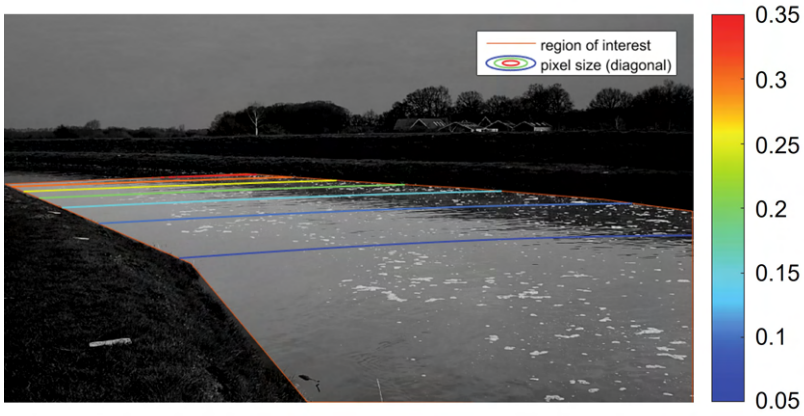

Figure 3.41: Pixel sizes (m/px) of pixels within the ROI of location 2 in the Dinkel River study area. A larger pixel size indicates a larger error associated with orthorectification (Patalano et al., 2017)

The results of the velocity assessments of the two different experimental configurations are visualised in Figures 3.42 and 3.43. The velocity field corresponding to the stationary camera is characterised by an exceptionally high error, with RMSE and NRSME values of 0.23 m/s and 48%, respectively (Table 3.11). The positive, but comparatively low, MBE and NMBE values imply that the fixed camera LSPIV implementation has a moderate tendency to underestimate the velocity magnitudes. Next to the quantitatively poor performance of the fixed camera LSPIV analysis, seemingly inexplicable behaviour of the flow can be observed as well. More specifically, the velocity field and velocity profiles of the stationary camera show a relatively thin trail of high velocity magnitudes running through the middle of the stream. After careful inspection of the video recordings, it is believed that this peculiar behaviour is attributed to the presence of small propagating wind waves on the water surface (Figure 3.42), which likely led to flow-independent velocity measurements in the LSPIV analysis. In contrast, water surface distortions caused by wind effects are barely noticeable in the drone-borne imagery. Having said that, the overall poor performance of the fixed camera LSPIV implementation is likely caused by a combination of factors and error sources; for the sake of brevity, the main (alleged) culprits for the poor performance are briefly listed below:

- Despite the overcast weather, strong glare and excessive amounts of sun glitter could be observed on the water surface, which are well-known sources of error in LSPIV (Jolley et al., 2021);
- Small features were barely visible due to the non-uniformity of the water surface luminosity;
- Poor visibility of surface patterns was identified in the far field of the image as a result of the perspective distortions associated with the camera inclination;
- The orthorectification procedure was unable to properly reconstruct the geometry of the river;
- Wind effects induced much noise in the imagery, resulting in flow-independent velocity measurements.

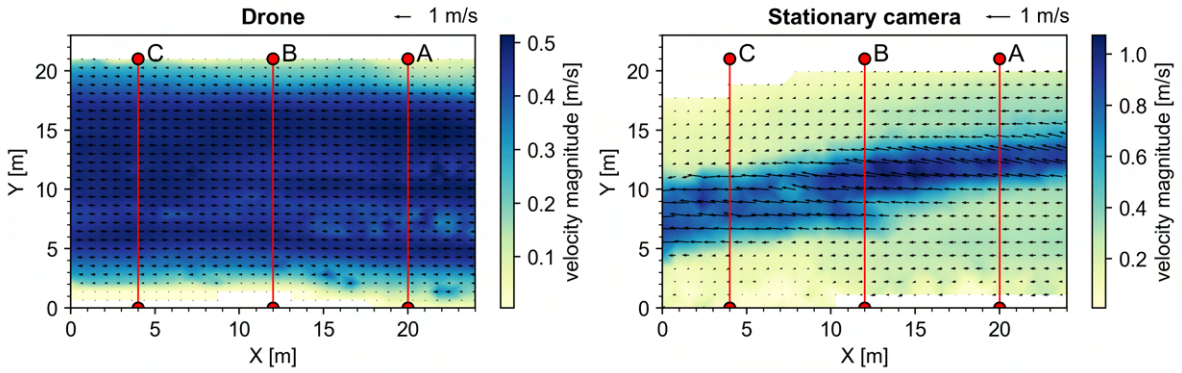

Figure 3.42: Visual comparison of time-averaged surface water flow velocity fields computed with imagery obtained from a drone and stationary camera. Images were acquired at location 2 in the Dinkel River study area.

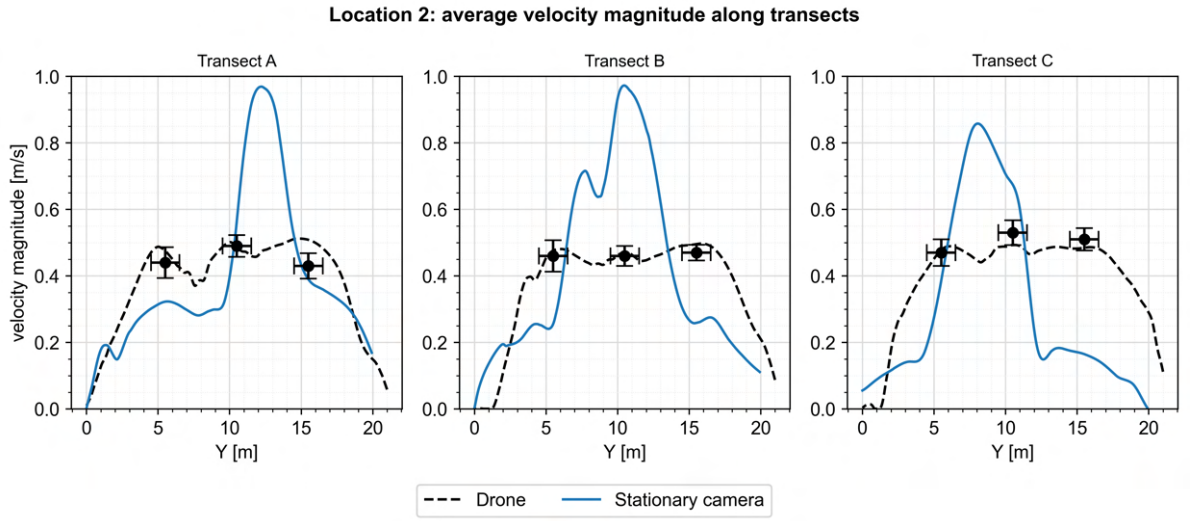

Figure 3.43: Velocity profiles extracted from the transects defined in Figure 3.11 for drone-based and fixed camera LSPIV. Markers represent mean surface water velocity magnitudes obtained from the float method. Uncertainty intervals surrounding the markers represent the standard deviation.

Table 3.11: Summary of error metrics of location 2 at the Dinkel River for drone-based and fixed camera LSPIV. RMSE = root mean squared error; MBE = mean bias error; RMSE and MBE were normalised by the mean velocity magnitude obtained from the float method (0.47 m/s).

Imaging platform	Pixel size [m]	Interrogation area [px]	Step size [px]	Vector spacing [m]	RMSE [m/s]	MBE [m/s]	Normalised RMSE [%]	Normalised MBE [%]
Drone	0.0227	64	32	0.73	0.033	-0.01	7.1	-2.0
Stationary camera	0.0247	64	32	1.11	0.23	0.035	48.1	7.4

3.3.2. Location 3 Dinkel River

Figure 3.44a illustrates the stream portion of interest that was considered in the comparison. It is worth noting that the ROI only spans a streamwise distance of 12 m due to the limited FoV of the stationary camera. Once again, it is expected that the perspective distortion associated with the inclined view of the camera will induce additional error on a significant portion of the ROI (Figure 3.45). For a description of the parameter settings considered in the LSPIV analyses, the reader is referred to the previous subsection (section 3.3.1).

(a) (b)

Figure 3.44: Location 3 at the Dinkel River: (a) drone-view of location 3, the solid black box represents the FoV of the stationary camera and the dashed red box delineates the ROI considered for the comparison between drone-based and fixed camera LSPIV; (b) snapshot of the video recorded by the stationary camera.

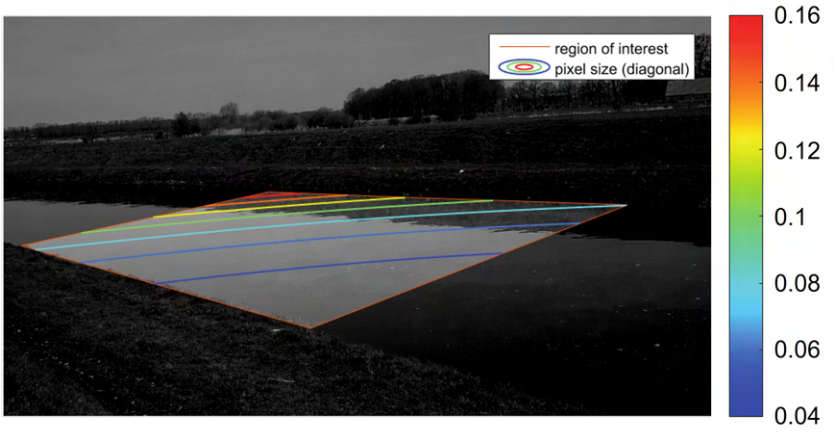

Figure 3.45: Pixel sizes (m/px) of pixels within the ROI of location 3 in the Dinkel River study area. A larger pixel size indicates a larger error associated with orthorectification (Patalano et al., 2017).

Figures 3.46 and 3.47 present the results of the LSPIV analyses performed in this subsection. As expected, the LSPIV analysis reveals a satisfying accuracy in reproducing the surface water flow velocity field at location 3 for the drone-borne imagery. The drone-based LSPIV output is well-able to qualitatively characterise the flow characteristics within the stream portion of interest and showed comparatively low error with RMSE and NRMSE values of 0.03 m/s and 6.3 %, respectively (Table 3.12). In contrast, the fixed camera LSPIV output is once again of substandard quality. Whereas, in the case of location 2, the vector field corresponding to the stationary camera showed somewhat coherent behaviour, here the LSPIV analysis completely failed to provide anything meaningful; to illustrate this, the vector field shown in the right panel of Figure 3.46 exhibits erratic behaviour and is mainly dominated by noise. Furthermore, similar to location 2, a trail of high-velocity values was observed in the velocity field; this phenomenon is again attributed to the illumination non-uniformity and ripples on the water surface (Figure 3.44b). The velocity profiles at the defined transects (Figure 3.47) also show random undulations and, hence, fail to reproduce realistic cross-stream velocity profiles. Accordingly, the RMSE and NRMSE values are 0.22 m/s and 55% for the stationary camera, respectively, while the MBE and NMBE are 0.04 m/s and 51%, respectively. The resounding failure of the fixed camera LSPIV implementation can be explained by the fact that the features advected on the water surface were not visible due to the suboptimal illumination conditions. Additionally, the error sources mentioned in the previous subsection also largely apply to this case. All in all, the experimental findings presented in this section support and greatly favour the use of drones to estimate surface water flow velocities in large-scale fluvial applications; the significant inclination of the camera axis of the stationary camera setup was found to be detrimental for the measurement accuracy.

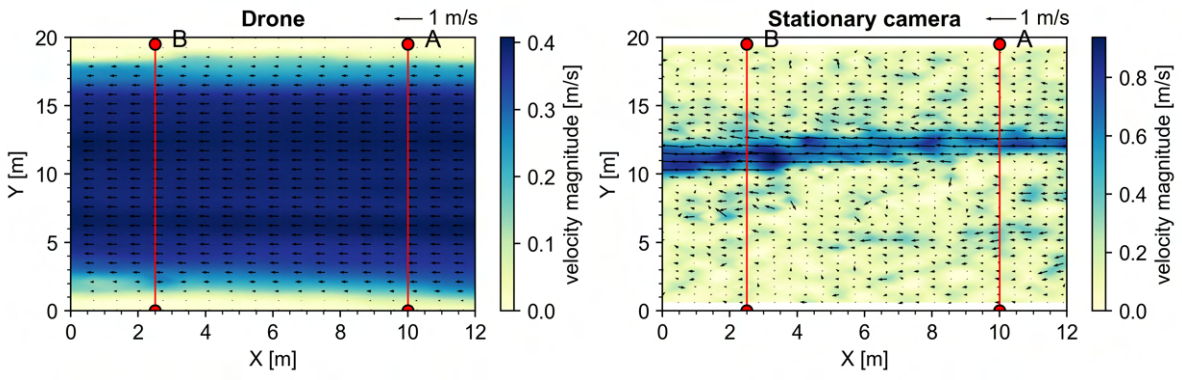

Figure 3.46: Visual comparison of time-averaged surface water flow velocity fields computed with imagery obtained from a drone and stationary camera. Images were acquired at location 3 in the Dinkel River study area.

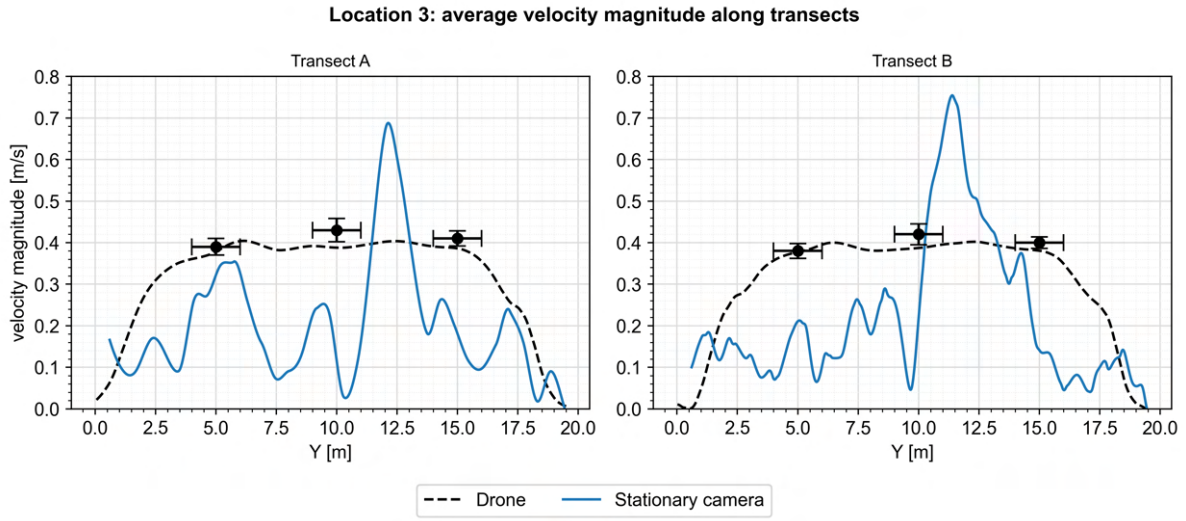

Figure 3.47: Velocity profiles extracted from the transects defined in Figure 3.12 for drone-based and fixed camera LSPIV. Markers represent mean surface water velocity magnitudes obtained from the float method. Uncertainty intervals surrounding the markers represent the standard deviation.

Table 3.12: Summary of error metrics of location 3 at the Dinkel River for drone-based and fixed camera LSPIV. RMSE = root mean squared error; MBE = mean bias error; RMSE and MBE were normalised by the mean velocity magnitude obtained from the float method (0.40 m/s).

Imaging platform	Pixel size [m]	Interrogation area [px]	Step size [px]	Vector spacing [m]	RMSE [m/s]	MBE [m/s]	Normalised RMSE [%]	Normalised MBE [%]
Drone	0.0214	64	32	0.69	0.026	0.022	6.3	5.5
Stationary camera	0.0159	64	32	0.57	0.22	0.035	54.5	51.2

4
Discussion

The first section of the discussion provides general remarks regarding the rationale behind this research and the practical significance of drone-based LSPIV. The second section explains how the findings of this research fit the current knowledge in the literature; furthermore, this section also briefly touches upon some possible applications of drone-based LSPIV and relevant limitations associated with LSPIV in general. The final section presents the main limitations and challenges encountered in this thesis and, subsequently, provides recommendations for future research.

4.1. Significance and main innovations

The main objective of this thesis was to contribute to the knowledge on using remote sensing techniques and LSPIV methods to infer surface water flow velocities in unseeded flows within large-scale fluvial applications. In this case, unseeded flows refer to flows in which no artificial tracers are introduced and, hence, strictly rely on naturally occurring features to achieve flow seeding. With this in mind, an important aim of this research was to investigate the potential value of naturally occurring surface features as an alternative to artificial tracers. Another aim of this thesis was to provide insight into how the dominant error sources affect the LSPIV application in such environments; this was done as an attempt to provide guidance and a more systematic approach to selecting the appropriate processing parameters in LSPIV. In addition, this thesis aimed to provide a more process-based explanation as to why or how certain experimental configurations are effective or ineffective when applying LSPIV.

The reasons and motivation for the research work presented in this thesis can be linked to the findings and limitations of similar studies. More specifically, this thesis is essentially built on the works of Veldhuizen (2021), Koutalakis et al. (2019) and Legleiter & Kinzel (2020). Veldhuizen (2021) employed drone-based LSPIV techniques at the Eastern Scheldt storm surge barrier in the Netherlands. This was done with the specific aim of studying complex, large-scale flow phenomena that emerged due to the strong contraction of the tidal flow through the barrier. LSPIV was successfully applied to the drone-borne imagery collected at the landward side of the barrier, and they were able to characterise major elements of the surface flow, such as jet-like flow structures and horizontal recirculation zones; it was argued that the presence of the barrier allowed for high density and homogeneous seeding, which was essential to obtain useful velocity fields. To give an idea of the LSPIV measurement accuracy, Veldhuizen (2021) found average absolute differences of roughly 0.2 to 0.6 m/s between the LSPIV-derived surface water flow velocities and reference measurements obtained from an ADCP; the time-averaged velocity fields obtained from the LSPIV analysis generally showed surface water velocity magnitudes in the order 1 and 3 m/s. The findings of Veldhuizen (2021) motivated this research to further investigate the capabilities of drone-borne imaging techniques and LSPIV to measure surface water flow velocities in unseeded flows near hydraulic structures. While Veldhuizen (2021) showed promising results, they provided little rationale for the choice of processing parameters and experimental configurations. Furthermore, it remains unclear how and to what extent the dominant error sources affected the LSPIV-derived flow velocity estimations in the work of Veldhuizen (2021). Similarly, Koutalakis et al. (2019) analysed surface flow velocities near an agricultural pipeline constructed in the Aggitis River in Greece. Due to the interaction of the flowing water and the pipeline, turbulence patterns along with foam and air bubbles were generated on the water surface. Koutalakis et al. (2019) argue that these surface features were particularly suitable for LSPIV implementations. However, Koutalakis et al. (2019) were

unable to perform an accuracy assessment as reference velocity measurements could not be collected on-site. Therefore, they could not assess whether LSPIV can provide accurate velocity estimations in such an environment. On top of that, the LSPIV analyses in the work of Koutalakis et al. (2019) heavily relied on a trial-and-error approach and they did not justify any of their decisions regarding the selection of PIV processing parameters. Finally, another recent achievement worth mentioning relates to the study of Legleiter & Kinzel (2020). Legleiter & Kinzel (2020) used naturally occurring features as well to achieve flow seeding in large Alaskan rivers with average surface flow velocities of 1.5 to 2 m/s; however, instead of foam and air bubbles, they exploited boil vortices containing suspended sediment. Based on an extensive accuracy assessment, they found that the flow velocity estimations were in good agreement with field estimates from an ADCP; RMSE and MBE values of 0.09 m/s and 0.06 m/s, respectively, were obtained from the comparison between the LSPIV and ADCP measurements. This once again convincingly demonstrates that, under the right conditions, natural tracers may potentially be used for flow seeding and the use of artificial tracers may be circumvented. However, in spite of the efforts mentioned in this section, research is still lacking on the application of LSPIV in unseeded flows. The research work in this thesis attempted to overcome the shortcomings of the aforementioned studies by rigorously testing the capabilities of drone-based LSPIV by considering different environments and conducting an extensive sensitivity analysis. Similar sensitivity analyses have been done in the past (e.g, Meselhe et al., 2004; Muste et al., 2008; Dal Sasso et al., 2020; Tauro et al., 2016a; Pizarro et al., 2020); however, these studies have mainly focused on small-scale, artificially seeded flows.

Whereas the majority of existing literature and case studies tended to focus on relatively narrow rivers and streams, this research has been directed towards larger water systems; this research has mainly focused on river reaches that are wider than 20 m and extend for over tens of metres in the streamwise direction. Next, it is common practise in LSPIV to utilise artificial tracers for flow seeding. However, an important limitation of using artificial tracers is that they are ill-suited for large-scale water systems. Ensuring continuous and adequate seeding is highly impracticable in large-scale fluvial systems and, therefore, the application of LSPIV in such environments is severely impeded; this challenge was a great opportunity to explore the possibilities of using alternative ways to achieve flow seeding. This brings us to one of the main innovative aspects of this thesis, namely, using naturally occurring features on the water surface as flow seeding. Within this context, the LSPIV implementations in this study focused on flows near hydraulic structures, as the interaction of the flowing water with the hydraulic structure gives rise to turbulence patterns along with the generation of foam and air bubbles on the water surface. Next to the high practicality of natural flow seeding, it also presents other important benefits; for example, data collection is less laborious and fewer resources are required, leading to a cost reduction of the data acquisition campaign. Another important advantage is that the flow is continuously seeded, which allows one to observe the flow for a long period of time. In contrast, experimental observations in the case of artificial seeding generally suffer from serious time constraints. To illustrate this, LSPIV studies that artificially introduced tracers to the flow (e.g., Bandini et al., 2021; Strelnikova et al., 2020; Tauro et al., 2016a; Sutarto, 2015; Meselhe et al., 2004) were only able to obtain image sequence durations of several seconds or even milliseconds. The findings in this research revealed that very short image sequence durations may drastically reduce the measurement accuracy. A final benefit worth mentioning is that pollution of the water system may be avoided when exploiting natural tracers rather than artificial tracers.

The second innovative aspect of this research relates to the fact that a drone was used to acquire imagery. Even though drones have been employed extensively in various research areas and fluvial applications, drone-based approaches in LSPIV are still relatively uncommon (Rhee et al., 2018). Conventionally, LSPIV has mainly used terrestrial imaging platforms positioned on a bridge or river bank. Although such fixed camera solutions have high operational reliability and are easy to operate, they are subject to some serious limitations; for example, fixed camera LSPIV cannot be used in inaccessible and hazardous environments. Furthermore, the literature (e.g., Jolley et al., 2021; Legleiter & Kinzel, 2020; Tauro et al., 2016b) often mentioned that the applicability of fixed camera configurations is limited in large-scale water systems, as it only captures a small field of view. The aforementioned statement is corroborated by experiments carried out in this research. Because of the reduced field of view, the fixed camera configurations employed in this research could not capture all GCPs placed on the river banks. The limited spatial coverage of the fixed camera complicated the orthorectification procedure,

as preferably all GCPs should be visible to minimise error associated with image transformations (Jolley et al., 2021). Moreover, the fixed camera configurations could not image the entire water surface of the stream portions of interest. This was due to the significant inclination of the camera axis with respect to the water surface, causing the southernmost river bank to obstruct the view of a part of the river (Figures 3.40b and 3.44b). In contrast, the drone-based experimental configurations in this study did not encounter any of the abovestated limitations.

4.2. Implications, applications and limitations

Some of the results obtained in this research can be linked and compared to the results of similar studies, this is especially true with regard to the sensitivity analysis. First and foremost, LSPIV analyses were performed using imagery collected by a drone in different environments with different seeding conditions. Analogous to other studies (Pumo et al., 2021; Dal Sasso et al., 2020; Meselhe et al., 2004), it was found that the concentration of tracer material on the water surface and the spatial distribution thereof are crucial controls of the LSPIV performance. Based on 15 experimental observations in a laboratory setting, involving a wide range of seeding densities, Meselhe et al. (2004) found that tracers must cover at least 10% to 30% of the water surface to yield LSPIV velocity estimates with the lowest error. Consistent with the findings of Meselhe et al. (2004), this study observed the lowest measurement error for the Dinkel River study area, which exhibited seeding densities of around 10% at the time of the data acquisition campaign. Downstream of the weir in the Meuse River study area, seeding densities of roughly 5% were observed in the region of interest; as expected, the LSPIV analysis revealed the highest measurement error for this study area. The poor LSPIV performance in the case of the Meuse River study area was also attributed to the fact that the surface features were scattered inhomogeneously across the water surface. With this in mind, the more recent works of Dal Sasso et al. (2020) and Pumo et al. (2021) confirm that, next to the seeding density, the spatial distribution of tracers is a critical control of the LSPIV performance as well; they hypothesise that inhomogeneous seeding will reduce velocity samples for large areas on the water surface, likely causing a significant underestimation of the velocity magnitudes. Interestingly enough, evidence from Pumo et al. (2021) showed that tracer scarcity and inhomogeneous seeding might potentially be counterbalanced by using considerably longer image sequence durations. Pumo et al. (2021) assert that by considering longer image sequence durations (of several minutes) in the case of sub-optimal seeding conditions, one may increase the number of surface flow velocity samples in space and, therefore, reduce error. However, one must realise that the time-averaged velocity fields will still include spurious, zero-velocity measurements this way, which will likely lead to an underestimation of the surface flow velocities nonetheless (Pizarro et al., 2020; Dal Sasso et al., 2020); for this reason, Pizarro et al. (2020) and Dal Sasso et al. (2020) do not recommend using a very long image sequence duration as a means to deal with sub-optimal seeding conditions. Instead, Pizarro et al. (2020) and Dal Sasso et al. (2020) propose that one should identify sets of images (or windows) from the image sequence that exhibit the best seeding conditions; these sets of images should then be used as input in the LSPIV analysis instead of the complete image sequence. To be able to identify images with the best seeding conditions, Pizarro et al. (2020) introduced the so-called 'Seeding Distribution Index' (SDI). The reader is referred to Appendix D for more information on the SDI. Dal Sasso et al. (2020) used the SDI to identify the best images to analyse and, subsequently, significantly reduced error (up to 39% error reduction) associated with tracer scarcity and seeding inhomogeneity. This thesis also examined whether the SDI approach could effectively reduce error for images obtained at the Meuse River (Appendix D); similar to Dal Sasso et al. (2020), an error reduction of 35% was achieved.

This thesis also tried to answer the practical question of how long the flowing water should be recorded to obtain reliable LSPIV velocity estimates. However, the sensitivity analysis performed in this study was unable to provide a definitive answer regarding the most appropriate image sequence duration. Instead, it can be concluded that the appropriate sequence duration is highly dependent on the flow conditions and seeding characteristics. In the case of the Dinkel River study area, an image sequence duration of 4 s was found to be sufficient already. In comparison, the location downstream of the weir in the Meuse River study area required a minimum duration of 40 to 60 s. This indicates that poorly seeded flows must be observed for a longer period of time in order to reduce error; this is especially true for low flow conditions. Similarly, there also exists a large disparity in the literature

regarding the image sequence durations used for the LSPIV analysis. To illustrate this, Tauro et al. (2016a) adopted image sequence durations between 0.6 and 2.9 s, while Legleiter & Kinzel (2020) used durations up to 64 s. All in all, the appropriate image sequence duration is highly application-driven and must be chosen with extreme care. One can assess which image sequence duration to adopt for the LSPIV analysis using the methods used in this thesis (e.g., section 3.1.4). In the case of poorly seeded flows and low flow velocities, it may be required that the video is recorded for a longer period of time. However, as mentioned earlier in this subsection, to effectively reduce the error associated with sub-optimal seeding conditions, it is recommended that the LSPIV analysis is performed using segments of the image sequence that exhibit the best seeding conditions.

Another critical consideration in LSPIV is the sampling frequency at which the images are recorded. The sensitivity analysis in this study contributes to a better understanding of the relationship between the sampling frequency, interrogation area size and flow conditions and how it may affect the accuracy of the LSPIV results. In this study, it has been established that the choice of the sampling frequency should be made in relation to the flow conditions; to illustrate this, if high flow velocities are observed, it may be appropriate to select a higher sampling frequency to prevent that advected particles show excessively large displacements between successive images and move beyond the scope of the searching area. Likewise, low flow conditions may require lower sampling frequencies. The interrogation area size must also be proportional to the particle displacements and vice versa, the same reasons mentioned before apply to this as well; for instance, a very small interrogation area size can lead to loss of detected particles between image pairs. Various papers proposed rules of thumb to guide the specification of the sampling frequency. For example, Weitbrecht et al. (2002) suggest that the maximum particle displacement between image pairs must be less than 50% of the interrogation area size in LSPIV analyses. On the other hand, Pumo et al. (2021) argue that the maximum particle displacements between successive images should be less than 15% of the interrogation area size to achieve adequate LSPIV performance. Meselhe et al. (2004) argue, based on experimental observations, that the optimum sampling frequencies should be estimated according to the following relationship: $10\frac{\bar{V}}{\sqrt{A}} \leq SF \leq 20\frac{\bar{V}}{\sqrt{A}}$, where SF is the sampling frequency, $\bar{V}$ whole-field mean velocity magnitude, and A is the interrogation area size. The findings in this study confirm that the empirical rule proposed by Meselhe et al. (2004) may indeed be an effective way of selecting the appropriate sampling frequency; this is especially true for uniform and low flow conditions. However, additional research is required to further establish the validity of these empirical rules.

Whereas the tracers typically used in LSPIV applications are rigid artificial objects, the surface features observed in the Dinkel and Meuse River study areas were continuously clustering, disintegrating and deforming. This phenomenon presented a worrisome problem: the pattern matching technique adopted by the PIV algorithm strongly relies on recognisable patterns between successive images (Raffel et al., 2018), which means that the suitability of naturally occurring surface features was questionable. However, the findings of this research build on the existing evidence (i.e., Veldhuizen, 2021; Koutalakis et al., 2019) that surface patterns comprising foam and air bubbles are particularly suitable for LSPIV implementations. It is presumed that the loss of detected particles caused by deformations and clustering is counterbalanced by a continuous inflow of particles, ensuring that a sufficient number of particles is captured by the PIV algorithm nonetheless.

Remote sensing techniques and LSPIV have demonstrated great potential in measuring surface water flow velocities in large-scale fluvial applications. Some recent achievements showed that such non-intrusive measurement techniques are potentially very valuable for various applications in the Hydraulic Engineering context. For instance, Liu et al. (2021) and Le Coz et al. (2010) claim that (drone-based) LSPIV techniques can overcome the deficiencies of traditional gauging methods. Because of this, they assert that LSPIV is highly suitable for monitoring (urban) flood events; this is especially true because features, such as debris, are commonly omnipresent on the water surface during such events. In contrast to conventional gauging methods, LSPIV methods provide a relatively safe, flexible and practical way of conducting direct measurements during extreme flood conditions due to their non-intrusive nature (Liu et al., 2021). Furthermore, LSPIV methods could even be applied to amateur footage of past flood events; this allows one to reconstruct the dynamics of flood processes in past flood events (Le Boursicaud et al., 2016). The results existing in the literature and the findings of this thesis work corroborate that LSPIV may be a reliable method to monitor flood events and conduct post-flood analyses without the need for artificial seeding.

LSPIV-derived data are also commonly applied to obtain river discharge estimations (Jolley et al., 2021; Aberle et al., 2017). Discharge measurements using LSPIV have been applied many times already in the past two decades (Jolley et al., 2021). Examples of studies that successfully estimated the discharge in natural streams are Ran et al. (2016), Dramais et al. (2011), Harpold et al. (2006), Kim et al. (2008), Le Boursicaud et al. (2016) and Le Coz et al. (2010). The aforementioned authors generally used velocity-area methods, meaning that surface velocities obtained from LSPIV were combined with the channel bathymetry to calculate the discharge.

Ultimately, it can be concluded that LSPIV-derived surface flow velocity measurements are primarily used to better understand flow characteristics in water systems. In the existing literature and case studies (e.g., Strelnikova et al., 2020; Muste et al., 2008; Dermisis & Papanicolaou, 2005), LSPIV results were mainly used to derive spatial and temporal flow characteristics, such as time-averaged velocity fields, surface flow streamlines, and vorticity. This information can be used to develop a better understanding of critical fluvial processes, such as meandering of rivers, the interaction of flows with hydraulic structures, flood propagation, the effect of flow processes on the river ecosystem, (morphological) response of rivers to interventions, etc. (Aberle et al., 2017). For example, Strelnikova et al. (2020) recently investigated the flow conditions near fish passages at a hydroelectric dam using drone-based LSPIV and artificial flow seeding. This was done to assess the passage efficiency and fish attraction reliability of the fishways. The results in this thesis, with reference to the Meuse River study area, demonstrated that flow patterns within and around the entrance of fish passages can be captured relatively well by drone-based LSPIV methods; such results can be used, for example, to assess the fish attraction reliability of the fish passage at the Sambeek lock-weir complex (and other similar locations) under varying flow conditions downstream of the weir. This is true considering the fact that the fish attraction and passage efficiency are highly dependent on the observable flow patterns and velocities (Kranenbarg & Kemper, 2006; Thorncraft & Harris, 2000).

While this thesis has been focusing on the positive aspects of drone-based LSPIV and its capabilities quite a lot, one must also be aware of its limitations and caveats. First and foremost, a fundamental requirement in LSPIV is that high-visibility features must be present on the water surface. Without any seeding, or with insufficient seeding, LSPIV methods are practically worthless. This thesis has made use of natural surface features occurring near hydraulic structures. However, such structures or other obstructions may not be present in many other fluvial environments. Therefore, LSPIV may not be applicable in these environments without artificial seeding. Furthermore, careful planning of the data acquisition campaign is essential. Conducting fieldwork during adverse weather conditions is not possible, as the quality of the images will likely be degraded due to external environmental effects (e.g., rain, fog, wind effects, glare, and sun glitter). Also, conducting field work near nesting areas of birds may provoke bird attacks on the drone, which could complicate the acquisition of drone imagery. Moreover, field campaigns typically involve the placement of GCPs around the region of interest. However, this may not be practicable in inaccessible areas. It is also worth mentioning that LSPIV implementations require extensive calibration of the image and PIV processing parameters to obtain accurate results, which can be extremely laborious and time-consuming. Finally, despite the efforts of existing literature and this thesis work, there are still no strict guidelines on how to perform LSPIV analyses; with this in mind, LSPIV in its current state still heavily relies on ad hoc, heuristic working principles which undermine the validity, credibility and appeal of this method.

4.3. Research limitations and future research

The research work presented in this thesis encountered various challenges and was subject to several limitations. An important limitation of this research relates to the accuracy assessment. This research compared LSPIV-derived surface water flow velocities to reference measurements obtained from the so-called ‘float method’. The float method is based on a traditional measurement method where floating objects in the water are visually tracked to determine the flow velocity. This method, however, is highly subject to human error (Dobriyal et al., 2017). The accuracy assessment results in this research may therefore provide a distorted image regarding the accuracy of the LSPIV-derived estimates. Furthermore, the measurements are not entirely independent of the measurements obtained from LSPIV, as the two methods may be subject to the same bias. To illustrate this, the features on the water surface may show flow-independent behaviour due to, for example, wind effects; this, in turn, will affect

the velocity estimates of both the float method and LSPIV. In future research, it is recommended that alternative methods are used to obtain reference velocity measurements; this can be done by utilising advanced velocimetry instruments (ADCP, ADV, etc.) or by developing hydrodynamic models. Preferably, multiple validation methods ought to be used concurrently to rigorously test the performance of drone-based LSPIV in unseeded flows.

The second limitation encountered in this research relates to the acquisition of GPS data at the GCPs placed in the field during the data acquisition campaign in the Dinkel River study area. Due to the malfunctioning of the RTK GNSS antenna, the coordinates of the GCPs could not be determined. Instead, a local coordinate system was established by manually measuring the distance between the GCPs. Once again, this approach is prone to human error. This limitation likely affected the LSPIV results in this research. However, it is unknown to what extent the results were affected. This brings us to the next recommendation: in future research, one should assess the sensitivity of LSPIV to different approaches concerning the establishment of coordinates at the GCPs.

Another important limitation of this study is that a one-factor-at-a-time sensitivity analysis was carried out. Even though it provides meaningful insight into how and to what extent single input variables affect the LSPIV results, it does not account for the cooperative effect of the different identified error sources in LSPIV (Saltelli et al., 2006). For example, it was established earlier that selecting the appropriate image sampling frequency depends on the interrogation area size and vice versa. To account for their confounding effect on the LSPIV performance, they should be varied concurrently according to a multivariate sensitivity analysis or even a full uncertainty analysis (if possible) (Saltelli et al., 2006). In future research, alternative approaches should be explored to assess how the different parameters associated with the main identified error sources influence the measurement results.

Finally, the author of this thesis strongly encourages to further build on the work of this research by applying drone-based LSPIV methods in different environments with different seeding and flow conditions to establish the validity of drone-based LSPIV in unseeded flows and LSPIV in general.

5

Conclusion

This chapter outlines the main findings of the work proposed in this thesis, this was done by answering the research questions presented in the introduction:

*I. **How can drone-based LSPIV be utilised to derive surface flow velocity estimates in unseeded flows, and how do the different parameters associated with the main identified error sources influence these measurement results?***

To properly utilise LSPIV to infer surface water flow velocities from remotely-sensed imagery, one must have a thorough understanding of the LSPIV working principle and all the processes involved. Having said that, a detailed workflow was developed to guide the LSPIV implementations. The LSPIV workflow can be characterised by four main stages, including (1) data acquisition and preparatory work; (2) image pre-processing; (3) image evaluation; and (4) post-processing. The first stage involves collecting field data, such as video recordings of the flowing water, GPS data and reference velocity measurements. In the second stage, images obtained from the field campaign ought to be processed through the application of image stabilisation and orthorectification to reduce the effects of image distortions, deformations and instabilities; another key component of the image pre-processing stage is the enhancement of the imagery to improve the detectability and traceability of features on the water surface. Subsequently, the PIV algorithm is applied to the pre-processed imagery to obtain a sequence of vector fields representing the instantaneous surface water flow velocities within the region of interest; time-averaging can then be applied to obtain the mean velocity magnitudes. In the final stage, spurious vectors in the vector field are corrected and further analyses may be performed (e.g., accuracy assessment).

Whereas most existing LSPIV studies heavily relied on using artificial tracers for flow seeding, this research investigated whether applying LSPIV in flows seeded by naturally occurring features is feasible. In this research, drone-borne imaging techniques and the abovestated LSPIV workflow were applied to derive velocity estimates in flows near hydraulic structures. Flows near hydraulic structures were found to fit the focus of this study, as naturally occurring surface features (i.e., foam and air bubbles) tend to be omnipresent on the water surface in such environments. Two study areas were selected at which experimental observations were performed. The first set of experiments occurred downstream of a weir located at the Dinkel River in the Netherlands. The second set of experiments was conducted downstream of a weir and at a fish passage in the Meuse River at a lock-weir complex located near Sambeek, the Netherlands.

For the Dinkel River study area, the LSPIV-derived surface water flow velocities were in relatively good agreement with the reference velocity measurements, with mean absolute velocity deviations in the order of 10^{-2} m/s and normalised root mean squared values ranging between 5% and 9%. In addition, the LSPIV-derived velocity field was able to realistically describe the behaviour of the flow in the Dinkel River.

Downstream of the weir in the Meuse River study area, the LSPIV-derived velocities showed worse agreement with the reference measurements than the Dinkel River case, presumably due to inhomogeneous seeding and tracer scarcity. More specifically, the LSPIV results significantly and systematically underestimated the flow velocities with mean absolute deviations from the reference values in the order

of 10^{-1} m/s and a normalised root mean squared error value of around 35%. Even though the analysis tended to underestimate the flow velocities significantly, it was able to generate a coherent vector field and capture the key elements of the flow; this is especially true for areas within the stream portion of interest that showed higher seeding densities. With this in mind, the LSPIV still provided meaningful insight regarding the flow characteristics downstream of the weir. Furthermore, the analyses for the fish passage also provided promising results; the results strongly suggest that drone-based LSPIV can be successfully applied to visualise the flow patterns and quantify surface flow velocities within fish passages and similar hydraulic structures.

A comprehensive sensitivity analysis was carried out to investigate to what extent the main sources of error associated with data collection and image processing affect the performance of LSPIV implementations. The findings thereof support the conclusions listed below:

- Analysis of the sensitivity of LSPIV to a variable camera tilt angle supports the conclusion that a significant inclination (>45°) of the camera axis with respect to the water surface is likely to be detrimental for the accuracy of the LSPIV velocity estimations. Error associated with image rectification procedures may be minimised by applying orthorectification implicitly rather than explicitly. It is recommended that the camera tilt angle is kept as small as possible.
- Drone-borne imagery was collected at various flight altitudes. The LSPIV analyses performed on these images showed little difference to one another, indicating that the LSPIV accuracy is less likely to be significantly impacted by the drone flight altitude, given that the surface features remain clearly visible in the imagery.
- The duration at which the flow ought to be observed to obtain reliable LSPIV outputs was found to be highly case-specific. For the case of the Dinkel River study area, an image sequence duration of 4 s was found to be sufficient already, while the Meuse River study area required a minimum duration of 40 to 60 s. This confirms that the appropriate image sequence duration must be chosen with extreme care prior to each LSPIV implementation. It is recommended that the video is recorded with a sufficiently long duration, preferably of several minutes. Afterwards, one can assess which duration and sequence of images to adopt for the LSPIV analysis.
- The sensitivity analysis confirms that the sampling frequency at which the imagery is collected should be chosen with extreme care. Essentially, the choice for the sampling frequency should be such that the observed tracer displacements are proportional to the interrogation area size. As a general rule, the sampling frequency should be reduced considerably in the case of low flow conditions to prevent excessively small tracer displacements in successive images.
- The application of image enhancement techniques led to negligible improvement in the LSPIV performance. Some filters even significantly deteriorated the usability of the imagery, negatively affecting the accuracy of the velocity fields. In brief, image enhancement may not be required for environments where the surface features are already clearly distinguishable from the background colour.
- Regarding the interrogation area size, one must ensure that a sufficient number of tracer particles are captured therein. Large tracers may remain unresolved in the LSPIV application when assuming a very small interrogation area size, leading to an unsatisfactory LSPIV performance. Furthermore, the frame-by-frame particle displacements must not exceed the scope of the searching area.
- Finally, it was found that a performance increment can be achieved by carefully reducing the spatial resolution of the imagery; this is especially true for flows with relatively large surface features. A coarser resolution may enhance the detectability and traceability of these large features.

II. To what extent do the quantity and spatial distribution of naturally occurring tracing material constrain the applicability of drone-based LSPIV in unseeded flows?

The different study areas considered in this research allowed for assessing the LSPIV performance under variable seeding conditions. Three different reaches in the Dinkel River, referred to as locations 1, 2 and 3, were considered. The three river reaches differed from one another with respect to the

seeding conditions. More specifically, the naturally occurring surface features observed at location 3 attained a much smaller size on average than those observed at locations 1 and 2. Locations 1 and 2 also showed particularly large spreads in observed tracer sizes; in contrast, the tracers at location 3 had more or less a constant size across the water surface. Furthermore, the Dinkel River study area exhibited overall relatively high seeding densities (ca. 10%) and homogeneity across the water surface. However, it was observed that the spatial distribution of tracer material at location 1 was relatively inhomogeneous compared to locations 2 and 3. The Meuse River study area, on the other hand, showed comparatively worse seeding conditions downstream of the weir. To be more specific, the seeding density for the entire field of view was estimated to be 5%. Additionally, the spatial distribution of the tracer material was highly inhomogeneous. Furthermore, large areas on the water surface did not contain any tracer material at all. Lastly, experimental observations were also conducted at the fish passage located in the Meuse River study area. The fish passage exhibited much higher seeding densities of approximately 17% and adequate seeding homogeneity. With the above information in mind, it was found that the accuracy of the velocity estimations for all three sections at the Dinkel River were quite satisfactory. Interestingly enough, increasingly better LSPIV performance could be observed for the locations further downstream of the weir at the Dinkel River (i.e., locations 2 and 3); it is strongly believed that this is due to the more homogeneous distribution and uniform size of the tracer material. In the case of the Meuse River study area, the velocity field systematically underestimated the flow velocities downstream of the weir; on top of that, large low- and zero-velocity areas could be observed in this velocity field. This confirms that low seeding densities and seeding inhomogeneity are likely to result in a significant underestimation of surface flow velocities. One may reduce error associated with suboptimal seeding conditions by performing the LSPIV analysis on portions of the video that exhibit the best seeding conditions instead of the full video. Finally, the velocity field obtained for the fish passage in the Meuse River study area was much more promising in comparison, which is likely due to the high seeding densities therein.

III. How does drone-based LSPIV perform compared to traditional, fixed camera LSPIV implementations with regard to estimating surface flow velocities?

This research assessed fixed camera LSPIV configurations by comparing surface water flow velocity measurements of fixed camera LSPIV to measurements obtained from drone-based LSPIV. Moreover, the velocity estimations derived from fixed camera LSPIV were compared to independent benchmark surface water flow velocity values obtained from the float method as well. Experimental observations were carried out at locations 2 and 3 in the Dinkel River study area to facilitate this comparison. For the experimental observations conducted with the fixed camera configuration, images were collected from the southernmost river bank with a significant inclination of the camera axis with respect to the water surface (ca. 80°); the drone-borne configuration comprised a drone flight altitude of 40 m and camera tilt angle of 0° with respect to the water surface.

The experimental findings in this thesis revealed that the fixed camera LSPIV implementations could not accurately characterise the flow at the selected stream portions. In contrast, drone-based LSPIV results presented comparatively satisfying performance. The fixed camera LSPIV outputs showed poor agreement with the benchmark velocity measurements. Furthermore, the time-averaged velocity fields of fixed camera LSPIV were observed to be erratic and incoherent across the entire region of interest and, hence, failed to provide any meaningful insight. The resounding failure of fixed camera LSPIV implementations in this study was caused or alleged to be caused by several error sources, with the following being the most important ones: (i) suboptimal illumination conditions on the water surface causing deterioration of the tracer visibility; (ii) wind effects and sun glitter inducing distortions onto the water surface, resulting in flow-independent velocity measurements; and (iii) improper camera positioning and orientation resulting in significant perspective distortions in the imagery. The aforementioned error sources were practically non-issues in the case of drone-based LSPIV in this study; this is true as water surface distortions induced by external environmental factors were negligible and perspective distortions in the imagery were avoided by adopting a nadir camera orientation. A last disadvantage worth mentioning is that a stationary camera captures a smaller field of view compared to a drone, suggesting that fixed camera LSPIV may be less suitable for the application in large-scale water systems.

In conclusion, the significant inclination of the camera axis of the stationary camera setup was found to be detrimental to the measurement accuracy. Therefore, one should refrain from employing the same stationary camera setup used in this research. The findings in this research support and strongly favour the use of drones to estimate surface water flow velocities in large-scale fluvial applications. Suppose one decides to use a stationary camera setup nonetheless. In that case, it is recommended that the imaging system is erected on an elevated area, while keeping the inclination of the camera axis with respect to the water surface as small as possible (<45°); such configuration can be achieved by, for example, installing the fixed camera system on a bridge crossing the stream.

What are the capabilities that drone-borne imaging techniques and LSPIV methods hold for estimating surface flow velocities in unseeded flows within large-scale fluvial applications?

Based on the findings of this research, it can be argued that drone-based LSPIV offers a promising method for capturing the spatial and temporal structure of fluid motions without the need for artificial flow seeding. This study successfully exploited naturally occurring features on the water surface, such as foam and air bubbles, to quantify the surface water flow velocities and describe observable surface flow phenomena near hydraulic structures. The employment of drone technologies was particularly interesting as it allowed for quick, safe and relatively inexpensive field data collection in large-scale fluvial applications. However, one must realise successfully applying LSPIV requires a thorough understanding of its underlying principles and the parameters associated with data collection and image processing. Under the right conditions and by carefully selecting the appropriate experimental configurations and input parameters, accurate surface water flow velocity estimations may be obtained.

References

Aberle, J., Rennie, C. D., Admiraal, D. M., & Muste, M. (2017). *Methods, Instrumentation, Data Processing and Management. Volume II: Instrumentation and Measurement Techniques*, volume 2. CRC Press/Balkema.

Ali, S. (2013). *Flow over Weir-like Obstacles*. Delft University of Technology. https://doi.org/10.4233/uuid:b9c67923-a84a-47b0-8c0f-6d873ffd1d85

Bandini, F., Lüthi, B., Peña-Haro, S., Borst, C., Liu, J., Karagkiolidou, S., Hu, X., Lemaire, G. G., Bjerg, P. L., & Bauer-Gottwein, P. (2021). A Drone-Borne Method to Jointly Estimate Discharge and Manning's Roughness of Natural Streams. *Water Resources Research*, 57(2). https://doi.org/10.1029/2020WR028266

Breukel, R., Silva, W., Van Vuuren, W., Botterweg, J., & Venema, R. (1992). De Maas: Verleden, heden en toekomst. Technical report, Rijkswaterstaat, Lelystad. https://edepot.wur.nl/384762

Chanson, H. (2007). Bubbly flow structure in hydraulic jump. *European Journal of Mechanics - B/Fluids*, 26(3), 367–384. https://doi.org/10.1016/j.euromechflu.2006.08.001

Clasing, R. & Muñoz, E. (2018). Estimating the Optimal Velocity Measurement Time in Rivers' Flow Measurements: An Uncertainty Approach. *Water*, 10(8), 1010. https://doi.org/10.3390/w10081010

Cotton, J. A., Wharton, G., Bass, J. A., Heppell, C. M., & Wotton, R. S. (2006). The effects of seasonal changes to in-stream vegetation cover on patterns of flow and accumulation of sediment. *Geomorphology*, 77(3-4), 320–334. https://doi.org/10.1016/J.GEOMORPH.2006.01.010

Dal Sasso, S. F., Pizarro, A., & Manfreda, S. (2020). Metrics for the Quantification of Seeding Characteristics to Enhance Image Velocimetry Performance in Rivers. *Remote Sensing*, 12(11), 1789. https://doi.org/10.3390/RS12111789)

De Oliveira, E., Tetard, S., & Benammar, I. (2020). Downstream fish migration along the low Meuse River ACTION A.1: Definitions and nomenclature. Technical report. https://www.researchgate.net/publication/344774537

Dermisis, D. C. & Papanicolaou, A. N. T. (2005). Determining the 2-D Surface Velocity Field around Hydraulic Structures with the Use of a Large Scale Particle Image Velocimetry (LSPIV) Technique. *Impacts of Global Climate Change*, 1–12. https://doi.org/10.1061/40792(173)404

D'Errico, J. (2022). *inpaint_nans*. https://www.mathworks.com/matlabcentral/fileexchange/4551-inpaint_nans

Detert, M. (2021). How to Avoid and Correct Biased Riverine Surface Image Velocimetry. *Water Resources Research*, 57(2). https://doi.org/10.1029/2020WR027833

Dobriyal, P., Badola, R., Tuboi, C., & Hussain, S. A. (2017). A review of methods for monitoring streamflow for sustainable water resource management. *Applied Water Science*, 7(6), 2617–2628. https://doi.org/10.1007/s13201-016-0488-y

Dramais, G., Le Coz, J., Camenen, B., & Hauet, A. (2011). Advantages of a mobile LSPIV method for measuring flood discharges and improving stage–discharge curves. *Journal of Hydro-environment Research*, 5(4), 301–312. https://doi.org/10.1016/j.jher.2010.12.005

Fox, R. W., McDonald, A. T., Pritchard, P. J., Mitchell, J. W., & Leylegian, J. C. (2016). *Fluid Mechanics* (9 ed.). John Wiley & Sons.

Fujita, I. & Komura, S. (1994). Application of Video Image Analysis for Measurements of River-Surface Flows. *Physics, Environmental Science, Engineering*, 38, 733–738. https://doi.org/10.2208/prohe.38.733

Fujita, I., Muste, M., & Kruger, A. (1998). Large-scale particle image velocimetry for flow analysis in hydraulic engineering applications. *Journal of Hydraulic Research*, 36(3), 397–414. https://doi.org/10.1080/00221689809498626

Guan, D., Melville, B. W., & Friedrich, H. (2014). Flow Patterns and Turbulence Structures in a Scour Hole Downstream of a Submerged Weir. *Journal of Hydraulic Engineering*, 140(1), 68–76. https://doi.org/10.1061/(ASCE)HY.1943-7900.0000803

Harpold, A. A., Mostaghimi, S., Vlachos, P. P., Brannan, K., & Dillaha, T. (2006). Stream Discharge Measurement Using a Large-Scale Particle Image Velocimetry (LSPIV) Prototype. *Transactions of the ASABE*, 49(6), 1791–1805. https://doi.org/10.13031/2013.22300

Hauet, A., Creutin, J.-D., & Belleudy, P. (2008a). Sensitivity study of large-scale particle image velocimetry measurement of river discharge using numerical simulation. *Journal of Hydrology*, 349(1-2), 178–190. https://doi.org/10.1016/j.jhydrol.2007.10.062

Hauet, A., Kruger, A., Krajewski, W. F., Bradley, A., Muste, M., Creutin, J.-D., & Wilson, M. (2008b). Experimental System for Real-Time Discharge Estimation Using an Image-Based Method. *Journal of Hydrologic Engineering*, 13(2), 105–110. https://doi.org/10.1061/(ASCE)1084-0699(2008)13:2(105)

Higham, J. & Brevis, W. (2019). When, what and how image transformation techniques should be used to reduce error in Particle Image Velocimetry data? *Flow Measurement and Instrumentation*, 66, 79–85. https://doi.org/10.1016/j.flowmeasinst.2019.02.005

Hilgersom, K. P. & Luxemburg, W. M. J. (2012). Technical Note: How image processing facilitates the rising bubble technique for discharge measurement. *Hydrology and Earth System Sciences*, 16(2), 345–356. https://doi.org/10.5194/hess-16-345-2012

Jolley, M. J., Russell, A. J., Quinn, P. F., & Perks, M. T. (2021). Considerations When Applying Large-Scale PIV and PTV for Determining River Flow Velocity. *Frontiers in Water*, 3. https://doi.org/10.3389/frwa.2021.709269

Kabo-bah, A. (2010). *Developing water quality modelling scheme in ILWIS Open for the Dinkel River in support of climate change and adaptation studies.* International Institute for Geo-Information Science and Earth Observation. https://webapps.itc.utwente.nl/librarywww/papers_2010/msc/wrem/kabobah.pdf

Kim, Y. (2006). *Uncertainty analysis for non-intrusive measurement of river discharge using image velocimetry.* The University of Iowa.

Kim, Y., Muste, M., Hauet, A., Krajewski, W. F., Kruger, A., & Bradley, A. (2008). Stream discharge using mobile large-scale particle image velocimetry: A proof of concept. *Water Resources Research*, 44(9). https://doi.org/10.1029/2006WR005441

Kitsikoudis, V., Becker, B. P., Huismans, Y., Archambeau, P., Erpicum, S., Pirotton, M., & Dewals, B. (2020). Discrepancies in Flood Modelling Approaches in Transboundary River Systems: Legacy of the Past or Well-grounded Choices? *Water Resources Management*, 34(11), 3465–3478. https://doi.org/10.1007/S11269-020-02621-5

KNMI (2022). *Daggegevens van het weer in Nederland*. https://www.knmi.nl/nederland-nu/klimatologie/daggegevens

Koutalakis, P., Tzoraki, O., & Zaimes, G. (2019). UAVs for Hydrologic Scopes: Application of a Low-Cost UAV to Estimate Surface Water Velocity by Using Three Different Image-Based Methods. *Drones 2019, Vol. 3, Page 14*, 3(1), 14. https://doi.org/10.3390/DRONES3010014

Kranenbarg, J. & Kemper, J. (2006). Efficiëntere vismigratie bij vistrappen en kunstwerken: onderzoek op vismigratie gericht stuwbeheer in de Maas bij Sambeek. Technical report, Delft Hydraulics, Delft. http://resolver.tudelft.nl/uuid:d9c37b64-0b0c-4135-acfb-002a503920ff

Lanters, R. (1995). Vismigratie door de bekkenvistrappen Lith en Belfeld in de Maas. Technical report, Rijksinstituut voor Visserijonderzoek (RIVO-DLO), Ijmuiden. https://edepot.wur.nl/323349

Le Boursicaud, R., Pénard, L., Hauet, A., Thollet, F., & Le Coz, J. (2016). Gauging extreme floods on YouTube: application of LSPIV to home movies for the post-event determination of stream discharges. *Hydrological Processes*, 30(1), 90–105. https://doi.org/10.1002/hyp.10532

Le Coz, J., Hauet, A., Pierrefeu, G., Dramais, G., & Camenen, B. (2010). Performance of image-based velocimetry (LSPIV) applied to flash-flood discharge measurements in Mediterranean rivers. *Journal of Hydrology*, 394(1-2), 42–52. https://doi.org/10.1016/J.JHYDROL.2010.05.049

Legleiter, C. J. & Kinzel, P. J. (2020). Inferring Surface Flow Velocities in Sediment-Laden Alaskan Rivers from Optical Image Sequences Acquired from a Helicopter. *Remote Sensing*, 12(8), 1282. https://doi.org/10.3390/rs12081282

Liu, W.-C., Lu, C.-H., & Huang, W.-C. (2021). Large-Scale Particle Image Velocimetry to Measure Streamflow from Videos Recorded from Unmanned Aerial Vehicle and Fixed Imaging System. *Remote Sensing*, 13(14), 2661. https://doi.org/10.3390/rs13142661

Meselhe, E. A., Peeva, T., & Muste, M. (2004). Large Scale Particle Image Velocimetry for Low Velocity and Shallow Water Flows. *Journal of Hydraulic Engineering*, 130(9), 937–940. https://doi.org/10.1061/(ASCE)0733-9429(2004)130:9(937)

Muste, M., Fujita, I., & Hauet, A. (2008). Large-scale particle image velocimetry for measurements in riverine environments. *Water Resources Research*, 44(4), 0–19. https://doi.org/10.1029/2008WR006950

Patalano, A., García, C. M., & Rodríguez, A. (2017). Rectification of Image Velocity Results (RIVeR): A simple and user-friendly toolbox for large scale water surface Particle Image Velocimetry (PIV) and Particle Tracking Velocimetry (PTV). *Computers and Geosciences*, 109, 323–330. https://doi.org/10.1016/J.CAGEO.2017.07.009

Peña-haro, S., Lüthi, B., Lukes, R., & Carrel, M. (2020). Wind Effect on ImageBased River Surface Velocity Measurements. *EGU General Assembly 2020*. https://doi.org/https://doi.org/10.5194/egusphere-egu2020-9943

Perks, M. T., Fortunato, S., Sasso, D., Hauet, A., Le Coz, J., Pearce, S., Peña-Haro, S., Tauro, F., Grimaldi, S., Hortobágyi, B., Jodeau, M., Maddock, I., Pénard, L., & Manfreda, S. (2019). Towards harmonization of image velocimetry techniques for river surface velocity observations. *Earth System Science Data*. https://doi.org/10.4121/uuid

Pizarro, A., Dal Sasso, S. F., Perks, M., & Manfreda, S. (2020). Spatial distribution of tracers for optical sensing of stream surface flow. *Hydrology and Earth System Sciences*. https://doi.org/10.5194/hess-2020-188

Pumo, D., Alongi, F., Ciraolo, G., & Noto, L. (2021). Optical Methods for River Monitoring: A Simulation-Based Approach to Explore Optimal Experimental Setup for LSPIV. *Water*, 13(3), 247. https://doi.org/10.3390/w13030247

Raffel, M., Willert, C. E., Scarano, F., Kähler, C. J., Wereley, S. T., & Kompenhans, J. (2018). *Particle Image Velocimetry* (3 ed.), volume 1. Springer International Publishing. https://doi.org/10.1007/978-3-319-68852-7

Ran, Q.-h., Li, W., Liao, Q., Tang, H.-l., & Wang, M.-y. (2016). Application of an automated LSPIV system in a mountainous stream for continuous flood flow measurements. *Hydrological Processes*, 30(17), 3014–3029. https://doi.org/10.1002/hyp.10836

Rhee, D. S., Kim, Y. D., Kang, B., & Kim, D. (2018). Applications of unmanned aerial vehicles in fluvial remote sensing: An overview of recent achievements. *KSCE Journal of Civil Engineering*, 22(2), 588–602. https://doi.org/10.1007/s12205-017-1862-5

Rijkswaterstaat (2014a). *Legger Rijkswaterstaatswerken Waterwet: Stuw Sambeek Poiree*. https://www.rijkswaterstaat.nl/rws/legger/leggerrw_2_0/dwarsprofielen/46D-350-04.html

Rijkswaterstaat (2014b). *Legger Rijkswaterstaatswerken Waterwet: Stuw Sambeek Stoney*. https://www.rijkswaterstaat.nl/rws/legger/leggerrw_2_0/dwarsprofielen/46D-350-04_1.html

Rijkswaterstaat (2022). *Rijkswaterstaat Waterinfo*. https://waterinfo.rws.nl/#!/kaart/waterafvoer/

RIVeR (2020). Rectification of Image Velocity Results (RIVeR) - User Manual. Technical report.

Robert, A. (2003). *River Processes: An Introduction to Fluvial Dynamics*, volume 2. Routledge.

Saltelli, A., Ratto, M., Tarantola, S., & Campolongo, F. (2006). Sensitivity analysis practices: Strategies for model-based inference. *Reliability Engineering & System Safety*, 91(10-11), 1109–1125. https://doi.org/10.1016/j.ress.2005.11.014

Schneider, C. A., Rasband, W. S., & Eliceiri, K. W. (2012). NIH Image to ImageJ: 25 years of image analysis. *Nature Methods 2012 9:7*, 9(7), 671–675. https://doi.org/10.1038/nmeth.2089

Sciacchitano, A. (2019). Uncertainty quantification in particle image velocimetry Topical Review. *Measurement Science and Technology*, 30(9), 1–31. https://doi.org/10.1088/1361-6501/ab1db8

Sharif, O. (2022). Measuring surface water flow velocities by a drone and large-scale particle image velocimetry (LSPIV): Literature Report Preparation Master Thesis. Technical report, University of Twente, Enschede.

Strelnikova, D., Paulus, G., Käfer, S., Anders, K.-H., Mayr, P., Mader, H., Scherling, U., & Schneeberger, R. (2020). Drone-Based Optical Measurements of Heterogeneous Surface Velocity Fields around Fish Passages at Hydropower Dams. *Remote Sensing*, 12(3), 384. https://doi.org/10.3390/rs12030384

Sutarto, T. E. (2015). Application of Large Scale Particle Image Velocimetry (LSPIV) to Identify Flow Pattern in a Channel. *Procedia Engineering*, 125, 213–219. https://doi.org/10.1016/j.proeng.2015.11.031

Talstra, H. (2011). *Large-scale turbulence structures in shallow separating flows*. Delft University of Technology. http://resolver.tudelft.nl/uuid:922e297b-19b9-4399-808d-23e837401a52

Tareen, S. A. K. & Saleem, Z. (2018). A comparative analysis of SIFT, SURF, KAZE, AKAZE, ORB, and BRISK. *2018 International Conference on Computing, Mathematics and Engineering Technologies (iCoMET)*, 1–10. https://doi.org/10.1109/ICOMET.2018.8346440

Tauro, F., Petroselli, A., & Arcangeletti, E. (2016a). Assessment of drone-based surface flow observations. *Hydrological Processes*, 30(7), 1114–1130. https://doi.org/10.1002/hyp.10698

Tauro, F., Porfiri, M., & Grimaldi, S. (2016b). Surface flow measurements from drones. *Journal of Hydrology*, 540, 240–245. https://doi.org/10.1016/J.JHYDROL.2016.06.012

Thielicke, W. & Stamhuis, E. J. (2014). PIVlab – Towards User-friendly, Affordable and Accurate Digital Particle Image Velocimetry in MATLAB. *Journal of Open Research Software*, 2. https://doi.org/10.5334/jors.bl

Thorncraft, G. & Harris, J. H. (2000). Fish Passage and Fishways in New South Wales: A Status Report. Technical report, Cooperative Research Centre for Freshwater Ecology, Sydney.

Van Prooijen, B. (2004). *Shallow Mixing Layers*. Delft University of Technology. http://resolver.tudelft.nl/uuid:8eec05c0-73cf-4284-9439-c0246cddf160

Veldhuizen, R. (2021). *Development of remotely sensed image velocimetry for large-scale free surface flows: Application to the flow through the Eastern Scheldt storm surge barrier*. Delft University of Technology. https://repository.tudelft.nl/islandora/object/uuid:3639e4a1-61f3-41a2-aa16-1270ef8453b2/datastream/OBJ/download

Weitbrecht, V., Kühn, G., & Jirka, G. H. (2002). Large scale PIV-measurements at the surface of shallow water flows. *Flow Measurement and Instrumentation*, 13(5-6), 237–245. https://doi.org/10.1016/S0955-5986(02)00059-6

Yin, Z. (2010). *Hydrological transport model calibration and integration by GUI in 52° North/ILWIS OS for the Dinkel River for supporting water quality studies*. University of Twente. https://webapps.itc.utwente.nl/librarywww/papers_2010/msc/wrem/yin.pdf

A

Appendix A: Supplementary figures data acquisition campaign Dinkel River

(a) (b)

Figure A.1: Impression location 1 of Dinkel River study area: (a) view of weir from northernmost riverbank; (b) view of river from the top of the weir. Photographs taken on 11-04-2022.

(a) (b)

Figure A.2: Impression location 2 of Dinkel River study area: (a) view of river from southernmost riverbank; (b) positioning and orientation of stationary camera at location 2. Photographs taken on 11-04-2022.

(a) (b)

Figure A.3: Impression location 3 of Dinkel River study area: (a) view of river from southernmost riverbank; (b) positioning and orientation of stationary camera at location 3. Photographs taken on 11-04-2022.

Figure A.4: View of location 1 Dinkel River from the top of the weir during low flow conditions. Photograph taken on 19-07-2022.

B

Appendix B: Supplementary material Dinkel River results

B.1. Additional figures accuracy assessment

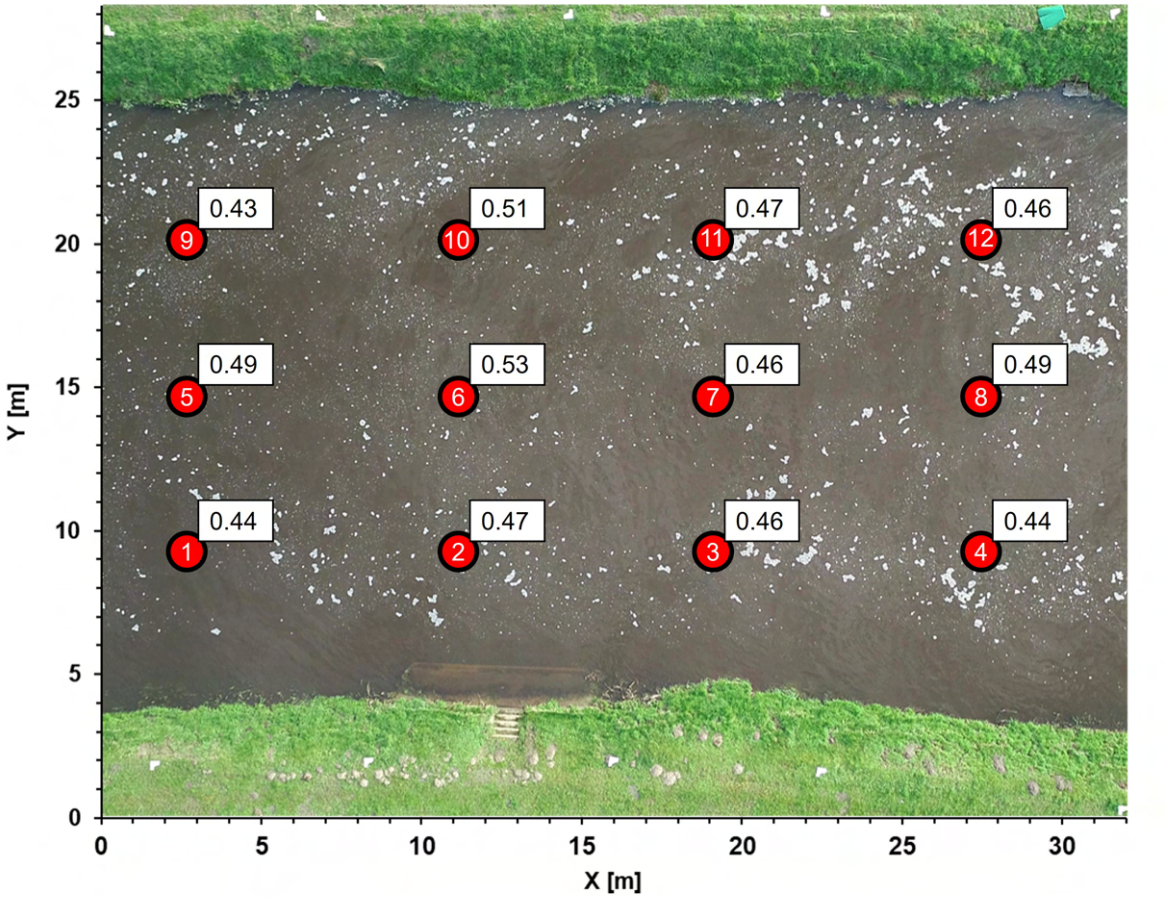

Figure B.1: Reference measurement points with surface water flow velocity magnitudes (m/s) at location 2 Dinkel River.

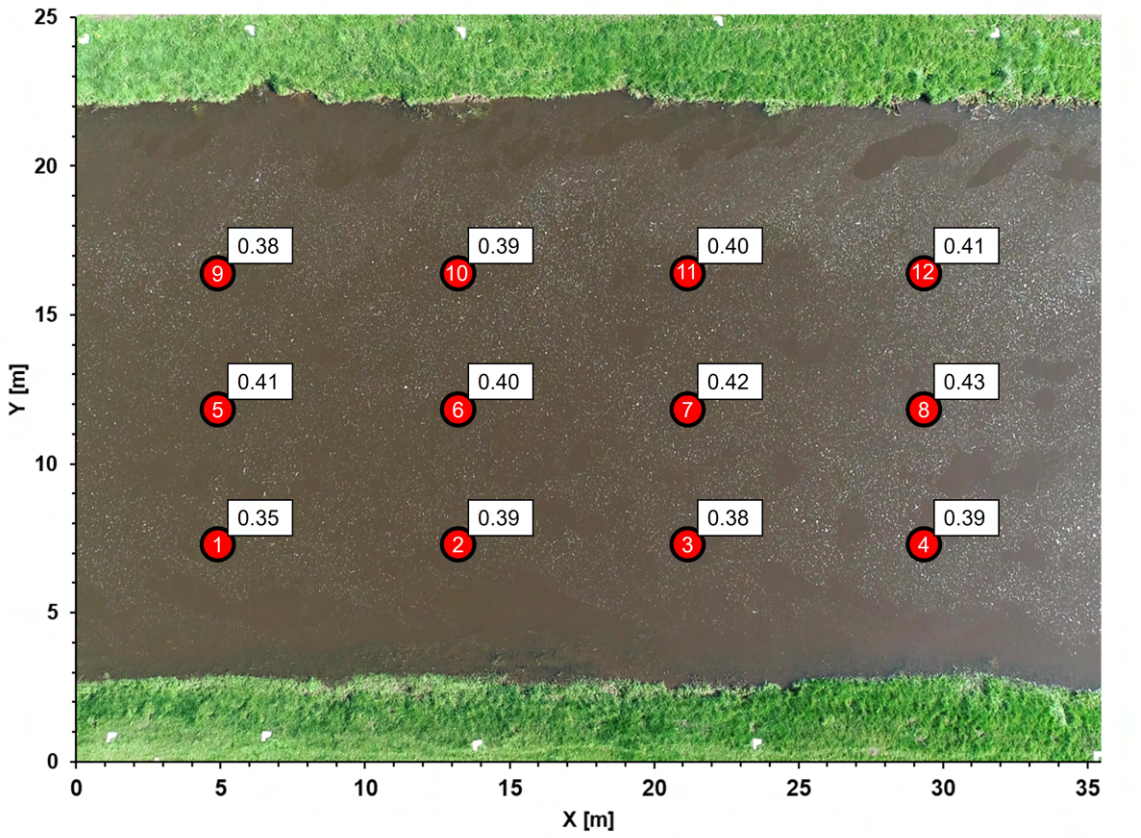

Figure B.2: Reference measurement points with surface water flow velocity magnitudes (m/s) at location 3 Dinkel River.

B.2. Additional figures LSPIV analysis

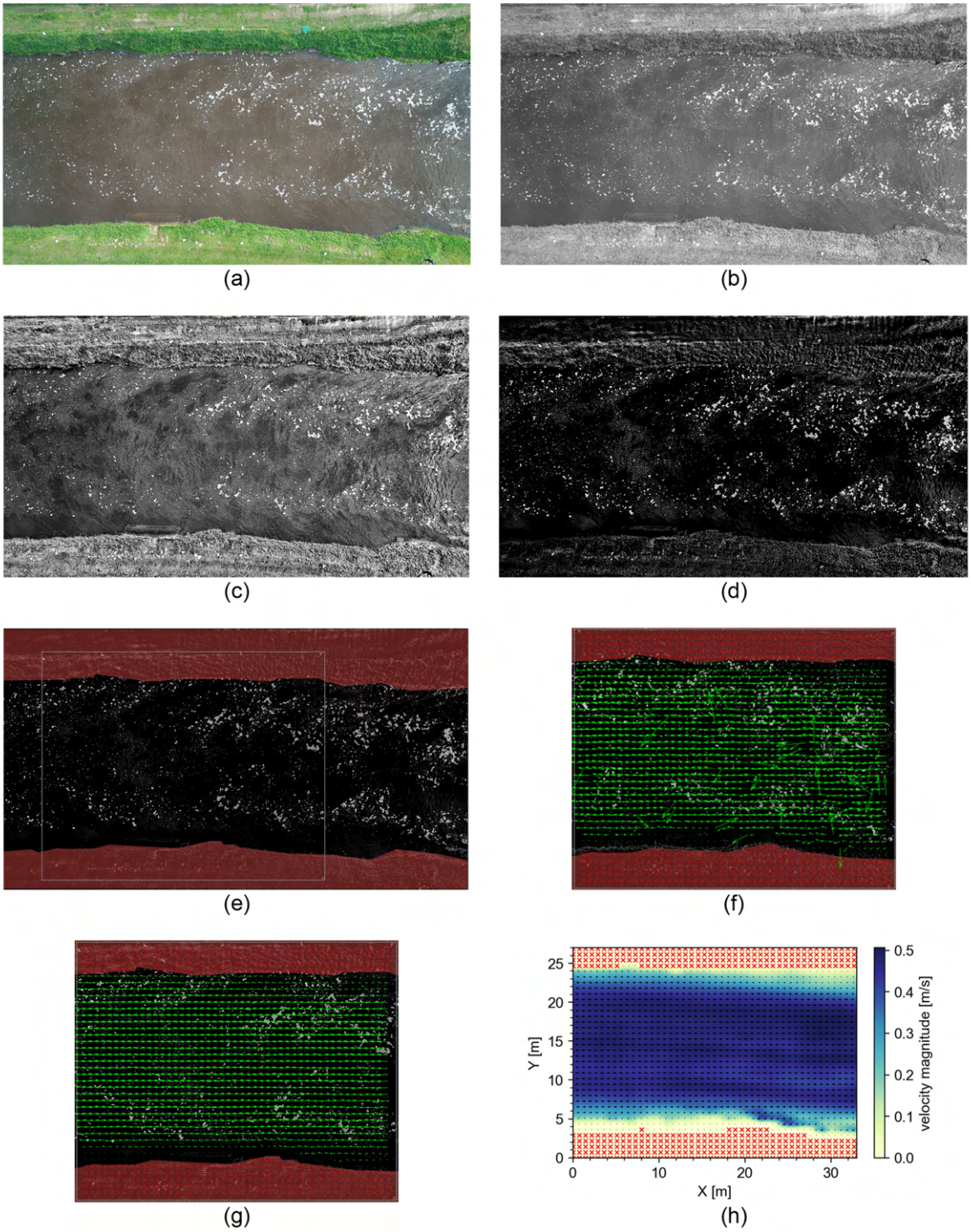

Figure B.3: Sequence of steps in LSPIV to obtain a time-averaged velocity field of location 2 at the Dinkel River: (a) snapshot of raw video recording acquired by drone (40 m & 0°); (b) converting the image sequence to greyscale; (c) applying CLAHE filter to image sequence; (d) subtracting image background from image sequence; (e) applying masks to river banks and defining region of interest; (f) random extract from sequence of instantaneous vector fields within region of interest; (g) time-averaged vector field; (h) final product.

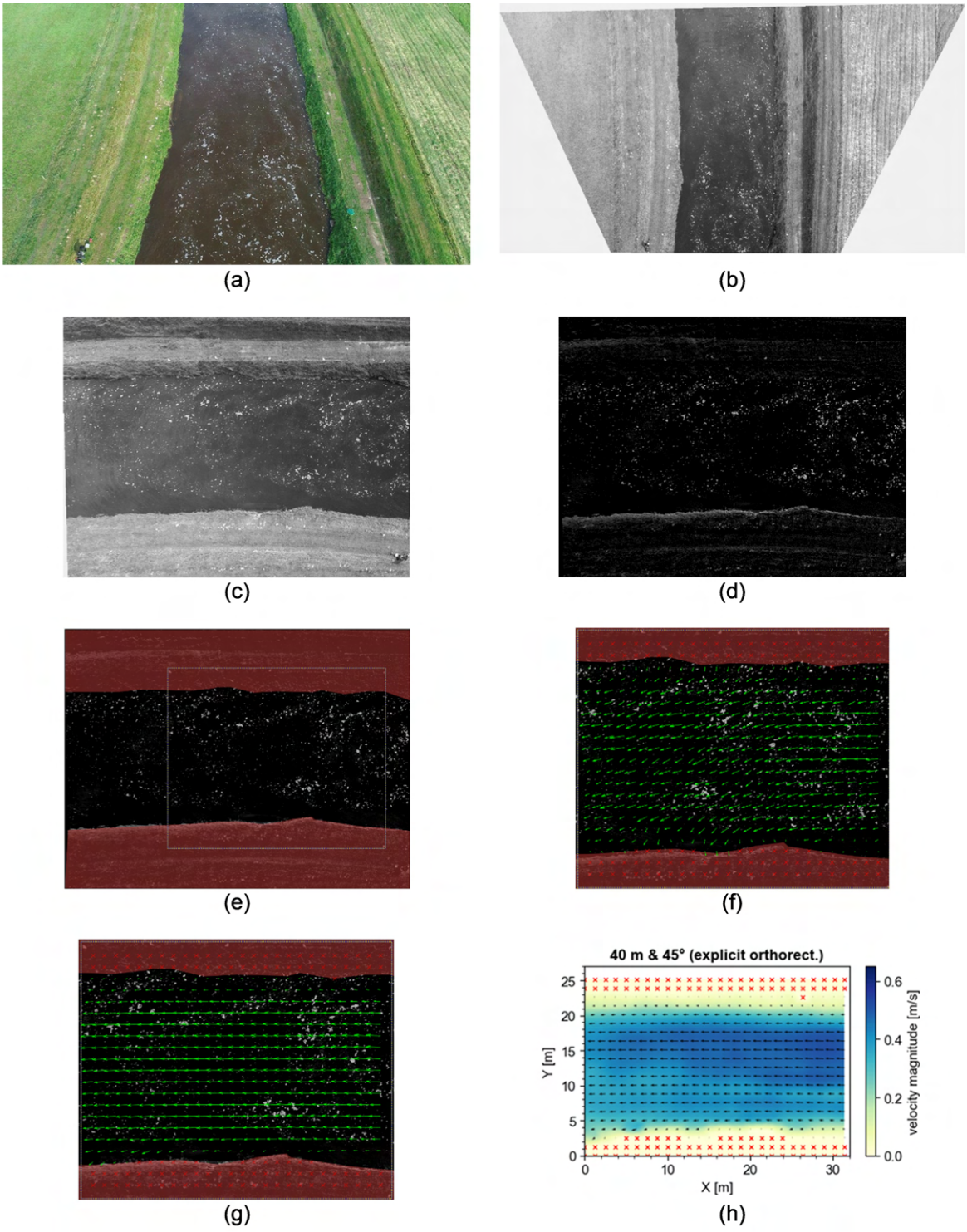

Figure B.4: Sequence of steps in LSPIV involving explicit orthorectification to obtain a time-averaged velocity field from tilted imagery for location 2 of the Dinkel River: (a) snapshot of raw video recording acquired by drone (40 m & 45°); (b) applying explicit orthorectification and converting the image sequence to greyscale; (c) cropping and rotating rectified image sequence; (d) applying CLAHE and subtracting image background from image sequence; (e) applying masks to river banks and defining region of interest; (f) random extract from sequence of instantaneous vector fields within region of interest; (g) time-averaged vector field; (h) final product.

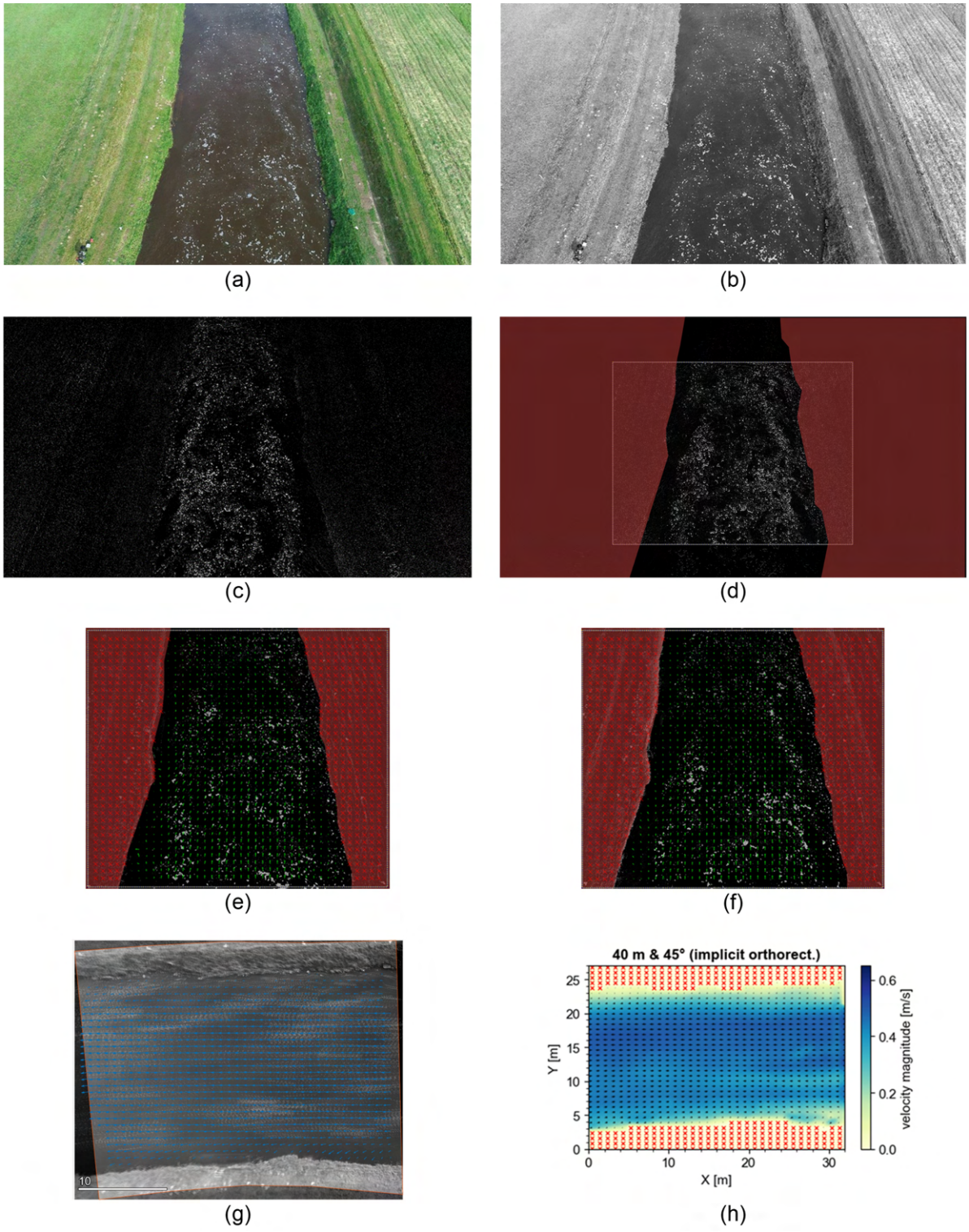

Figure B.5: Sequence of steps in LSPIV involving implicit orthorectification to obtain a time-averaged velocity field from tilted imagery for location 2 of the Dinkel River: (a) snapshot of raw video recording acquired by drone (40 m & 45°); (b) converting the image sequence to greyscale; (c) applying CLAHE filter and subtracting image background from image sequence; (d) applying masks to river banks and defining region of interest; (e) random extract from sequence of instantaneous vector fields within region of interest; (f) time-averaged vector field; (g) applying implicit orthorectification to time-averaged vector field and rotating the vector field; (h) final product.

B.3. Additional figures sensitivity analysis

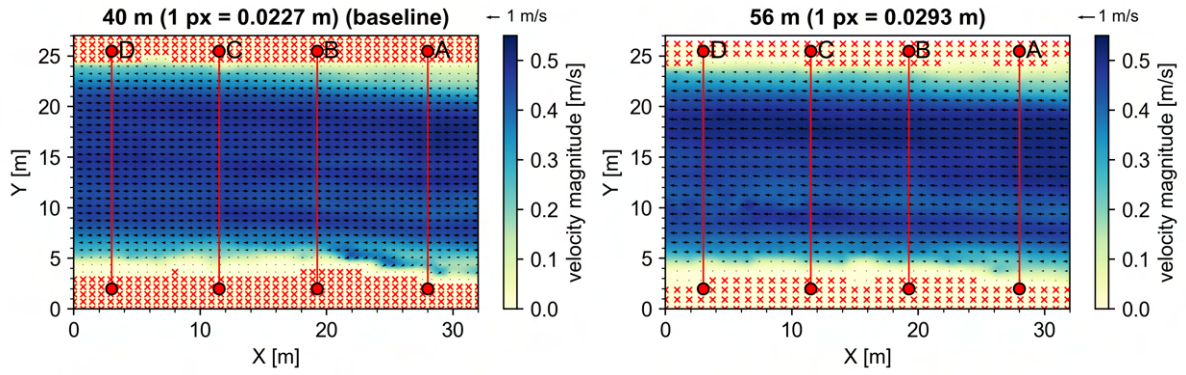

Figure B.6: Visual comparison of time-averaged surface water flow velocity fields computed with imagery obtained at drone flight altitudes of 40 and 56 m. Imagery was acquired from a drone at location 2 in the Dinkel River study area.

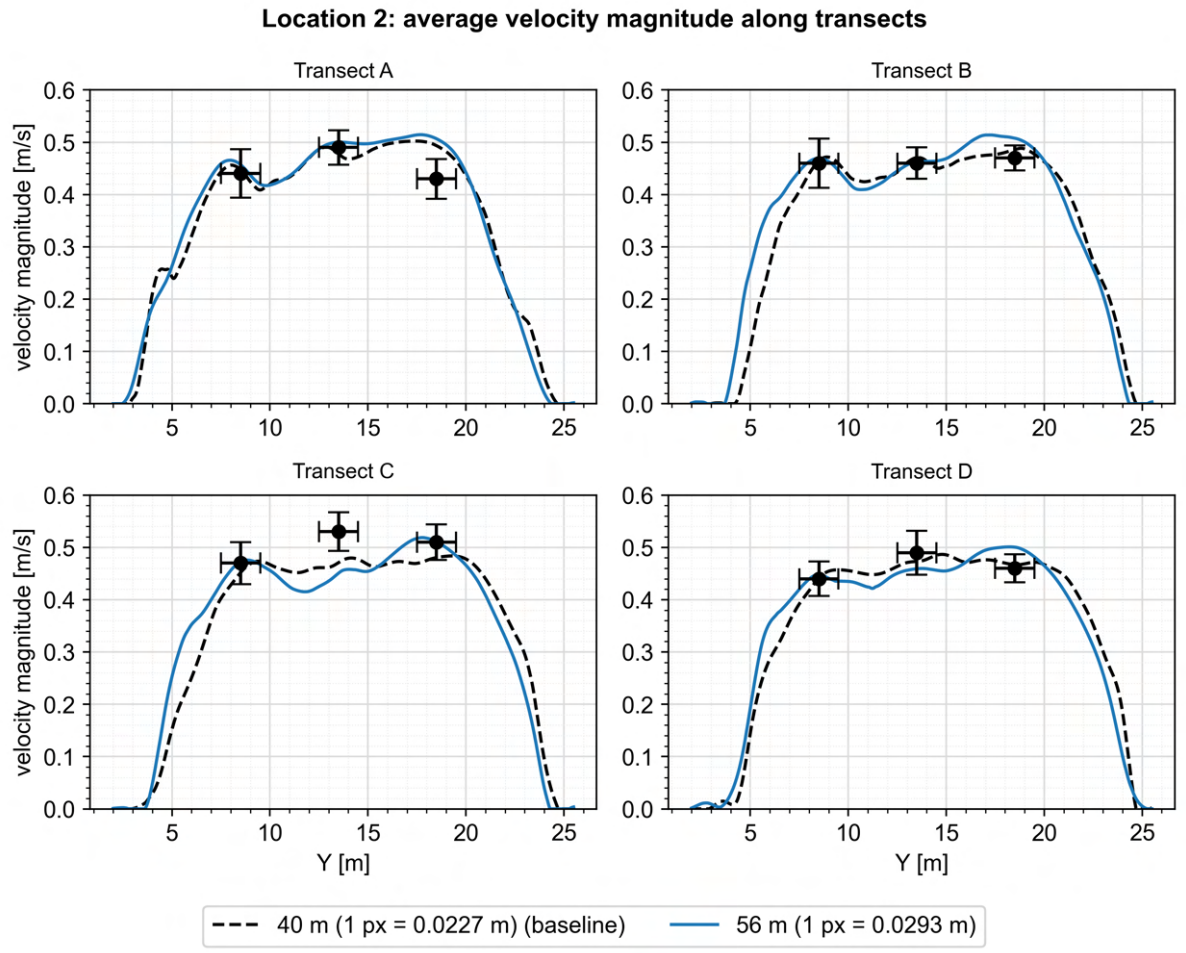

Figure B.7: Velocity profiles extracted from the transects defined in Figure B.6 for drone flight altitudes of 40 and 56 m. Markers represent mean surface water velocity magnitudes obtained from the float method. Uncertainty intervals surrounding the markers represent the standard deviation.

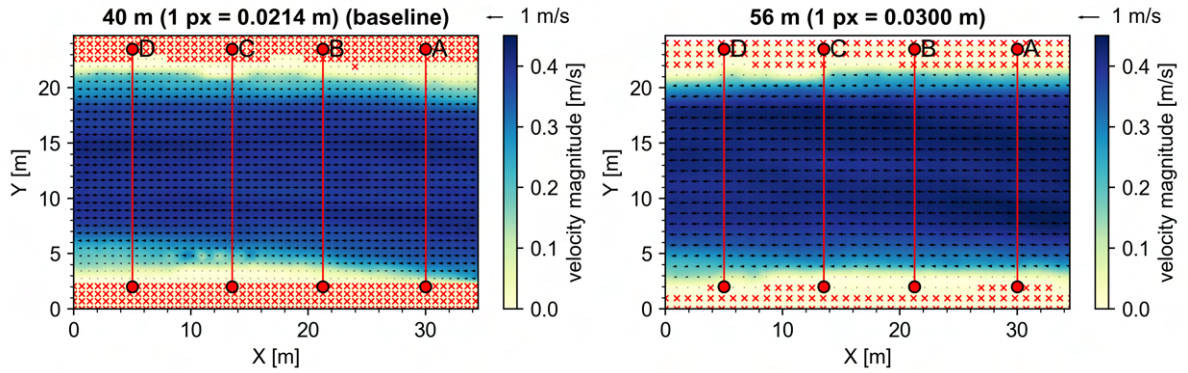

Figure B.8: Visual comparison of time-averaged surface water flow velocity fields computed with imagery obtained at drone flight altitudes of 40 and 56 m. Imagery was acquired from a drone at location 3 in the Dinkel River study area.

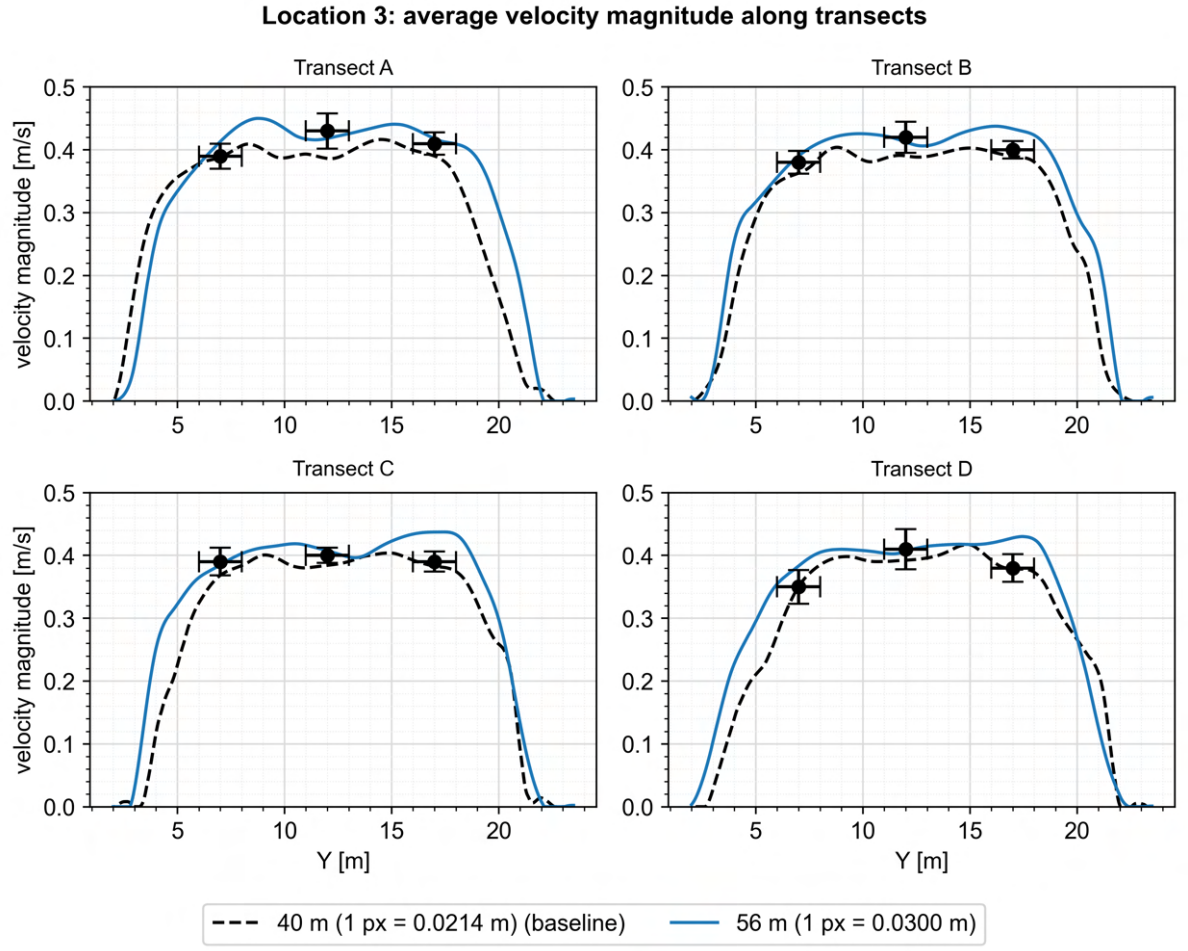

Figure B.9: Velocity profiles extracted from the transects defined in Figure B.8 for drone flight altitudes of 40 and 56 m. Markers represent mean surface water velocity magnitudes obtained from the float method. Uncertainty intervals surrounding the markers represent the standard deviation.

B.4. Additional statistics sensitivity analysis

Table B.1: Complete overview of error metrics obtained from the image (pre-)processing sensitivity analysis of location 1 in the Dinkel River study area. Various error metrics are presented for each case (C1, C2, ...) considered in the sensitivity analysis, see section 2.4.2 for a detailed description of each case. RMSE = root mean squared error; MBE = mean bias error; RMSE and MBE were normalised by the mean velocity magnitude obtained from the float method (0.47 m/s). The color shades represent the relative performance. The green shades indicate relatively good performance, while red indicates relatively poor performance.

Case	Pixel size [m]	Vector spacing [m]	RMSE [m/s]	MBE [m/s]	NRMSE [m/s]	NMBE [%]	Difference RMSE w.r.t baseline [%]
C1 (baseline)	0.0207	0.665	0.041	0.023	8.8	4.9	-
C2	0.0207	0.665	0.071	0.063	15.3	13.5	73.2
C3	0.0207	0.665	0.044	0.030	9.4	6.5	6.9
C4	0.0207	0.665	0.038	0.017	8.1	3.7	-7.6
C5	0.0207	0.665	0.048	0.028	10.4	6.0	18.0
C6	0.0414	1.329	0.035	0.018	7.4	3.8	-15.6
C7	0.0273	0.877	0.036	0.022	7.8	4.7	-11.2
C8	0.0138	0.443	0.051	0.029	10.9	6.3	23.5
C9	0.1035	3.326	0.038	-0.003	8.1	-0.6	-7.8
C10	0.0828	2.661	0.032	0.004	6.8	0.9	-22.9
C11	0.0414	1.330	0.029	0.009	6.3	2.0	-28.9
C12	0.0104	0.333	0.057	0.042	12.2	9.0	38.8
C13	0.0052	0.166	0.089	0.079	19.1	17.0	116.3
C14	0.0207	0.665	0.042	0.021	9.1	4.5	2.9
C15	0.0207	0.665	0.041	0.019	8.8	4.1	-0.8
C16	0.0207	0.665	0.046	0.028	10.0	6.0	13.3
C17	0.0207	0.665	0.046	0.028	10.0	6.1	13.4
C18	0.0207	0.665	0.060	0.048	12.9	10.2	45.9
C19	0.0207	0.665	0.058	0.046	12.5	10.0	42.1
C20	0.0207	0.665	0.044	0.024	9.5	5.1	7.5
C21	0.0207	0.665	0.047	0.032	10.1	6.8	14.2
C22	0.0207	0.665	0.066	0.053	14.2	11.5	60.8
C23	0.0207	0.665	0.049	0.035	10.5	7.6	18.8
C24	0.0207	0.665	0.046	0.026	9.8	5.6	11.6

Table B.2: Complete overview of error metrics obtained from the image (pre-)processing sensitivity analysis of location 2 in the Dinkel River study area. Various error metrics are presented for each case (C1, C2, ...) considered in the sensitivity analysis, see section 2.4.2 for a detailed description of each case. RMSE = root mean squared error; MBE = mean bias error; RMSE and MBE were normalised by the mean velocity magnitude obtained from the float method (0.39 m/s).

Case	Pixel size [m]	Vector spacing [m]	RMSE [m/s]	MBE [m/s]	NRMSE [m/s]	NMBE [%]	Difference RMSE w.r.t baseline [%]
C1 (baseline)	0.0227	0.726	0.028	0.002	6.1	0.4	-
C2	0.0227	0.726	0.044	0.034	9.4	7.3	54.8
C3	0.0227	0.726	0.030	0.007	6.3	1.4	4.4
C4	0.0227	0.726	0.030	-0.002	6.3	-0.5	4.1
C5	0.0227	0.726	0.030	-0.006	6.5	-1.3	6.9
C6	0.0455	1.454	0.026	0.006	5.5	1.4	-9.2
C7	0.0304	0.972	0.028	-0.005	6.0	-1.1	-0.5
C8	0.0151	0.484	0.029	0.002	6.1	0.3	0.5
C9	0.1136	3.632	0.029	0.009	6.1	2.0	0.7
C10	0.0909	2.906	0.029	0.011	6.1	2.3	1.6
C11	0.0454	1.453	0.027	0.002	5.7	0.3	-5.2
C12	0.0114	0.363	0.033	0.013	7.0	2.8	14.9
C13	0.0057	0.182	0.060	0.045	12.8	9.6	111.6
C14	0.0227	0.726	0.029	0.001	6.2	0.1	2.8
C15	0.0227	0.726	0.030	0.001	6.3	0.1	3.7
C16	0.0227	0.726	0.028	-0.0002	6.0	-0.1	-0.5
C17	0.0227	0.726	0.028	0.0003	5.9	0.1	-1.7
C18	0.0227	0.726	0.033	0.017	7.0	3.7	16.5
C19	0.0227	0.726	0.033	0.017	7.0	3.6	15.1
C20	0.0227	0.726	0.029	0.0	6.1	0.0	0.6
C21	0.0227	0.726	0.032	0.011	6.7	2.4	10.6
C22	0.0227	0.726	0.031	0.014	6.7	3.1	10.4
C23	0.0227	0.726	0.031	0.010	6.5	2.1	7.3
C24	0.0227	0.726	0.029	-0.001	6.2	-0.1	2.9

Table B.3: Complete overview of error metrics obtained from the image (pre-)processing sensitivity analysis of location 3 in the Dinkel River study area. Various error metrics are presented for each case (C1, C2, ...) considered in the sensitivity analysis, see section 2.4.2 for a detailed description of each case. RMSE = root mean squared error; MBE = mean bias error; RMSE and MBE were normalised by the mean velocity magnitude obtained from the float method (0.40 m/s).

Case	Pixel size [m]	Vector spacing [m]	RMSE [m/s]	MBE [m/s]	NRMSE [m/s]	NMBE [%]	Difference RMSE w.r.t baseline [%]
C1 (baseline)	0.0214	0.685	0.020	0.016	5.0	3.9	-
C2	0.0214	0.685	0.034	0.032	8.7	8.0	74.6
C3	0.0214	0.685	0.025	0.021	6.2	5.4	24.9
C4	0.0214	0.685	0.019	0.014	4.7	3.6	-5.2
C5	0.0214	0.685	0.018	0.013	4.5	3.2	-8.9
C6	0.0428	1.371	0.021	0.016	5.3	4.1	6.6
C7	0.0283	0.907	0.023	0.019	5.8	4.7	16.0
C8	0.0142	0.456	0.021	0.016	5.3	4.1	6.5
C9	0.1070	3.426	0.021	0.015	5.3	3.7	5.5
C10	0.0856	2.741	0.017	0.004	4.3	1.0	-13.2
C11	0.0428	1.370	0.019	0.014	4.7	3.5	-5.4
C12	0.0107	0.343	0.022	0.018	5.4	4.6	9.3
C13	0.0054	0.171	0.029	0.026	7.3	6.6	45.6
C14	0.0214	0.685	0.019	0.015	4.9	3.8	-2.0
C15	0.0214	0.685	0.019	0.015	4.9	3.8	-1.3
C16	0.0214	0.685	0.019	0.015	4.8	3.7	-3.4
C17	0.0214	0.685	0.019	0.015	4.8	3.7	-3.2
C18	0.0214	0.685	0.025	0.022	6.3	5.5	25.8
C19	0.0214	0.685	0.026	0.023	6.5	5.9	30.4
C20	0.0214	0.685	0.019	0.014	4.7	3.6	-4.7
C21	0.0214	0.685	0.024	0.021	6.1	5.3	22.0
C22	0.0214	0.685	0.024	0.021	6.2	5.4	23.5
C23	0.0214	0.685	0.024	0.020	6.0	5.2	20.3
C24	0.0214	0.685	0.020	0.015	5.0	3.9	-0.4

C

Appendix C: Supplementary material Meuse River at Sambeek results

C.1. Additional statistics sensitivity analysis

Table C.1: Complete overview of error metrics obtained from the image (pre-)processing sensitivity analysis of location 1 in the Meuse River study area. Various error metrics are presented for each case (C1, C3, ...) considered in the sensitivity analysis, see section 2.4.2 for a detailed description of each case. Note that, in this case, an interrogation area size of 64x64 px was considered for case 12 (C12) instead of 32x32 px. RMSE = root mean squared error; MBE = mean bias error; RMSE and MBE were normalised by the mean velocity magnitude obtained from the float method (0.26 m/s). The color shades represent the relative performance. The green shades indicate relatively good performance, while red indicates relatively poor performance.

Case	Pixel size [m]	Vector spacing [m]	RMSE [m/s]	MBE [m/s]	NRMSE [m/s]	NMBE [%]	Difference RMSE w.r.t baseline [%]
C1 (baseline)	0.0605	0.954	0.094	0.089	35.7	34.5	-
C3	0.0605	0.954	0.096	0.091	37.13	35.25	2.2
C4	0.0605	0.954	0.075	0.070	28.93	27.11	-21.4
C5	0.0605	0.954	0.051	0.044	19.65	16.96	-50.8
C11	0.0303	0.477	0.093	0.089	36.15	34.46	-0.1
C12	0.121	1.909	0.115	0.110	44.61	42.64	23.6
C13	0.242	3.817	0.160	0.145	61.92	56.30	63.2
C14	0.0605	0.954	0.088	0.083	34.0	32.3	-6.2
C15	0.0605	0.954	0.085	0.081	33.0	31.4	-9.0
C16	0.0605	0.954	0.092	0.088	35.8	34.1	-1.2
C17	0.0605	0.954	0.093	0.088	36.1	34.2	-0.8
C18	0.0605	0.954	0.114	0.104	44.0	40.2	16.5
C19	0.0605	0.954	0.113	0.104	43.7	40.3	16.8
C20	0.0605	0.954	0.087	0.083	33.7	32.3	-6.4
C21	0.0605	0.954	0.087	0.083	33.7	32.3	-6.4
C22	0.0605	0.954	0.108	0.101	41.7	39.3	13.8
C23	0.0605	0.954	0.093	0.088	36.2	34.1	-1.1
C24	0.0605	0.954	0.097	0.090	37.4	35.0	1.4

D

Appendix D: Seeding Distribution Index (SDI) for improving LSPIV performance

In the discussion of this thesis (chapter 4), it was claimed that the effects of tracer scarcity and inhomogeneous seeding may be counterbalanced by using considerably longer image sequence durations for the LSPIV analyses; this claim was based on the findings of Pumo et al. (2021). However, an important fallacy of this approach is that the time-averaged velocity fields will still include many spurious, low- and zero-velocity measurements, which will likely result in a significant underestimation of the surface flow velocities nonetheless (Pizarro et al., 2020). In this appendix, a different approach was tested as an attempt to reduce error associated with low seeding densities and seeding inhomogeneity. More specifically, the methods as proposed in the recent studies of Pizarro et al. (2020) and Dal Sasso et al. (2020) were tested; they propose that the so-called 'Seeding Distribution Index' (SDI) should be computed to identify the optimal time window of a video recording to analyse. The dimensionless SDI index essentially aims to capture the seeding characteristics within the ROI of an image by combining the seeding density and spatial distribution of the tracers into a single parameter. The SDI is computed using an empirical equation which was formulated based on numerical experiments; the evidences arising from Pizarro et al. (2020) and Dal Sasso et al. (2020) show that this index is potentially a good descriptor for the identification of video segments that exhibit the best seeding conditions. The SDI is computed for each image in the image sequence according to the following equation:

$$SDI = D^{*0.1}\left(\frac{\rho}{\rho_{cD^*1}}\right)^{-1} \tag{D.1}$$

where D^* is the dispersion index (-), ρ is the seeding density in terms of particles per pixel (ppp), and ρ_{cD^*1} is the reference seeding density for $D^* = 1$ and was estimated to be $1.53{\cdot}10^{-3}$ ppp in Pizarro et al. (2020). D^* is a metric for the seeding homogeneity and is determined as follows: $Var(N)/E(N)$. In this case, $Var(N)$ and $E(N)$ represent the variance and mean value of the number of tracer particles (N), respectively, computed on equal-size subareas in the ROI. It is important to realise that the the optimal time windows in the video correspond to the lowest SDI values. Finally, the MATLAB codes provided by Pizarro et al. (2020) were used to compute the SDI.

In this study, LSPIV showed particularly poor performance for the imagery collected at location 1 in the Meuse River study area (Figure 3.24). Therefore, it was examined whether the SDI could be utilised to increase the LSPIV performance in this case. According to Dal Sasso et al. (2020), the methodology for identifying the optimal window involves four main steps: (1) calculate the SDI time series; (2) calculate the mean value of the SDI; (3) apply a smoothing function (e.g., median filter) to reduce noise in the SDI time series; (4) identify the windows in the image sequence that attain SDI values below the mean SDI threshold as calculated in step 2. The optimal window is then selected based on two criteria: firstly, the optimal window maximises the image sequence duration; secondly, the mean SDI value is minimised within the optimal window. The aforementioned methodology was applied to the drone imagery collected at location 1 in the Meuse River study area at a flight altitude of 56 m; the length of the full video is 120 s in this case. Figure D.1 shows the seeding density and dispersion index computed for each image in the image sequence; using these time series, the SDI time series could be computed

using Equation D.1 (Figure D.2). From Figure D.2 can be concluded that the time window of 68-120 s is the optimal window and should therefore be used for the purpose of the LSPIV analysis.

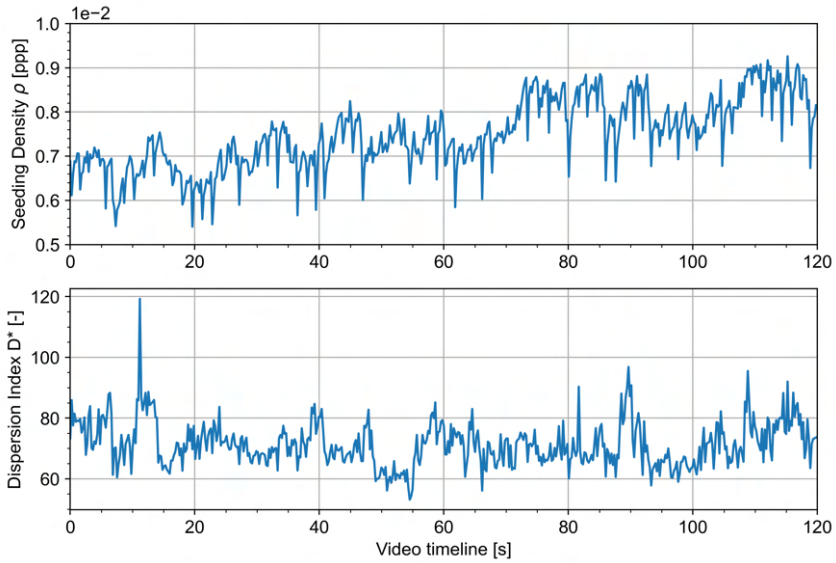

Figure D.1: Seeding density (top) and dispersion index (bottom) time series computed for drone imagery collected at location 1 in the Meuse River study area.

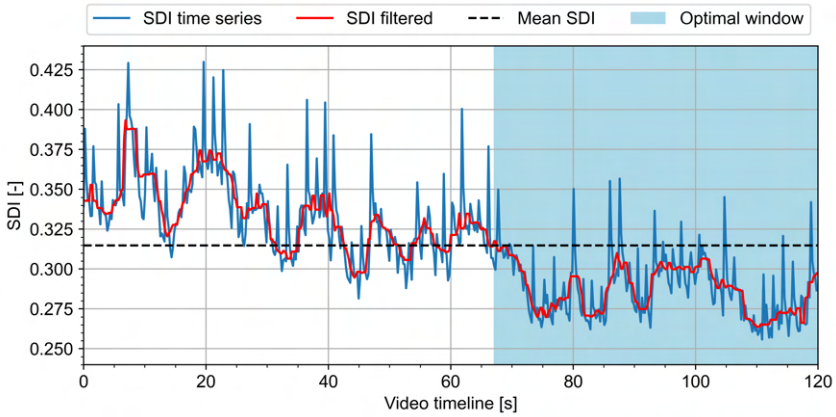

Figure D.2: SDI time series computed for drone imagery collected at location 1 in the Meuse River study area. The black dashed line represents the SDI threshold; (filtered) SDI values below this threshold indicate the best seeding conditions.

Based on the information obtained from the above analysis, the LSPIV analysis was performed on the sequence of images corresponding to the optimal time window (68-120s). According to the findings of the SA presented in section 3.2.4, it is fair to assume that an image sequence duration of 52 s is sufficient for the LSPIV analysis. Furthermore, the LSPIV analysis was performed on the full image sequence (0-120s) as well for comparison purposes. For the LSPIV analyses, a sampling frequency of 2 Hz, interrogation area size of 32x32 px and image resolution of 1280x720 px were adopted. Additionally, both the CLAHE and high-pass filters were applied to enhance the tracer visibility in the images. Lastly, the LSPIV-derived surface flow velocities were compared to reference velocity measurements obtained from the float method to assess the LSPIV performance.

The results of the LSPIV analyses are visualised in Figures D.3 and D.4. The time-averaged velocity fields corresponding to the two different time windows in Figure D.3 do not seem to differ much in a qualitative sense; they capture the same flow patterns as identified and described in section 3.2.2. However, LSPIV was unable to measure the surface flow velocities directly downstream of the weir (between X = 0 m and X = 8 m) in this case; this is attributed to the fact that a small sampling frequency

(2 Hz) was adopted. In spite of this, by employing the optimal time window for the LSPIV analysis, a considerable error reduction was observed with respect to the LSPIV analysis corresponding to the full video. The error metrics summarised in Table D.1 show RMSE and NRMSE values of 0.05 m/s and 19.7% for the full video, respectively, and 0.03 m/s and 12.6% for the optimal window, respectively; this translates to an error reduction of roughly 35%. All in all, the findings in this appendix show that a longer image sequence duration does not necessarily lead to an increase of the LSPIV performance in the case of sub-optimal seeding conditions. Instead, one can mitigate the negative effects of tracer scarcity and inhomogeneous seeding by only employing the time window in the video recording that exhibits the best seeding conditions; the SDI may be a powerful tool for this purpose. It is important to mention that the duration of the optimal window should still be sufficiently long.

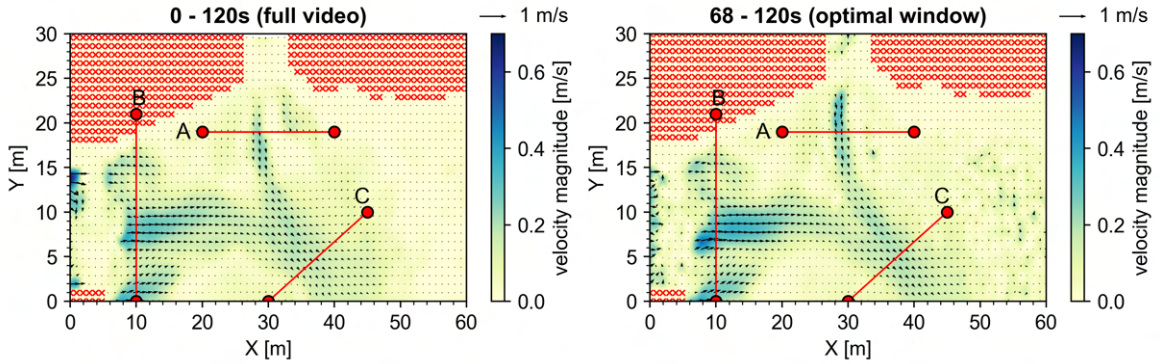

Figure D.3: Visual comparison of time-averaged surface water flow velocity fields computed with images from two different time windows of the same video recording: 0-120 s and 68-120 s. Imagery was acquired from a drone at location 1 in the Meuse River study area at a flight altitude of 56 m.

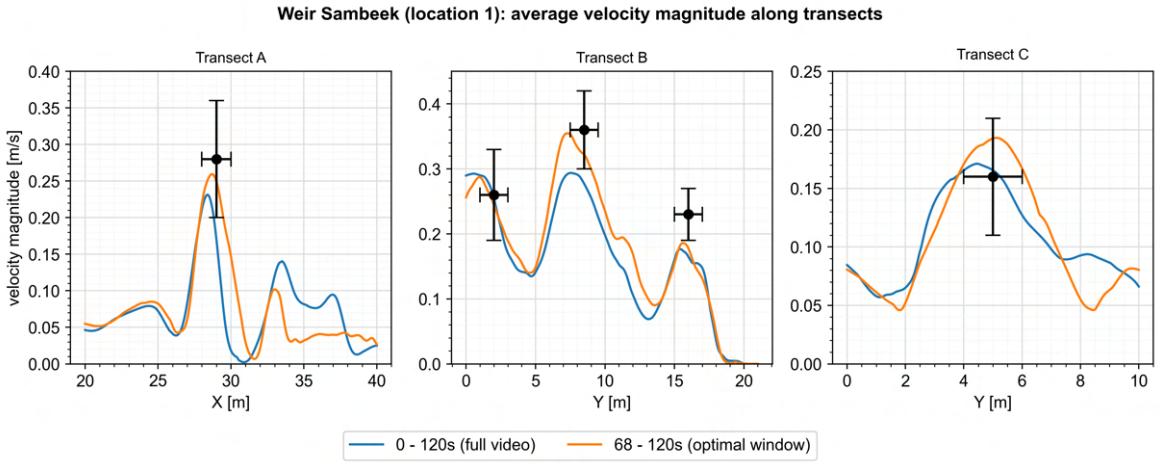

Figure D.4: Velocity profiles extracted from the transects defined in Figure D.3 for time windows of 0-120 s and 68-120 s. Markers represent mean surface water velocity magnitudes obtained from the float method. Uncertainty intervals surrounding the markers represent the standard deviation.

Table D.1: Summary of error metrics of location 1 at the Meuse River for two different time windows: 0-120 s and 68-120 s. RMSE = root mean squared error; MBE = mean bias error; RMSE and MBE were normalised by the mean velocity magnitude obtained from the float method (0.26 m/s).

Time window	Mean SDI [-]	Interrogation area [px]	Step size [px]	Sampling frequency [Hz]	RMSE [m/s]	MBE [m/s]	Normalised RMSE [%]	Normalised MBE [%]
0 - 120s	0.315	32	16	2	0.051	0.044	19.7	17.0
68 - 120s	0.288	32	16	2	0.033	0.027	12.6	10.4